# Electro-optic Photonic Integrated Circuits for Radio Frequency Multiplication and Translation

Gazi Mahamud Hasan

Thesis submitted in partial fulfillment of the requirements for the

Masters in Applied Science degree in Electrical and Computer Engineering

Ottawa-Carleton Institute for Electrical and Computer Engineering

School of Electrical Engineering and Computer Science

University of Ottawa

# Abstract

The ever-growing data traffic and super broadband services demanded by the end users have led the wireless communication network to undergo rapid development in terms of capacity, bandwidth, cost and mobility. The low-power, mature lower frequency bands are already congested and offer small capacity in wireless communication. On the other hand, the high capacity high frequency wireless system is inherently power hungry, costly and imposes complicated coverage schemes. This bottleneck has introduced the radio-over-fiber (RoF) system as a viable solution for broadband wireless access networks. The aim of this thesis is to address two major aspects of a broadband wireless access network using a distributed antenna system complemented by a digital coherent optical RoF link: the millimeter-wave (mm-wave) carrier generation at downlink and efficient single sideband (SSB) modulation at uplink and their configuration in electro-optic photonic integrated circuit format.

An optical path tracing method is proposed to transform any photonic circuit consisting of linear and time invariant optical components to its parallel counterpart comprising a collection of optical paths, each characterized by the transmission response of the element within it. This method is exploited to address the functionality of a photonic frequency multiplication circuit with a multiplication factor of eight where the time variance is handled by a focus on pure RF carriers and the Jacobi-Anger expansion. The series architecture consisting of four Mach-Zehnder modulator enables its application in a low RF drive condition with similar performance when compared to different functionally equivalent architectures.

The concept of a frequency multiplication circuit as a stable, tunable means of millimeter-wave generation can be extended to incorporate polarization modulators instead of conventional Mach-Zehnder modulators due to the fact that the cascade of polarization modulator and polarizer provides an intensity modulator whose biasing condition can be set by the polarizer angle and polarization state of the input light to each polarization modulator. The employment of polarization modulator can avoid DC bias drift and feasible discrete component implementation can be achieved which is important in a research environment to establish the proof of concept.

One of the circuits can access the millimeter-wave band for a wide range of modulation index; the other circuit can offer a RF power advantage in a moderate range of modulation index. Both circuits can provide a multiplication factor of eight which enables a low RF frequency source requirement. Simulation using industry standard software tools are used to validate theoretical predictions of the abovementioned circuits and their robustness against non-ideal factors are analyzed.

In addition, the frequency translation property of a single sideband modulator based on a generalized Mach-Zehnder interferometer structure consisting of four Mach-Zehnder modulator in parallel is experimentally demonstrated. The multi-functional photonic circuit fabricated on silicon on insulator platform can provide sub-carrier generation, in-phase and quadrature (IQ) modulation and frequency multiplication functionalities in addition to the frequency conversion.

The selection of the function is determined by the biasing condition of the modulators and RF drive specification which can be controlled externally. The employment of the multimode interference splitter/combiner can offer DC bias less operation due to its intrinsic phase relationship among the ports providing the necessary optical phase shift. Spatial separation of the up- and down-converted optical output opens the door for remote heterodyning operation. A carrier suppression of >20 dB and spurious sideband suppression > 12 dB relative to the principle harmonics is achieved when the circuit is operated as a frequency shifter with bias voltage tuning only.

The generalized Mach-Zehnder interferometer structure can be extended to support in-phase and quadrature modulation for any number of constituent phase modulators, which provide a general theory of in-phase and quadrature modulation. From this theory, the lowest dimension of the interferometer structure is found to be three which implies that a three phase modulator structure, in contrast to the orthodox four phase modulator structure, can provide in-phase and quadrature modulation when the drive signals to the phase modulators are linear combinations of in phase and quadrature component of the signal. A system simulation is used to validate its operation as an in phase and quadrature and single sideband modulator.

*Dedication: I would like to dedicate this thesis to my supervisor Professor Trevor James Hall and my family.*

# Acknowledgements

Every work of knowledge requires good amount of guidance and inspiration from mentors, peers and well-wishers for accomplishment. Hence, few words are here to express my sincere and heartfelt thankfulness to all those personas whose valuable support and assistance have enabled me complete this rigorous thesis project.

First of all I would like to mention my supervisor, Professor Dr. Trevor Hall who owes an extensive gratitude for his solid encouragement and counsel offered to me in pursuing this piece of work with brilliant efficiency. He has been my motivation to strike hard in every challenge since I am working with him. I earnestly thank him for believing in me with this project and guiding me from very beginning till now as a supportive chaperon. I thank Professor Dr. Karin Hinzer of University of Ottawa for her valuable consultation and advice in my research work. She and Dr. Ahmad Atieh, VP - Optical Systems at Optiwave Systems Inc. who are respected members of my thesis advisory committee have shown great interest in my work and I am highly thankful to them. Heartfelt thanks are for all the members of PTLab for their constant effort to maintain a supportive workplace with friendly environment where I could work vigorously. Of all my lab-mates, I would like to thank especially Mehedi Hasan for his enormous help in different aspects of my life both academic and personal, for which I am fervently indebted to him. A special appreciation goes to Peng Liu from Millview Photonics. who has introduced me to the industrial environment and mentored me in exploring industry practices of photonic circuits, testing and measurements and I graciously acknowledge his contribution in enhancing my expertise.

Last but not the least, I want to express gratefulness to my parents and all family members for their selfless love, prayers and support for which I am being able to pursue my aspirations diligently. I remember especially my late father with deep thoughts whose dream I am carrying on inside and wish to materialize it with sincerity.

# Table of Contents

# List of Tables

# List of Figures

# List of Acronyms

| | |
|---|---|
| RoF | Radio over Fiber |
| MZM | Mach-Zehnder Modulator |
| MZI | Mach-Zehnder Interferometer |
| GMZI | Generalized Mach-Zehnder Interferometer |
| MITP | Minimum Transmission Point |
| MATP | Maximum Transmission Point |
| SNR | Signal to Noise Ratio |
| CSR | Carrier Suppression Ratio |
| SSB | Single Sideband |
| OSSR | Optical Sideband Suppression Ratio |
| ESHSR | Electrical Side Harmonic Suppression Ratio |
| DP-MZM | Dual Parallel Mach-Zehnder Modulator |
| PM | Phase Modulator |
| PolM | Polarization Modulator |
| BERT | Bit Error Rate Tester |
| LD | Laser Diode |
| LO | Local Oscillator |
| DFB | Distributed Feedback |
| PIC | Photonic Integrated Circuit |
| MMI | Multi-Mode Interference Coupler |
| OSSB | Optical Single sideband |
| IoT | Internet of Things |
| MM-wave | Millimeter wave |
| WLAN | Wireless Local Area Network |
| GSM | Global System for Mobile Communications |
| UMTS | Universal Mobile Telecommunications System |
| LTE | Long-Term Evolution |
| RAU | Remote Antenna Unit |
| IM-DD | Intensity Modulation Direct Detection |
| VCO | Voltage Controlled Oscillator |
| RF | Radio Frequency |
| HNLF | Highly Non-Linear Fiber |
| FWM | Four Wave Mixing |
| IM | Intensity Modulator |
| DP-PolM | Dual Parallel Polarization Modulator |
| SBS | Stimulated Brillouin Scattering |
| UFBG-AOTF | Uniform Fiber Bragg Grating based Acousto-Optic Tunable Filter |
| LDV | Laser Doppler Velocimetry |
| FSF | Frequency-Shifted Feedback |
| FMCW | Frequency Modulated Continuous Wave |
| SOH | Silicon-Organic Hybrid |
| SOI | Silicon-on-Insulator |
| Pol | Polarizer |

| | |
|---|---|
| PD | Photodetector |
| OPLL | Optical Phase Locked Loop |
| PRBS | Pseudo Random Binary Sequences |
| EVM | Error Vector Magnitude |
| BS | Base Station |
| CO | Central office |
| AWG | Arrayed Wavelength Grating |
| LSB | Lower Sideband |
| USB | Upper Sideband |
| PC | Polarization Controller |
| PBS | Polarization Beam Splitter |
| SHSR | Spurious Harmonic Suppression Ratio |
| SER | Symbol Error Rate |
| WPAN | Wireless Personal Area Network |

# Chapter 1. Introduction

The ever-increasing data traffic and super broadband services such as high-definition video streaming, high-speed internet, video calling, cloud computing and Internet of things (IoT) have revolutionized the telecommunication network framework. Fiber communication has already been manifested as a future-proof infrastructure to provide wideband, high frequency, low loss, low cost, longer reach and interference immune signal distribution. The wireless mobile consumers also demand high-speed operation alongside the flexibility of the mobility of transponder and broadcasting capabilities to realize ubiquitous connectivity (communication anytime, anywhere and with anything). As a consequence, present wireless local networks must provide increased transmission capacity while maintaining sufficient coverage [1]. Conventional wireless network suffers from its narrowband nature which limits its operation in multi-Gb/s and future terabit/s applications. Complex modulation formats have been employed to increase its spectral efficiency; nevertheless the congested lower frequency bands urge the deployment of the high-speed service in the high frequency regime. The inherent high atmospheric attenuation, complex distribution system and complicated electronic generation process have prevented the inclusion of high-capacity millimeter wave (mm-wave) in the wireless regime. The solution is the smooth merging of fiber optics and wireless, traditionally distinct, systems to exploit high capacity with access flexibility. Radio-over-fiber (RoF) distributed antenna systems have been recognized as a high capacity, flexible, bandwidth efficient and cost effective solution to transparent wireless access through fiber-based infrastructure [2].

This thesis presents the findings of research concerning the generation of mm-wave signals utilizing optical methods for radio frequency multiplication and translation functionalities. This has important application to next generation access network infrastructure as the generation of mm-wave carriers at the remote antenna unit is essential to the successful implementation of a radio-over-fiber network employing a distributed antenna architecture complemented by optical digital coherent systems [3]. This chapter provides the motivation and background to set this research in context, outlines the challenges to be addressed and explains how the thesis is structured to meet its objectives.

## 1.1 Background & Motivation

### 1.1.1 Millimeter-wave and Radio-over-Fiber Networks

The ever-growing data traffic and super broadband services demanded by the end users have led the wireless communication network to undergo rapid development in terms of capacity, bandwidth, cost and mobility. Not more than 0.2% (11 million) of the world's population (5 billion) had access to a mobile phone in 1991 [4], which is 2% of fixed line telephone subscribers, whereas, in 2019, the number of mobile phone users was more than 8 billion. Almost the entire world population (97%) lives within reach of a mobile cellular signal with 82% living within the reach of an LTE or higher mobile broadband signal [5]. An estimated 4.1 billion people (53.6% of the world population) are using the internet in 2019, which reflects the yearly average growth of 10% of the internet users [6]. International bandwidth usage grew by 33.4 per cent on average annually between 2015 and 2019 [6].

The rapid growth in mobile cellular and mobile broadband subscriptions over the last decade reflects the demand for ubiquitous connectivity. After the introduction in 1997, Wireless Local Area Network (WLAN) have been continuing its growth, providing high data transmission rate to fixed wireless subscribers. Tremendous Internet growth due to technological advancement and competition among operators and the consequent demand for high speed applications are calling for high transmission capacity with sufficient coverage area butut the mobility offered by the mobile broadband services adds the choice of flexibility. That is why, while the fixed broadband subscriptions have continued to grow at a modest rate, a year-on-year growth rate of 18.4% has been observed for mobile broadband subscription [6]. More household environments are adopting Internet access without any fixed means for subscription such as a personal computer.

The trend has been shifting from fixed wireless subscription to more versatile mobile network access. Canada is also adopting the trend as the operators are continuously decreasing the gap between the fixed and mobile broadband speed [7]. The unprecedented demand for wireless bandwidth has placed a heavy burden on the lower microwave spectral region. Besides, from the Shannon channel capacity theorem, low carrier frequencies offer low bandwidth. Global System for Mobile Communications (GSM) operating at carrier frequencies in the 900 MHz or 1800 MHz has a 200 kHz channel spacing including 20 kHz for a guard band [8]. Universal Mobile Telecommunications System (UMTS) operates around 2 GHz with 4 MHz bandwidth [9]. IEEE 802.11ac and its successor IEEE 802.11ax protocol operate in the 2.4 and 5 GHz frequency spectrum [10]. Long-Term Evolution (LTE) standard operates at carrier frequencies up to 2.6 GHz with flexible channel bandwidth up to 20 MHz whereas, The LTE-Advanced technology offers a higher bit-rate than LTE because of scalable system bandwidth up to 100 MHz [11].

The tremendous growth of mobile data traffic and the advent of bandwidth-hungry wireless applications highlight the impending need for large bandwidth and high data rate in next generation mobile networks which enable complex modulation format and multiplexing schemes to increase spectral efficiency as well as push the wireless operation into the millimeter-wave (mm-wave) region to exploit the inherent bandwidth advantage. A few of the mm-wave frequency bands have been actively explored. K-band (18-27 GHz), Q-band (33-50 GHz) and W-band (75-110 GHz) are employed in satellite communications and military applications [12, 13]. 76-77-GHz and 77-81-GHz bands are used in automotive radar systems for long-range cruise control and short-range side-crash prevention [14]. The 60-GHz unlicensed band is used for short-range high-speed area networks that have been commercialized [15, 16]. The next generation (5G) systems have been explored, potentially, in mm-wave bands [17]. In particular, the unlicensed 60 GHz frequency band with GHz of spectrum available has achieved significant attention over the last two decades [18-19]. The principle obstacle is the high transmission path loss at high frequency. The stringent requirements of high modulation formats in terms of Signal-to-Noise Ratio (SNR) together with the propagation losses result in limited coverage which leads to service areas (cell) with reduced size and consequently, larger number of remote antenna units (RAU) with extensive feeder networks. The cost and complexities for the installation and maintenance complemented by the demanded broadband services have brought new paradigms in broadband wireless access networks with distributed antenna systems into light.

It is well established that optical fiber networks render high capacity, low attenuation, lower energy consumption and simplification to RAUs, base stations and the backhaul network that connect to the central station. The idea of Radio-over-Fiber (RoF) was conceived as early as the eighties following the introduction of radio frequency/microwave subcarrier multiplexing that rapidly gained popularity for the distribution of cable TV channels [20-22]. The term RoF is usually applied when it is used to facilitate wireless access. Traditionally, in a RoF paradigm, the application of wireless link for access networks takes place in the last mile segment of the data transport whereas, the analogue transport of wireless data from central station to base station occurs through the fiber infrastructure. With that, RoF technology is able to manage the unification of wireless and optical backbone network towards a converged network infrastructure with simplified control, management and routing functionalities.

The simplest, conventional analogue transport over the RoF link involves intensity modulation direct detection (IM-DD) method which is prone to high power consumption, limited dynamic range and periodic RF power fading. The industry preference is for digital RF transport [3]. The Photonic Technology Laboratory of University of Ottawa is investigating, inter alia, wireless access networks capable of delivering the ubiquitous broadband and computing access from the perspective of energy efficiency and environmental factors. Hall et al. reasoned that broadband wireless access network using distributed antenna system architecture deployed in cluttered urban environments complemented by a digital coherent optical RoF link provides an energy efficient solution [3]. The millimeter-wave (mm-wave) carrier generation at downlink and efficient single sideband (SSB) modulation at uplink are two major factors to be considered for improvement of digital coherent optical transport of RF signal [23-25].

### 1.1.2 Optical MM-wave Generation by External Modulation

Numerous researches have been undertaken on mm-wave generation techniques. The conventional electronic methods involves either phase locking a frequency divided voltage controlled oscillator (VCO) or using cascaded multiplication stages. These methods are limited by the bandwidth of the digital divider, or the complexities due to suppression of unwanted harmonics by maintaining resonance which only offers narrowband operation. Photonic techniques for mm-wave generation have become attractive over the last two decades. The simplest approach is the heterodyne beating of two phase correlated optical carriers separated in frequency at a high speed photo-detector. The efficacy of this approach depends upon the stability, linewidth and degree of phase correlation between the carriers.

One approach to photonic means to achieve mm-wave generation is to use heterodyne beating of a master and a slave lasers. Heterodyning two separate lasers results in an electrical linewidth that is greater than the optical linewidth due to the absence of critical phase correlation [26-27]. Phase-locked loop techniques may then be used to control the frequency of the slave laser, so that the beat is locked to a harmonic of an mm-wave reference [28-30]. Alternatively, optical injection locking can be used to phase lock a narrow linewidth single frequency to individual lines separated by the desired RF frequency of a frequency comb. In general, phase locking mechanisms are complex, costly and require careful wavelength alignment, a complicated feedback network and a high level of temperature control for stabilization. The complexity can be reduced greatly by

employing a dual-wavelength laser which can enable oscillations at two modes subject to the same electrical, thermal and mechanical fluctuations [31-32]. The linewidth of the beat signal between the two modes separated in frequency by the desired RF frequency will be then significantly narrower than the linewidth of the individual modes because of the correlation of their phase noise [33], though competition between the two modes for a share of the gain can lead to the instability.

External modulation based photonic mm-wave generation techniques are emerging as a feasible candidate due to its higher spectral purity, simplicity, stability and low RF frequency requirement. The basic principle is to phase-modulate an optical carrier from a single laser source by a radio frequency (RF) electrical carrier via a suitable electro-optic modulator. The modulation results in an optical spectrum containing a multitude of phase-correlated lines separated by the RF frequency. To the best of the author's knowledge, the first integrated mm-wave generation scheme obtaining a RF frequency multiplication factor of 2 utilizing a $LiNbO_3$ Mach-Zehnder modulator (MZM) was developed by O'Reilly et al. [34]. After that, extensive investigation of external modulation as a viable method for mm-wave generation has been conducted. The external modulation not only offers phase correlated operation but also delivers a frequency multiplication option which reduces the bandwidth constraints of the optical modulators and RF components. Millimeter waves beyond 100 GHz have been generated from lower RF frequency sources exploiting the frequency multiplication capability. Numerous architectures have been proposed to obtain different multiplication factor, better carrier and unwanted harmonic suppression, stable operation in non-ideal situation and simplicity for integration. Table 1.1 summarizes some of the works related to mm-wave generation with frequency multiplication functionality. A detailed list is given in Appendix I.

Table 1.1: Summary of some photonic frequency multiplication techniques with experimental results

| Short description | Multiplication factor | Performance metrics |
|---|---|---|
| Mach-Zehnder modulator (MZM) biased to suppress the carrier and even order harmonics [34] | 2 (36 GHz from 18 GHz) | Signal to Noise ratio (SNR) > 35 dB |
| MZM biased to suppress the odd order optical harmonics is followed by a fixed-wavelength optical notch filter to suppress the carrier [35] | 4 (32-50 GHz from 8-12.5 GHz) | Optical sideband suppression ratio (OSSR) > 25 dB |
| Dual parallel MZM (DP-MZM) with the outer Mach-Zehnder interferometer (MZI) is biased at MITP. The sub MZMs are biased at maximum transmission point (MATP). The sub MZMs are driven by relative $\pi/2$ phase shifted RF input. No optical filtering is needed [38]. | 4 (40-72 GHz from 10-18 GHz) | Electrical side harmonic suppression ratio (ESHSR) > 38 dB (40 GHz)<br>Optical sideband suppression ratio (OSSR) > 36 dB (72 GHz) |
| MZM biased at MITP followed by 400m highly nonlinear fiber (HNLF) utilizing four wave mixing (FWM) to generate 3rd order optical harmonics. Adoption of fiber Bragg gratings is needed to filter out unwanted 1st order optical harmonics [43] | 6 (40 GHz from 6.667 GHz) | ESHSR >25 dB<br>SNR ~50 dB<br>Linewidth < 3 Hz |

| | | |
|---|---|---|
| Two cascaded DP-MZM with all sub-MZMs are differentially driven and biased at MATP. The outer MZIs of the two DP-MZMs are biased at MITP. Carrier and odd order unwanted harmonics suppression can be achieved by design [46]. | 8 (60-80 GHz from 7.5-10 GHz) | SNR > 40 dB (60 GHz)<br>Phase noise -73 dBc/Hz at 10 kHz offset (60 GHz)<br>OSSR > 30 dB (80 GHz) |
| A polarization division multiplexing-dual arm MZM (PDM-DMZM) or PDM-DPMZM followed by an FBG filter to suppress carrier provides tunable multiplication factor under different DC biases and RF drive phase conditions [48]. | i) 2 (20 GHz from 10 Ghz)<br>ii) 4 (24 GHz from 6 GHz)<br>iii) 8 (28 GHz from 3.5 GHz) | OSSR > 15 dB (2-tupling)<br>OSSR > 15 dB (4-tupling)<br>OSSR > 10 dB (8-tupling) |
| A DP-MZM is placed in a Sagnac loop with its sub-MZMs and outer MZI are biased at MATP. By controlling the polarization controller to satisfy a strict condition, carrier is suppressed at the polarizer [51]. | 8 ( 24 GHz from 3 GHz) | OSSR ~ 18 dB<br>ESHSR ~ 16 dB |
| Two stage (frequency quadrupling followed by frequency doubling) architecture employing MATP-biased MZM at 1st stage and MITP-biased MZM at 2nd stage is used. The quadrupled microwave harmonic from the 1st stage is the RF drive for the 2nd stage's MZM. Optical bandpass and band-elimination filters are needed for carrier and unwanted harmonics suppression [62]. | 8 (100 GHz from 12.5 GHz) | Carrier suppression ratio (CSR) > 60 dB<br>Optical sideband suppression ratio (OSSR) > 30 dB<br>SNR > 70 dB<br>Phase noise degraded by ~19.2 dB at 100 kHz offset |

### 1.1.3 Frequency Translation/ Single Sideband Modulation using Generalized Mach-Zehnder Interferometer (GMZI) Structures

One of the fundamental requirement in the uplink of a coherent radio-over-fiber system is to transfer the signal from the RF domain to the optical domain while preserving its phase and amplitude information [3]. The orthodox method for this conversion is the employment of a single side-band (SSB) modulator/frequency shifter where an optical carrier is modulated by the received mm-wave signal. The outcome is a frequency up-converted optical signal, shifted by the mm-wave frequency from its emission frequency.

The application of a photonic frequency shifter is not limited to a heterodyne light communication system. The other sectors where it plays a key role are: laser Doppler velocimetry (LDV) and Doppler Lidar systems [70-71]; high quality multicarrier generation with a recirculating frequency shifting loop [72-73]; frequency-shifted feedback (FSF) laser [74]; true time delay beam steering in frequency modulated continuous wave (FMCW) radars [75]; high-resolution laser spectroscopy [76]; and measurements of ultra-high-Q photonic crystal nanocavities [77]. Various techniques have been pursued to realize a high-performance frequency shifter. Early photonic frequency shifters are based on discrete components [78-80]. To the best of the authors' knowledge, an integrated frequency shifter based on a titanium-diffused $LiNbO_3$ optical waveguide circuit was reported for the first time in 1981 [81]. The most conventional method to obtain frequency conversion is to use an optical single sideband (OSSB) modulator followed by filter structure to suppress carrier and/or unwanted sideband [82-85]. Its operation is limited by the frequency

response of the filter. In addition, the optical source, modulator and the filter must be very closely matched in frequency of operation that involves temperature control, which is undesirable in terms of energy consumption.

Mach-Zehnder interferometer (MZI) based frequency conversion has been investigated intensely [81, 86-89]. Carrier and unwanted sideband suppression by design is possible by applying appropriate RF signals with strict relative phase relationships, biasing the MZI structure to the proper operating point and/or implementing phase-shift elements within the arms of a MZI. The spectral purity can be impaired by any imbalance in the mentioned features. Mature $LiNbO_3$ modulator technology is a natural choice for frequency shifting purpose as its extinction ratio is relatively high and it can offer a linear electro-optic effect with large bandwidth. However, it needs high drive voltage and is not suitable for large-scale photonic integration. Besides, $LiNbO_3$ modulator also suffers from severe dc bias drift caused by charge screening and dielectric relaxation. A compact footprint can be gained by using the Si platform which can exploit CMOS compatible industry standards for optoelectronic integration. With the recent studies on high-speed modulator, Si optical frequency converters with excellent performance are emerging. Lauermann et al. demonstrated an integrated frequency shifter on a Silicon-Organic Hybrid (SOH) platform with conversion efficiency of -5.8 dB while suppressing spurious sidebands by more than 23 dB for a frequency range up to 10 GHz [90]. Another Si photonic frequency shifter has been reported recently with carrier suppression of 27 dB and at least 12 dB sideband suppression at 1 GHz [91].

Other methods for frequency conversion includes traveling wave TE/TM mode conversion [92], serrodyne translation [93-94] and acousto-optic deflection [79-80, 95-96]. Serrodyne technique can offer high carrier and spurious sideband suppression when a sawtooth shaped modulating signal with very small fall time (very small percentage of the sawtooth signal period) can be applied. This implies a very high bandwidth for the modulator and driving circuit are needed for sufficient spectral purity and high achievable frequency shift. In addition, a conventional Si diode modulator cannot be operated with serrodyne signal and so, thermo-optic modulation is necessary, which restricts its high frequency operation. Acousto-optic modulation depends on the acoustic wave induced refractive index variation which demands delicate phase matching. The operation is inherently limited to low frequency and, as Si is not piezoelectric, hybridization with other materials becomes mandatory. All-optical frequency shifting operations based on stimulated Brillouin scattering in optical fibers has also been demonstrated [97-98], which are limited by the fixed Brillouin frequency of a fiber and a complicated pump wave locking procedure.

## 1.2 Aim & Objectives

The aim of this thesis is to explore the two major aspects of digital coherent optical transport of RF signals: the millimeter-wave (mm-wave) carrier generation at downlink and efficient single sideband (SSB) modulation/frequency translation at uplink. The focus of this work is on designing circuits for radio frequency multiplication and translation, validating their theoretical functionalities through industry standard software tools, analyzing their qualitative deviations

from ideal outcome when non-ideal conditions for circuit operation are considered and feasibility check for integrated implementation. Specific objectives are:

1) To establish a generalized theory employing graphical approach which can investigate any photonic circuit consisting of linear and time invariant optical component. The time variant nature of active elements can be handled by a focus on pure RF carriers and the Jacobi-Anger expansion.
2) To design simple photonic mm-wave generation circuits using external modulation so that both discrete component and integrating circuit implementation can be achieved.
3) To improve the performance (e.g., spectral purity, linearity and dynamic range, power consumption, footprint, and stability) by investigating their non-ideal characteristics and correcting their limitation.
4) To investigate a generalized Mach-Zehnder interferometer architecture fabricated on silicon on insulator platform to analyze its functionalities qualitatively and study its performance as a SSB modulator/frequency up-converter
5) To sort out possible modifications needed in the design of the GMZI SSB modulator for future fabrication so that performance can be improved.
6) To generalize the GMZI structure to the IQ modulation format

## 1.3 Structure of the Thesis

The thesis has been structured into six (6) chapters to demonstrate the achievements in research meeting the objectives mentioned above.

Chapter 1 describes the motivation and the background of the research. It addresses the previous work done in the topics and their roadblocks. This chapter also summarizes the objectives of the thesis and achievements during the period of research.

Chapter 2 introduces a cascaded configuration consisting of 4 MZMs, each biased at its minimum transmission point (MITP) as a superior optical millimeter-wave generation scheme. The functionality of frequency multiplication is analyzed by an optical path tracing method. An optical path can be expressed as a phasor if the optical components are optically linear. The time variant nature of active elements can be handled by a focus on pure RF carriers and the Jacobi-Anger expansion. Satisfactory performance in terms of spectral purity, tunability and RF power efficiency is observed by simulation. Its simple architecture has the feasibility to be integrated in any material platform that offers electro-optic modulators.

Chapter 3 discusses two architectures capable of mm-wave generation. The first architecture involves a dual-parallel structure with each arm containing two cascaded PolMs with analyzers between a Y-power splitter at the input and a polarisation beam combiner and polarizer at the output. The second single arm architecture consists of four polarization modulators (PolM) in series, each followed by a polarizer (Pol). Both circuits can perform as an optoelectronic method of microwave frequency octupling for a broad range of modulation index. The optical carrier and all sidebands except for harmonics of order equal to an odd integer multiple of four are suppressed without the necessity of any optical or electrical filter or careful adjustment of RF drive voltage.

The second circuit offers additional RF power advantages. The robustness of the circuit is also verified by taking different non-ideal factors into consideration.

In chapter 4, a multi-functional photonic circuit implemented on silicon on insulator (SOI) platform is reported. Eight phase modulators are connected to provide four Mach-Zehnder interferometer structures in parallel. Multimode interference couplers are used as the splitter/combiner of the MZI structures to provide static DC bias. This architecture generates two principle spatially separated 1st order harmonics from a single light source, which may be collected from separate ports without using any optical demultiplexing filters which permits remote heterodyning. A carrier suppression of >20 dB and spurious sideband suppression > 12 dB relative to the principle harmonics is achieved with bias voltage tuning only. In addition to the frequency conversion, the circuit can also perform as a sub-carrier generator, IQ modulator and frequency multiplier.

In chapter 5, a generalized theory of complex modulation utilizing a generalized Mach-Zehnder interferometer (GMZI) is presented. The theory suggests that any number of phase modulator greater than two arranged in a parallel cascade can perform vector modulation scheme. A circuit consisting of three phase modulators (PM) in parallel, in contrast to the conventional architectures with four PM, can act as an IQ modulator with distortion-limited functionality. Increment of the dimension of the GMZI structure and adoption of linear combination of in-phase and quadrature signal as the drive to modulator are conjectured to be one of the condition of the ideal operation. Numerical simulation validates the operation of IQ modulator based on 3 PM-GMZI structure.

Chapter 6 summarizes the findings in the thesis, makes conclusions and offers recommendations for further work.

VPIphotonics Design Suite$^{TM}$ (version 9.8.0.1-version 10.0) simulation software is used to simulate all the considerations throughout the thesis. It sets the industry standard for software and services supporting end-to-end Photonic Design Automation (PDA) and Optical Equipment Configuration (OEC). VPI Design Suite provides an integrated, flexible design environment with sophisticated means for signal representation and conversions, powerful numerical algorithms tailored for specific applications, extensive libraries of realistic and widely adaptable component models, and powerful functions supporting day-to-day design, analysis and optimization processes. It can perform abstractions between the simulation layers — component, transmission, and network layer. The cascaded S-matrix approach for modeling passive components allows the efficient design of large-scale passive PICs in the frequency domain and active or dynamically tunable PICs in the time domain. This merging greatly reduces the overall simulation inaccuracies inherent to any time-domain simulations, and thus enables fast and accurate simulations of large-scale PIC with thousands of dispersive components. This approach also enables modeling multiscale integrated circuits with lengths of photonic components ranging from a few microns to several centimeters on the same chip. The combination of a powerful graphical interface, a sophisticated and robust simulation scheduler and realistic simulation models together with flexible optical signal representations at different degrees of abstraction enables accurate and efficient modeling of any transmission system including bidirectional links, ring and mesh networks.

The primary reason to utilize VPIphotonics Design Suite$^{TM}$ is that it is one of the industry-standard simulation tools which can be implemented to design RoF system. Two application tools are extensively used in this thesis: VPItransmissionMaker Optical Systems and VPIcomponentMaker Photonic Circuits. VPItransmissionMaker Optical Systems supports behavioral and detailed physical modeling of subsystems and components. Physical models allows studying the effect of the smallest components on the longest systems whereas models following the Black Box and Datasheet Model philosophies enable design from a systems-level perspective by utilizing measurable performance parameters rather than physical framework. VPIcomponentMaker Photonic Circuits offers advanced wide-spectrum, dynamic models of active, dynamically tunable and passive elements such as semiconductor lasers and LEDs, switches, modulators, detectors, AWG, MMI-based MUX/DeMUX, delay lines, filters, directional couplers, branches, MMIs, star couplers, microring resonators and waveguides. These can be interconnected in any permutation to design devices and photonic circuits. The full longitudinal and spectral dynamics of lasers and semiconductor optical amplifiers, careful modeling of external optical modulators and their electronic drive circuitries is important to characterize photonic circuits presented in this thesis with respect to large signal dynamics, tuning behavior, noise characteristics, side-mode suppression and modulation response. Designs and performance of active and passive devices and PICs can be abstracted for systems-level simulations with VPItransmissionMaker Optical Systems.

## 1.4 Original Contributions and Achievements

The thesis contributes to the advancement of the field of RoF technology and microwave photonics through both original contributions and the critical analysis of current knowledge. The contributions of the author include:

1. A simplified radio frequency multiplication architecture employing four Mach-Zehnder modulator in series to obtain RF power advantage with a multiplication factor of eight
2. Two radio frequency multiplication architecture utilizing polarization modulator to obtain multiplication factor of eight
3. Employment of the mm-wave generation architectures in a RoF system to validate their operation by software simulation
4. Extension of a graphical method to address the non-ideal factors of any linear optical circuit component.
5. Test, measurement and analysis of a fabricated multifunctional circuit and identify its operation condition and limitation
6. Validation a GMZI structure's frequency shifting capability by experimentation
7. Incorporation of a three phase modulator structure in a system to validate its functionality as a working IQ modulator.

The results demonstrated in this thesis were obtained during a period of study at the University of Ottawa to fulfill the requirement of achieving an M.A.Sc. degree. The work was carried out under the supervision of Professor Trevor James Hall from Winter 2018 to Fall 2019 at the Photonic Technology Lab (PTL). The following publications related to this research work (thesis) were published or submitted for publication during this period.

[1] **G. M. Hasan,** M. Hasan, K. Hinzer, T. Hall, " Vector modulation scheme using three phase modulator," In 2019 International Conference on Numerical Simulation of Optoelectronic Devices (NUSOD), Ottawa, ON, Canada, 8-12 July 2019, pp. 127-128. DOI: 10.1109/NUSOD.2019.8806843

[2] **G. M. Hasan,** M. Hasan, K. Hinzer, T. Hall, " Optical frequency multiplication technique using cascaded modulator to achieve RF power advantage," In 2019 International Conference on Numerical Simulation of Optoelectronic Devices (NUSOD), Ottawa, ON, Canada, 8-12 July 2019, pp. 125-126. DOI: 10.1109/NUSOD.2019.8806895

[3] **G. M. Hasan,** M. Hasan, H. Shang, D.-G. Sun, K. Hinzer, P. Liu, T. Hall, "Energy efficient photonic millimeter-wave generation using cascaded polarization modulators," Optical and Quantum Electronics, 51:7, pp. 217, June 2019, DOI: 10.1007/s11082-019-1927-4

[4] **G. M. Hasan,** M. Hasan, K. Hinzer, T. Hall, "Filterless frequency octupling circuit using dual stage cascaded polarisation modulators," Journal of Modern Optics, 66:4, pp. 455-461, December 2018, DOI: 10.1080/09500340.2018.1555292

[5] **G. M. Hasan,** M. Hasan, P. Liu, D.-G. Sun, K. Hinzer, T. Hall, "Energy efficient photonic millimeter-wave generation using cascaded polarization modulators," 2018 International Conference on Numerical Simulation of Optoelectronic Devices (NUSOD), Hong Kong, 5-9 November 2018, pp. 29-30. DOI: 10.1109/NUSOD.2018.8570277

[6] **G. M. Hasan,** M. Hasan, T. Hall, "Performance analysis of a multi-function photonic architecture on SOI acting as a frequency shifter" (Submitted) March 2020.

Contributions not directly related to this thesis:

[1] M. Hasan, **G. M. Hasan,** K. Hinzer, T. Hall, "Comments on Zihang Zhu, Shanghong Zhao, Xuan Li, and Kun Qu, Tao Lin "Photonic generation of frequency-octupled microwave signal with reduced electrical local oscillator power and improved spectrum purity"," Optical and Quantum Electronics, 51:157, May 2019, DOI: 10.1007/s11082-019-1877-x

# Chapter 2. Optical Frequency Octupling Circuit with RF Power Advantage

## 2.1 Introduction

A major pre-requisite for the widespread deployment of high-capacity digital coherent radio-over-fiber (RoF) systems is the effective generation and transmission of millimeter wave (mm-wave) carriers over fiber at the down link (central office to base station/remote unit) [3]. The technique to generate mm-wave and its feasible transmission over the fiber have been studied extensively over the years. Electronic methods either phase lock a frequency divided voltage controlled oscillator (VCO), which is limited by the digital divider's upper frequency limit or use cascaded multiplication stages: the amplifier in each stage must limit to generate harmonics and must be resonant to extract the required harmonic, which results in a complex circuit that is narrow band and power hungry. Photonic generation has become attractive, due to its ability to generate RF signals at frequencies exceeding 100 GHz, which generally involves an optical heterodyne technique in which two phase correlated optical carriers separated by the mm-wave frequency beat at a square-law photodetector (PD). Various optical mm-wave generation approaches have been investigated and developed involving two laser sources [99-100], dual-wavelength laser [31-32], non-linear effects [43],[60],[61],[65] and external modulation. Heterodyning two separate free-running lasers results in an electrical linewidth that is greater than the optical linewidth due to the absence of critical phase correlation [26-27]. Different methods such as optical injection locking [31],[100], mode locking [27],[101], and optical phase locked loop (OPLL) [29-30] have been applied to minimize phase noise and stabilize frequency fluctuation. Optical injection locking requires careful wavelength alignment and high level of temperature control. Mode-locking requires temperature stabilization and a complex electronic feedback control. OPLL significantly increases system complexity and cost. The nonlinear effects such as Four-Wave Mixing (FWM) require longer fiber length, high power to optimize desired harmonics and a phase matching condition to be achieved.

External modulation generally employs one laser source and intensity/phase modulators. To the best of the author's knowledge, the first mm-wave generation scheme obtaining a RF frequency multiplication factor of 2 utilizing a $LiNbO_3$ intensity modulator was developed by O'Reilly et al. [34]. After that, extensive investigation of external modulation as a viable method for mm-wave generation has been conducted. Vallejo et al. experimentally demonstrated the transmission of 10 Gb/s 32-QAM signal over hybrid fiber/FSO network at 40-90 GHz utilizing a frequency doubling scheme [102]. The external modulation not only offers simple, stable and spectrally pure operation but also delivers a frequency multiplication option which reduces the bandwidth constraints of the optical modulators and RF components. Millimeter waves in the range of 100 GHz [62], 210 GHz [61], 80 GHz [46],[50] 60-70 GHz [36],[38],[66] have been generated from lower RF frequency sources exploiting the frequency multiplication capability. Numerous architectures have been proposed to obtain different multiplication factor, better carrier and unwanted harmonic suppression, stable operation in non-ideal situation and simplicity for integration. Table 1.1 summarizes some of the works related to mm-wave generation with frequency multiplication functionality. Although most of the works reporting transmission feasibility employed single-stage

modulation scheme for optical mm-wave generation, large-scale integration of high-speed electro-optic modulator on mature material platform such as $LiNbO_3$, SOH, SOI, III-V opens the window for multi-stage architectures to be exploited.

In this chapter, a graphical method to address the functionality of a photonic frequency multiplication circuit is presented. The optical path tracing scheme exploits the fact that the transmission of an optical path can be expressed as a phasor if the optical components on it are optically linear. The time variant nature of active elements can be managed by incorporating pure RF carriers and the Jacobi-Anger expansion. Non-ideal RF situations can be quantified which is difficult to obtain in a compact analytic fashion. The method can be extended to involve imbalances in the optical domain. A cascaded configuration consisting of 4 MZMs, each biased at its minimum transmission point (MITP) is proposed and analyzed by the mentioned technique as a superior optical millimeter-wave generation scheme. Frequency multiplication factor of eight can be achieved without any optical/electrical filter. Its spectral purity obtained by design and robustness against the non-ideal factors is verified by simulation using industry standard software package. A comparative analysis with three other frequency 8-tupling circuits [46],[57],[103] provides the evidence of the RF power advantage the proposed circuit can offer. The architecture of the circuit engineers the modulation index of the system which allows operation with low RF power with satisfactory performance. The simplicity inherent to the architecture enables its feasibility to be integrated in any material platform that offers electro-optic modulators. A complete (down-link) simulation of a digital coherent RoF system is also presented as an application of the proposed circuit.

## 2.2 Contribution

A short report on the graphical method and proposed frequency multiplication system has been presented in the 2019 International Conference on Numerical Simulation of Optoelectronic Devices (NUSOD) [115]. This chapter discusses an elaborated and extended version of the theory and its application in extracting the functionality of a photonic frequency multiplication architecture quantitatively. A comparative study of four functionally equivalent frequency octupling circuit is presented. The application of a frequency multiplication circuit in a RoF system is also shown by simulation. I drafted the papers, performed the simulations and contributed the original ideas by extending the theory to incorporate non-ideal factors and predict the functionality quantitatively. Mehedi Hasan has contributed the circuit concept. Dr. Karin Hinzer and Dr. Trevor Hall were the principal investigators that formulated the research project. Dr. Hall contributed to the theory, provided advice on the interpretation of the results and helped revise the manuscript.

## 2.3 Theory

A photonic circuit can be modelled as a combination of passive and active optical elements through which light is passing from one point to another. Each element characterizes the light depending on its transmission response. So the whole circuit can be represented as a collection of light paths, each path tracing from the input to output would have the exact transmission characteristics attained from the optical elements on its way. This is equivalent to model the circuit using its parallel counterpart. The problem becomes more tractable if the passive optical elements are linear and time invariant. The active phase shifters / delays are linear optically but are time variant. In

the analysis below, this time variance is handled by a focus on pure RF carriers and the Jacobi-Anger expansion.

An abstract graph can be considered to represent the collection of the light paths. The vertices on this graph describe splitters (defined by their transmission matrices) and edges describe optical components in the arms such as active phase shifters driven by RF signals or delays and pre-set phase biases. Selecting one port at a vertex as input and one port at a different vertex as output, every possible path can be traced and summed to obtain the total transmission.

Frequency multiplication using external modulation involves phase modulators which enable the light to be modulated by a pure RF carrier. The modulated light components then interfere to produce the desired response. A frequency multiplication technique employing four differentially driven Mach-Zehnder modulators (MZM) in series, each biased to its minimum transmission point can be modelled by its equivalent parallel architecture utilizing the above mentioned optical path tracing method. There are $2^q$ paths through the structure corresponding to all choices of the upper and lower arms in each stage. The total transmission can be represented as:

$$f(t) = \frac{1}{2^q} \sum \rho_\alpha \exp\{im[\sum_{p=1}^{N} \sigma_p \cos(\omega_{RF} t + \Delta\emptyset_p)]\} \quad (2.1)$$

$$\rho_\alpha = \prod_{p=1}^{N} \alpha_p \quad (2.2)$$

where $N$ is the number of MZM stages on each optical path, $m = (\pi v_{RF})/v_\pi$ is the modulation index of each MZM stage, $v_\pi$ is the half-wave voltage, $\omega_{RF}$ is the RF angular frequency, $\Delta\emptyset_p = (p-1)\pi/4 \quad (p = 1,2,3,4)$ is the phase shift of the p[th] RF drive introduced to the p[th] MZM and $q$ is the number of optical splitter/combiner pairs on each optical path.

Being differentially driven, each MZM introduces an intrinsic π phase difference between its two arms which can be represented by $\sigma_p$ (for ideal case: upper arm $\sigma_p$ = 1, lower arm $\sigma_p = \exp(i\pi)$. Additional phase relationship in optical domain due to null point biasing of each MZM can be represented by $\alpha_p$. For the case considered here, $\alpha_p = \sigma_p$. An MZM biased at its maximum transmission point would have $\alpha_p$=1.

The sum of the RF drive in equation (2.1) can be expressed in terms of its in-phase and quadrature components as follows:

$$\sum_{p=1}^{N} \sigma_p \cos(\omega_{RF} t + \Delta\emptyset_p) = [\sum_{p=1}^{N} \sigma_p \cos(\Delta\emptyset_p)] \cos(\omega_{RF} t) - [\sum_{p=1}^{N} \sigma_p \sin(\Delta\emptyset_p)] \sin(\omega_{RF} t) \quad (2.3)$$

Or equivalently as the real part of the complex phasor sum:

$$\sum_{p=1}^{N} \sigma_p \exp[i(\omega_{RF} t + \Delta\emptyset_p)] = [\sum_{p=1}^{N} \sigma_p \exp(i\Delta\emptyset_p)] \exp(i\omega_{RF} t) \quad (2.4)$$

Now from the phasor summation formula:

$$r_\sigma \exp(i\theta_\sigma) = \sum_{p=1}^{N} \sigma_p \exp(i\Delta\emptyset_p) = \sum_{p=1}^{N} \sigma_p \cos(\Delta\emptyset_p) + i \sum_{p=1}^{N} \sigma_p \sin(\Delta\emptyset_p) \quad (2.5)$$

it can be shown that:

$$r_\sigma \cos(i\theta_\sigma) = \sum_{p=1}^{N} \sigma_p \cos(\Delta\emptyset_p); \qquad r_\sigma \sin(i\theta_\sigma) = \sum_{p=1}^{N} \sigma_p \sin(\Delta\emptyset_p) \quad (2.6)$$

Equation (2.3) can be expressed utilizing (2.6) as:

$$\sum_{p=1}^{N} \sigma_p \cos\left(\omega_{RF} t + \Delta\emptyset_p\right) = r_\sigma \cos(\omega_{RF} t + \theta_\sigma) \tag{2.7}$$

Employing equation (2.7), the total transmission becomes:

$$f(t) = \frac{1}{2^q} \sum \rho_\alpha exp\{imr_\sigma \cos(\omega_{RF} t + \theta_\sigma)\} \tag{2.8}$$

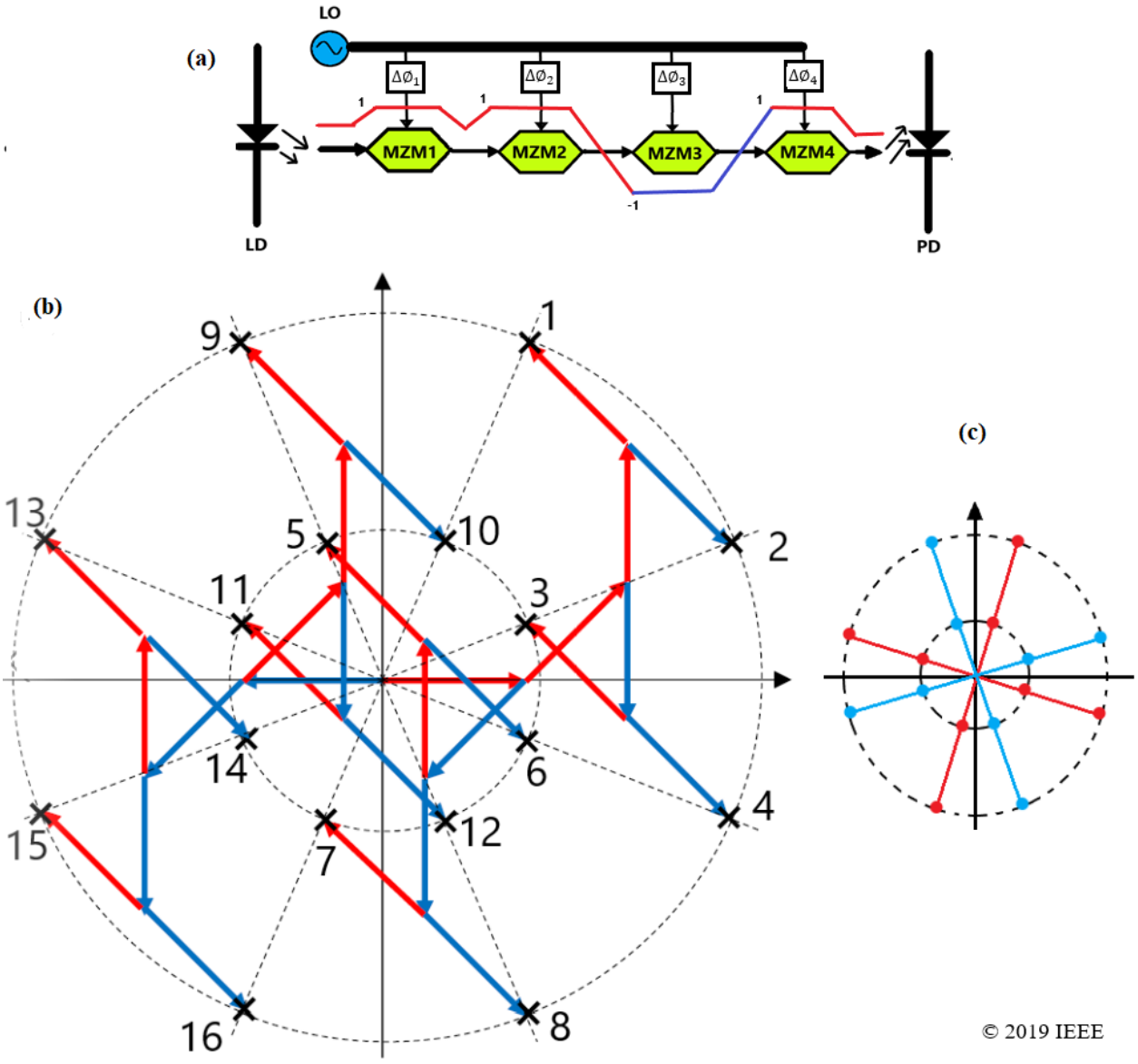


Figure 2.1 (a) Schematic diagram of the proposed frequency octupling architecture. LD: laser diode; PD: photo-diode; LO: local oscillator, (b) Argand diagram showing 16 paths of the parallel equivalent architecture where each segment represents the individual arm's RF phase and the phase information of it being differentially driven. Red defines $\sigma_p = 1$ and blue defines $\sigma_p = -1$, (c) The summation of the phasors lies on the same path forms a constellation of 16 points. For MITP bias, red defines $\rho_\alpha = 1$, blue defines $\rho_\alpha = -1$.

The analysis above implies that on each optical path, the light's encounter with the phase modulators representing each arm of the MZM can be modelled as a phasor on an Argand diagram. The RF drive amplitude and phase represent the magnitude and argument of the phasor. The transmission over one optical path can be taken as a summation of its corresponding phasors. Figure 2.1(a) shows the proposed architecture of frequency 8-tupling technique. An optical path is traced through the circuit which is represented by path number 3 on the argand diagram shown in Figure 2.1(b). The optical biasing condition of each path is shown in Figure 2.1(c). The Argand diagram for the phasor sum over all possible paths forms a constellation of 16 points of which 8 points lie on a circle of radius $r_{1+} = 2\sqrt{2}\cos(\pi/8)$ and the remaining 8 points lie on a circle of radius $r_{1-} = 2\sqrt{2}\sin(\pi/8)$, both regularly distributed at angles of $\theta_\sigma = \{\pm\pi/8, \pm 3\pi/8, \pm 5\pi/8, \pm 7\pi/8\}$. The phasors that correspond to the same angle have the same parity, which alternates with angle $\rho_\alpha(\theta) = \{\mp 1, \pm 1, \mp 1, \pm 1\}$ respectively. Taking all paths into consideration to express the transmission of the proposed architecture:

$$\begin{aligned} f(t) = \tfrac{1}{16}\Big[ & exp\left\{imr_{1+}\cos\left(\omega_{RF}t + \tfrac{3\pi}{8}\right)\right\} - exp\left\{imr_{1+}\cos\left(\omega_{RF}t + \tfrac{\pi}{8}\right)\right\} - exp\left\{imr_{1-}\cos\left(\omega_{RF}t + \tfrac{\pi}{8}\right)\right\} + \\ & exp\left\{imr_{1+}\cos\left(\omega_{RF}t - \tfrac{\pi}{8}\right)\right\} - exp\left\{imr_{1-}\cos\left(\omega_{RF}t + \tfrac{5\pi}{8}\right)\right\} + exp\left\{imr_{1-}\cos\left(\omega_{RF}t - \tfrac{\pi}{8}\right)\right\} + \\ & exp\left\{imr_{1-}\cos\left(\omega_{RF}t - \tfrac{5\pi}{8}\right)\right\} - exp\left\{imr_{1+}\cos\left(\omega_{RF}t - \tfrac{3\pi}{8}\right)\right\} - exp\left\{imr_{1+}\cos\left(\omega_{RF}t + \tfrac{5\pi}{8}\right)\right\} + \\ & exp\left\{imr_{1-}\cos\left(\omega_{RF}t + \tfrac{3\pi}{8}\right)\right\} + exp\left\{imr_{1-}\cos\left(\omega_{RF}t + \tfrac{7\pi}{8}\right)\right\} - exp\left\{imr_{1-}\cos\left(\omega_{RF}t - \tfrac{3\pi}{8}\right)\right\} + \\ & exp\left\{imr_{1+}\cos\left(\omega_{RF}t + \tfrac{7\pi}{8}\right)\right\} - exp\left\{imr_{1-}\cos\left(\omega_{RF}t - \tfrac{7\pi}{8}\right)\right\} - exp\left\{imr_{1+}\cos\left(\omega_{RF}t - \tfrac{7\pi}{8}\right)\right\} + \\ & exp\left\{imr_{1+}\cos\left(\omega_{RF}t - \tfrac{5\pi}{8}\right)\right\}\Big] \end{aligned} \tag{2.9}$$

Utilizing Jacobi-Anger expression:

$$\begin{aligned} f(t) = \tfrac{1}{4}\Big\{ & \textstyle\sum_{n=1}^{\infty}[1+(-1)^n][J_{2n}(mr_{1+}) + J_{2n}(mr_{1-})]\cos\left(2n\omega_{RF}t - n\tfrac{\pi}{4}\right) \\ & - \textstyle\sum_{n=1}^{\infty}[1+(-1)^n][J_{2n}(mr_{1+}) + J_{2n}(mr_{1-})]\cos\left(2n\omega_{RF}t + n\tfrac{\pi}{4}\right)\Big\} \\ & \Rightarrow \\ f(t) = \{ & [J_4(mr_{1+}) + J_4(mr_{1-})]\sin(4\omega_{\mathrm{RF}}\mathrm{t}) \\ & -[J_{12}(mr_{1+}) + J_{12}(mr_{1-})]\sin(12\omega_{\mathrm{RF}}\mathrm{t}) \\ & +[J_{20}(mr_{1+}) + J_{20}(mr_{1-})]\sin(20\omega_{\mathrm{RF}}\mathrm{t}) \ldots\} \end{aligned} \tag{2.10}$$

Consequently all harmonics are suppressed including the carrier apart from harmonics with order equal to the odd multiple of 4. Biasing all MZMs at MATP can be employed to perform frequency 16-tupling [104] but then the operating range in terms of modulation index becomes narrow because of the emergence of carrier breakthrough, which can be deduced from Figure 2.1(c). All paths are added with same optical phase so nullification of $J_0(mr_{1\pm})$ cannot be obtained by design.

The analysis described above is not exclusive to the proposed structure. Figure 2.2 shows the application of the proposed Argand diagram method to obtain the transmission functions for three other frequency 8-tupling circuits [46],[57],[103]. It can be observed that each individual circuit has its modulation index weighted differently based on its structure. This relates to the fact that each circuit will operate efficiently in a modulation index range which is different from others. Low RF power can be enabled by engineering this weighting function which is reflected in Figure 2.3.

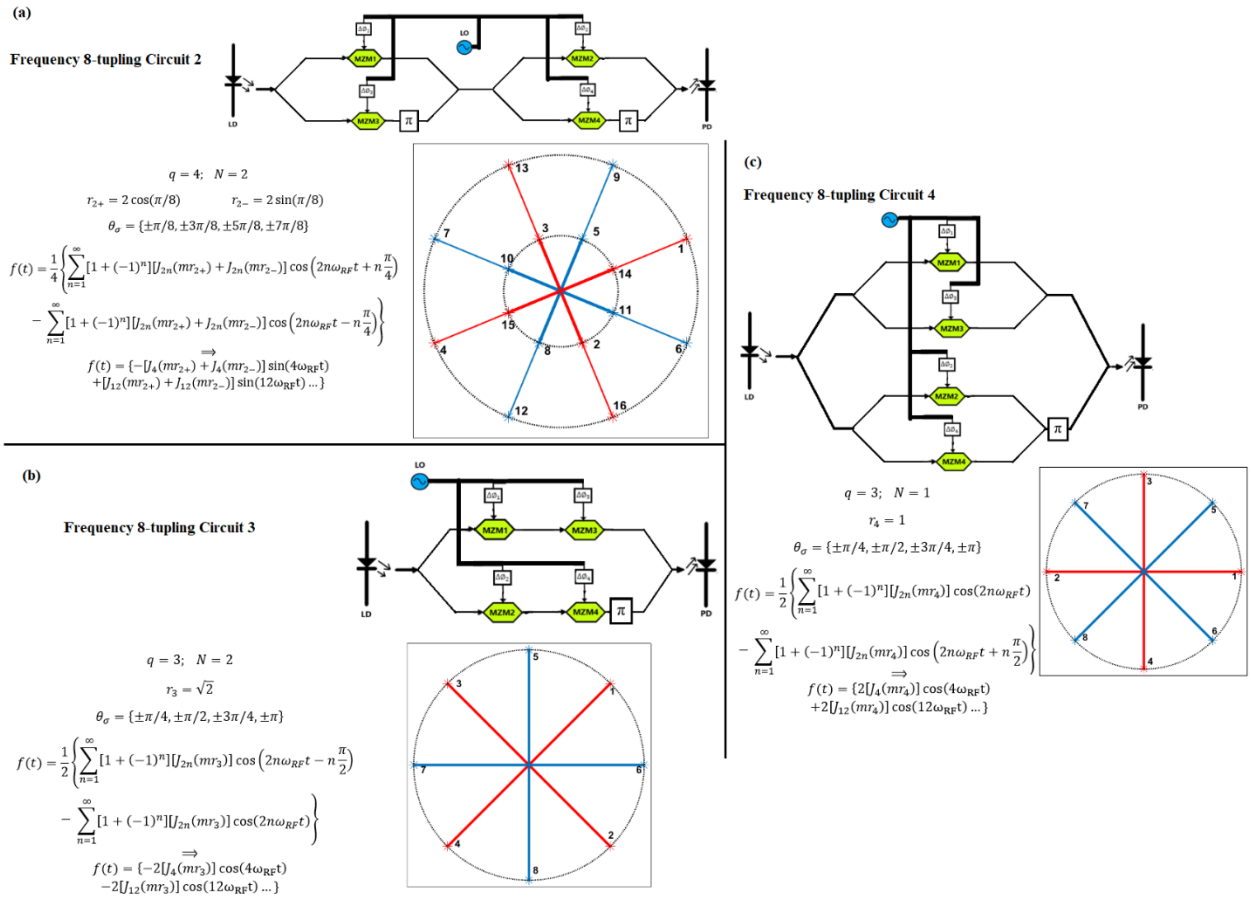


Figure 2.2 Application of Argand diagram to characterize the ideal RF specifications graphically which can be utilized to establish the total transmission function of frequency 8-tupling circuit using (a) two dual-parallel MZM (DP-MZM) is series [46], (b) two dual-stage MZMs in parallel [57] and (c) four MZMs in parallel [103]

Figure 2.3 (a) represents the variation of the coefficients of the principle optical harmonic (e.g. 4$^{th}$

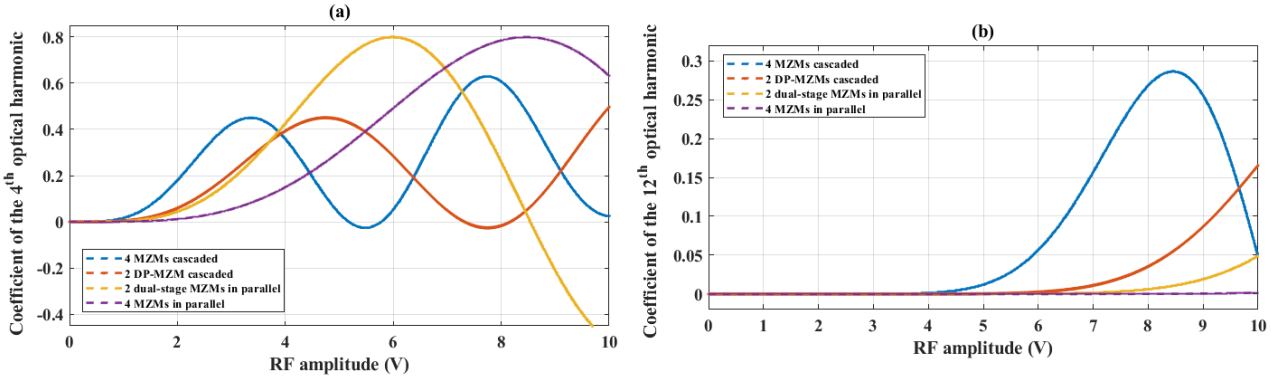


Figure 2.3: Variation of the coefficients of the two major unsuppressed optical harmonics, (a) 4$^{th}$ order and (b) 12$^{th}$ order in terms of the variation of the RF input amplitude. The half-wave voltage $v_\pi$ for each modulator is 5 V

order) of the four circuits. It can be suggested that RF power advantage can be achieved by the proposed architecture as its weighted modulation indices permit its satisfactory operation in the low RF amplitude range compared to others. Figure 2.3(a) shows that frequency octupling operation can be achieved for RF amplitude lower than 2 V. The low optical conversion efficiency and limited range of operation in terms of modulation RF amplitude variation for the proposed circuit is due to the fact that each component of the coefficient $[J_{2n}(mr_{1+}) + J_{2n}(mr_{1-})]$ acts in a reciprocal fashion in certain range of RF amplitude. Figure 2.3(b) shows that frequency 12-tupling operation can also be achieved for lower RF input power than the other architecture, but conditional RF driving is necessary for the suppression of $4^{th}$ order harmonics.

## 2.4 Simulation and Result

The proposed system is simulated using the Virtual Photonics Inc. (VPI) software package. A continuous wave distributed feedback (DFB) laser at a wavelength of 1550 nm with average power of 100 mW is used as the optical input. A 5 GHz sinusoidal RF drive signal is applied to each MZM with appropriate RF phase. RF drive amplitude for the ideal case is taken on the basis of output RF power and spectral purity in terms of electric side harmonic suppression ratio (ESHSR). Low RF frequency for the drive signal is considered to observe a broad frequency response at the output in the limited simulation window. In the ideal case: each MZM is differentially driven with half-wave voltage at 5V and has infinite extinction ratio (80 dB in the VPI simulation). Appropriate DC biasing voltage to maintain corresponding transmission condition is applied to each MZM. A PIN diode with a responsivity of 0.8 A/W is used for detecting the output signal. No optical or electrical filter is employed to suppress unwanted carrier. The simulations are done without using any optical or electrical amplifier.

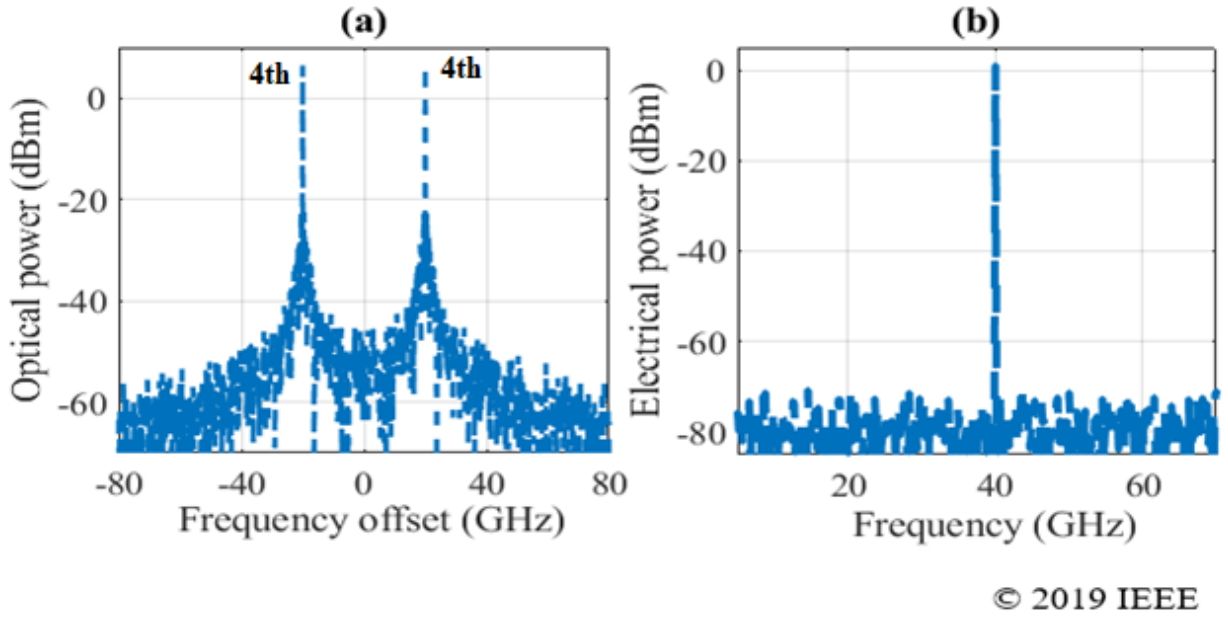



Figure 2.4 (a) Optical spectrum and (b) electrical spectrum of the proposed frequency 8-tupling signal shown in Figure 2.1(a)

The optical and electrical spectra at the output of the configuration are shown in Figure 2.4. As shown in Figure 2.4(a), the power of the two 4$^{th}$ order harmonics is 70 dB higher than that of the other pronounced unwanted harmonics. The optical carrier and all the sidebands except the odd multiple of 4$^{th}$ order are effectively suppressed as predicted by the theoretical approach. After beating at the photodetector, a pristine frequency component at 40 GHz is obtained as shown in Figure 2.4(b).

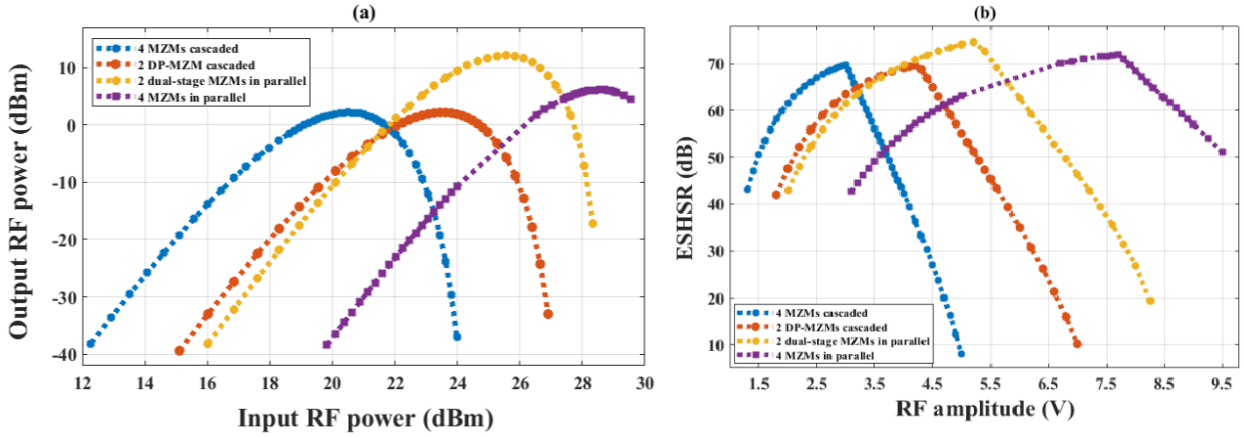


Figure 2.5 Comparison between the proposed cascaded architecture and three other architectures in terms of (a) RF input-output power and (b) ESHSR. The generated output power is calculated for a load resistance of 50 Ω.

A comparison is made among the proposed architecture and three other frequency 8-tupling configurations to evaluate the RF power efficiency [46],[57],[103]. The circuits are chosen based on the criteria that all circuits including the proposed architecture have same number of MZM and identical RF phase condition. Besides theoretically each circuit is capable of suppressing the optical carrier and all the sidebands except the odd multiple of 4$^{th}$ order by design. Small descriptions of each of these circuits with ranges of RF drive voltage and ideal case simulation parameters are presented in Table 2.1. Specifications of the input laser and photodetector are same as the proposed circuit. From Figure 2.5, it can be observed the proposed cascaded architecture biased at MITP can perform more efficiently at low RF input. A wide operating range in terms of modulation index can be obtained while considering both output power and ESHSR. Although the operating range of the proposed circuit which could have an ESHSR exceeding 60 dB is smaller than that of the other configurations, it can be used for a range of input RF power as low as 15 dBm to achieve output power greater than − 25 dBm with ESHSR > 50 dB. A minimum input RF advantage of ~1.7 dB for individual RF drive can be obtained by the proposed architecture. When compared to the circuit with parallel MZMs, the RF advantage is ~6 dB with ESHSR greater than 60 dB.

The RF input power can be lowered further by employing electro-optic modulator with low half-wave voltage [105]. In the simulations, the half-wave voltage is set to 5 V as representative of commercially available $LiNbO_3$ modulators. As can be observed from the Figure 2.5, the other architectures need high RF input power to maintain satisfactory performance which is close to or

Table 2.1: Summary of the circuits from used for comparison. These circuits are also depicted in Figure 2.2

| No | Description | MZM | RF drive amplitude (ideal case) | RF drive phase (ideal case) | Range of RF drive amplitude obtaining ESHSR> 50 dB and output RF power > -25 dB |
|---|---|---|---|---|---|
| 1 | Proposed circuit with four MITP-biased MZM in series. Each MZM has infinite extinction ratio and is differentially driven with half-wave voltage at 5V. The RF drive frequency is 5 GHz. | $MZM_1$ | 3.1 V | 0 | 1.6 V<$V_{RF}$< 3.7 V |
| | | $MZM_2$ | 3.1 V | $\pi/4$ | |
| | | $MZM_3$ | 3.1 V | $\pi/2$ | |
| | | $MZM_4$ | 3.1 V | $3\pi/4$ | |
| 2 | Two DP-MZM are in series where each DP-MZM has its sub MZMs biased at MATP while the outer MZI is biased at MITP. Each MZM has infinite extinction ratio and is differentially driven with half-wave voltage at 5V. The RF drive frequency is 5 GHz [46]. | $MZM_1$ | 4.5 V | 0 | 2.4 V<$V_{RF}$< 5.2 V |
| | | $MZM_2$ | 4.5 V | $\pi/4$ | |
| | | $MZM_3$ | 4.5 V | $\pi/2$ | |
| | | $MZM_4$ | 4.5 V | $3\pi/4$ | |
| 3 | An outer Mach-Zehnder interferometer (MZI) biased at its MITP with each of its two arms containing a pair of MZMs in series; each MZM biased at its MATP. Each MZM has infinite extinction ratio and is differentially driven with half-wave voltage at 5V. The RF drive frequency is 5 GHz [57]. | $MZM_1$ | 5.8 V | 0 | 2.6 V<$V_{RF}$< 6.6 V |
| | | $MZM_2$ | 5.8 V | $\pi/4$ | |
| | | $MZM_3$ | 5.8 V | $\pi/2$ | |
| | | $MZM_4$ | 5.8 V | $3\pi/4$ | |
| 4 | Four MZMs in parallel constitute two DP-MZM in parallel. Each sub-MZM and outer MZI of DP-MZM are biased at MATP. The outer MZI of the whole circuit is biased at MITP. Each MZM has infinite extinction ratio and is differentially driven with half-wave voltage at 5V. The RF drive frequency is 5 GHz [103]. | $MZM_1$ | 6.5 V | 0 | 3.9 V<$V_{RF}$< 9.5 V |
| | | $MZM_2$ | 6.5 V | $\pi/4$ | |
| | | $MZM_3$ | 6.5 V | $\pi/2$ | |
| | | $MZM_4$ | 6.5 V | $3\pi/4$ | |

beyond the half-wave voltage of each modulator. In practical scenario, driving an electro-optic modulator with input greater than the half-wave voltage could lead the appearance of higher order harmonics. In that case, an architecture with low input operating capability is needed to maintain spectral purity.

From Figure 2.3, it has been predicted that the operating range becomes narrower because of the increment of power at $12^{th}$ order optical unsuppressed harmonic and decrement of the $4^{th}$ harmonic. A frequency 24-tupling generation scheme can be achieved in a limited RF input range. The restriction is to suppress the $4^{th}$ harmonic. A pristine RF frequency component at 120 GHz with -39 dBm power can be obtained if the RF drive amplitude is fixed at 5.773 V which is lower than the requirement by the architecture proposed by Hasan and Hall [57].

The simulation results are obtained with the employment of perfectly balanced (50%) optical splitter/coupler with ideal relative phase relationship between ports. Besides, three other circuits [46],[57],[103] have parallel MZMs structure with outer MZI biased at null point. This leads to the addition of optical delay line. Directional coupler or polarization beam combiner followed by polarizer can also be used to achieve the optical biasing condition. These arrangement will introduce additional excess optical loss relative to the proposed cascaded architecture.

A major problem with these architecture is their severe drift in performance in terms of spectral purity when RF phase is subjected to any deviation from their prescribed

values $\Delta\emptyset_p = (p-1)\pi/4 \quad (p = 1,2,3,4)$. Figure 2.6(a) shows an almost identical performance degradation for individual RF drive phase deviation in the proposed architecture. The appearance

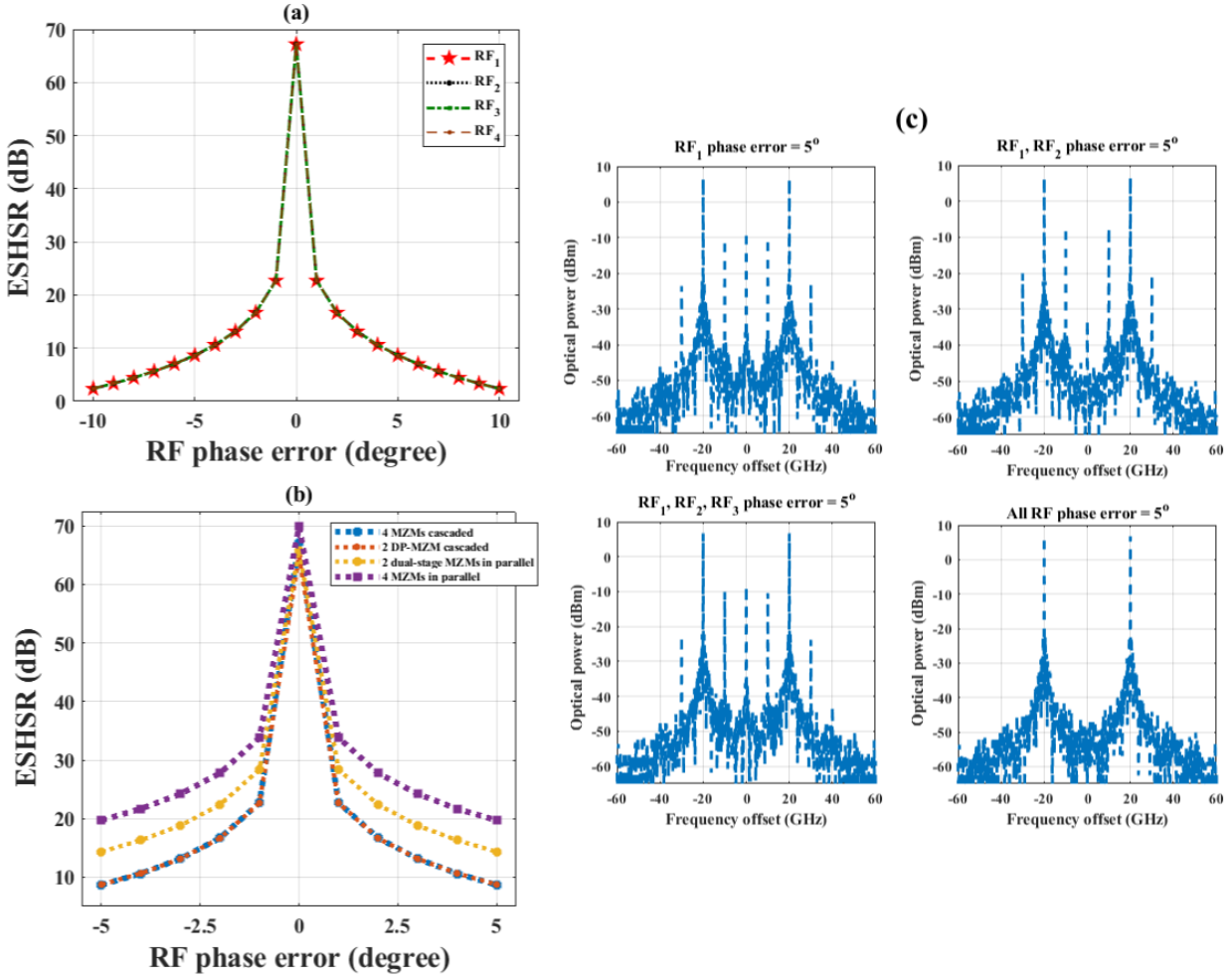


Figure 2.6 (a) ESHSR variation due to RF phase drift in individual RF drive of the proposed architecture; (b) Comparison among the frequency 8-tupling configurations mentioned in Table 2.1 in terms of RF phase drift; (c) Optical spectra at the output of the proposed circuit when multiple RF phases are subjected to same drift. Here, $RF_n = \Delta\varphi_n$

of the carrier and unwanted harmonics leads to lower order frequency component at the output of the photodiode. An ESHSR greater than 20 dB puts a restriction on the RF phase drift to be limited within ±1º. From Figure 2.6(b), it can be observed that the degradation is much more severe in a cascaded architecture which can be expected due to the fact that the sub-periodicity of the transmission function of the cascaded structure is broken as the introduced phase error at each stage would displace the zeros from their ideal position [59]. This results in a loss of complete suppression of the carrier and unwanted harmonics, as shown in Figure 2.6(c). Each optical spectrum depicts the degradation of the spectral purity by the emergence of carrier and even order harmonics when phase drifts are introduced to the RF drives mentioned in the Figure 2.6(c) while the others are at their ideal value. When all MZMs have the same RF phase error, the circuit could retain its ideal spectral characteristics which denotes the fact that the ideal relative phase difference

is vital to maintain satisfactory performance. Zhu et al. reported a filterless 1 × N hybrid RF photonic splitter capable of producing arbitrary phase shift and amplitude ratio which can be implemented to maintain the required RF phase condition [106].

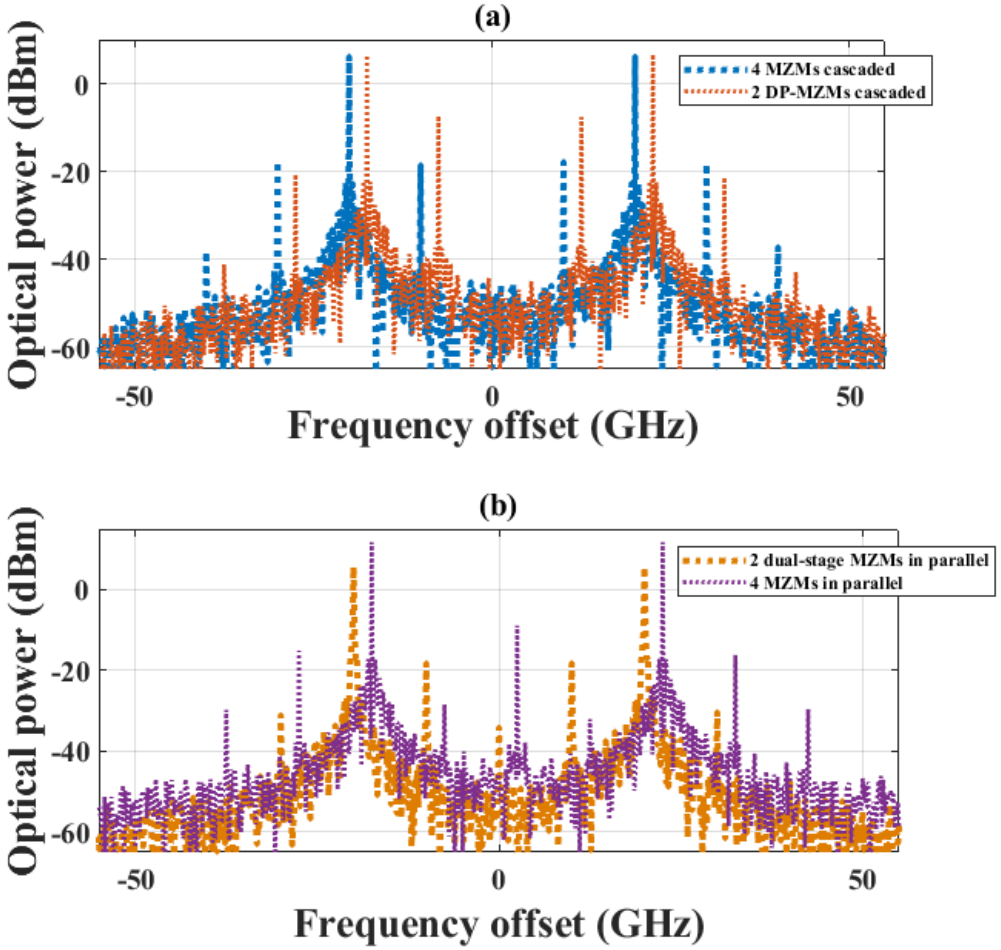


Figure 2.7. Optical spectra of the four frequency 8-tupling architectures when the RF drive amplitude of $MZM_1$ in each circuit has a 10% deviation from the other RF drives amplitude. The spectra of circuit 2 in Figure 2.7(a) and circuit 4 in Figure 2.7(b) is shifted by 2.5 GHz for better visualization. The numbering of the circuits is based on the order representing them in Table 2.1

Suppression of the unwanted harmonics can also be degraded by the RF drive amplitude drift from its ideal value. Figure 2.7 shows the optical spectra of the four frequency 8-tupling architectures mentioned in Table 2.1 for a 10% RF drive amplitude deviation ratio implemented to the $MZM_1$. The RF drive amplitude deviation ratio is defined as $(\Delta v_{RF}/v_{\pi}) \times 100\%$. It can be observed from Figure 2.7 that RF drive amplitude drift leads to the appearance of the undesired harmonics which leads to unwanted RF components at the output of the photodiode. The circuit should be robust to variation in drive magnitude provided the RF drive to be small i.e. not introducing additional zeros. Careful RF drive maintenance is crucial for achieving the ideal functionality which can be obtained by the photonic-integrated microwave phase shifter demonstrated by Porzi et al. which is capable of 360° phase shift over broad bandwidth of more than 6 GHz around an RF carrier flexibly

selectable between 10 and 16 GHz and with the power oscillation is well confined within 0.8 dB [107].

As discussed in the previous section, the non-ideal RF situation cannot be introduced easily in the theoretical approaches utilizing electro-optic modulators due to the emergence of complicated expressions and infinite series containing information of every optical harmonics. In the ideal cases, the complete suppression of various harmonics by design, definite RF phase relation and fixed modulation indices help to assume the spectral behavior of an architecture. Introduction of non-ideal RF conditions complicate the process. In the proposed Argand diagram approach, any RF deviation can be introduced and spectral information can be achieved from the trace of each path in the circuit. This is shown in Figure 2.8.

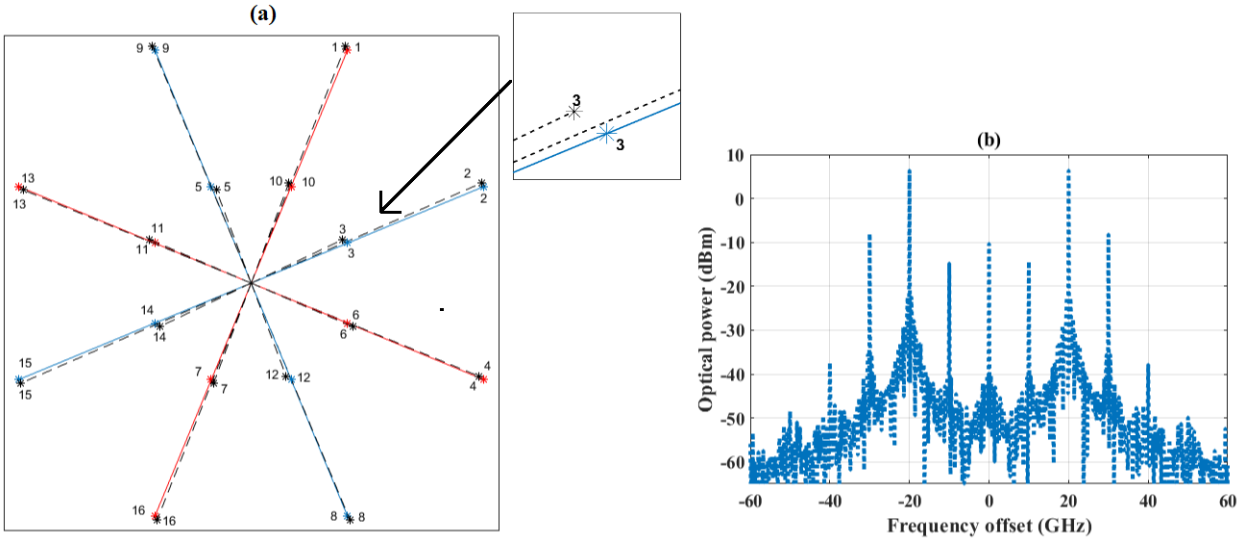


Figure 2.8 (a) The deviation of the optical path vectors from their ideal position a result of the introduction of RF drifts; (b) Optical spectrum showing the effects due the RF drift

As shown in Figure 2.8(a), any arbitrary RF drive drift from its ideal value can be represented by the new traces of each optical path. For the proposed cascaded configuration, any deviation which can be expressed as an RF drive phasor would affect all of the optical paths. Individual path will have a new trace deviated from its ideal position as shown in Figure 2.8(a). An arbitrary case is considered where the RF drive parameters are given: for $MZM_1$, $v_{RF1}$=2.725 V, $\Delta\emptyset_1$=0º; for $MZM_2$, $v_{RF2}$=3.1 V, $\Delta\emptyset_2$=48º; for $MZM_3$, $v_{RF3}$=3.8 V, $\Delta\emptyset_3$=89.2º and for $MZM_4$, $v_{RF4}$=3.1 V, $\Delta\emptyset_4$=135º. An ideal case with $v_{RFn}$=3.1 V and $\Delta\emptyset_p = (p-1)\pi/4 \quad (p = 1,2,3,4)$ can generate an optical spectrum as shown in Figure 2.4(a). The RF drive deviations are responsible for the appearance of unwanted harmonics. This situation can be predicted numerically from the magnitude and angle of each trace which can be applied in the total summation with the introduction of optical information to get the total response. A MATLAB script presented in Appendix II can be utilized to derive the transmission of the circuit for both ideal and non-ideal condition.

Another non-ideal situation involves the DC bias drift. The DC bias needed to maintain the desired transmission point of the MZM is a major factor in the suppression of odd harmonics in the

proposed function. The performance degradation in terms of optical sideband suppression ratio (OSSR) is shown in Figure 2.9(a). OSSR is defined as the difference of power between the desired optical harmonic and the most significant (in terms of power) unwanted optical harmonic in the upper sideband of the optical spectrum. The DC bias drift is defined as $(\Delta V_{DC} / v_{\pi}) \times 100\%$. The drift is applied to one MZM of each circuit mentioned in Figure 2.9(a) and they show similar characteristics. Lin et al. experimentally demonstrated a 30 dB OSSR degradation with a 25% bias

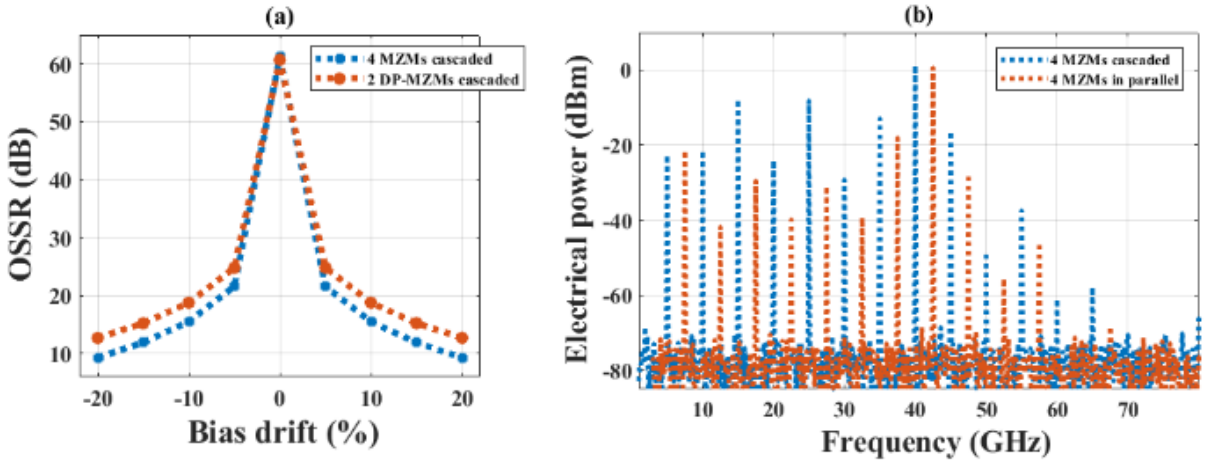


Figure 2.9 (a) OSSR deviation due to the variation of the DC bias; (b) RF spectrum at the output of photodiode when a 20% DC bias drift is applied to $MZM_1$ of each circuit. The spectrum of the circuit with parallel MZMs is shifted by 2.5 GHz for better visualization

drift applied at all of DP-MZM stages of the architecture [46]. In terms of the power at the unwanted RF harmonics, circuit 4 of Table 2.1 shows a little better performance where the proposed configuration shows higher power at the undesired RF harmonics. DC bias can be translated to optical phasor component which can be incorporated in the analysis using Argand diagram to predict the spectral behavior.

Utilizing bias feedback control circuit to limit the bias drift within ±5%, the OSSR can be maintained at values greater than 20 dB which is sufficient for most millimeter-wave application [108]. DC bias free intensity modulator utilizing polarization modulator followed by polarizer can replace the MZM of the circuit to avoid the drift [59]. But this approach is hardly integrate-able and so the circuit should be assembled from discrete components. In the case of high refractive index contrast photonic integration platforms, the commercially available MZM with DC bias can be replaced by the static phase bias-less MZM proposed by Hasan et al. which utilizes the intrinsic phase relations of multi-mode interference couplers [109].

Figure 2.10 shows the relationship between the extinction ratio of MZM and spectral response of the frequency 8-tupling circuits mentioned in Table 2.1. As can be seen from Figure 2.10(a), when all MZMs have same extinction ratio, the proposed circuit can maintain a flat response in terms of ESHSR whereas the other circuits show degradation in their performance. The symmetry condition attained by the proposed architecture is responsible for the cancellation of the spurious harmonics at the RF spectrum. From Figure 2.10(c), it can be observed that this cancellation depends on the

phase of the spurious harmonics at the optical spectrum while other configurations suffer from the unwanted frequency components in the RF spectrum. Randomizing the extinction ratio among the MZMs can break the symmetry which can be observed in Figure 2.10(b). In this situation, the extinction ratio of one MZM ($MZM_1$) is being varied while other MZMs have their extinction ratio fixed at 25 dB. $MZM_1$ is chosen so that the effect of propagation of the imbalance through the whole cascaded architecture can be observed. The MZM which has the same RF specification is also chosen for other circuits for comparison. A sharp transition from its ideal response is observed.

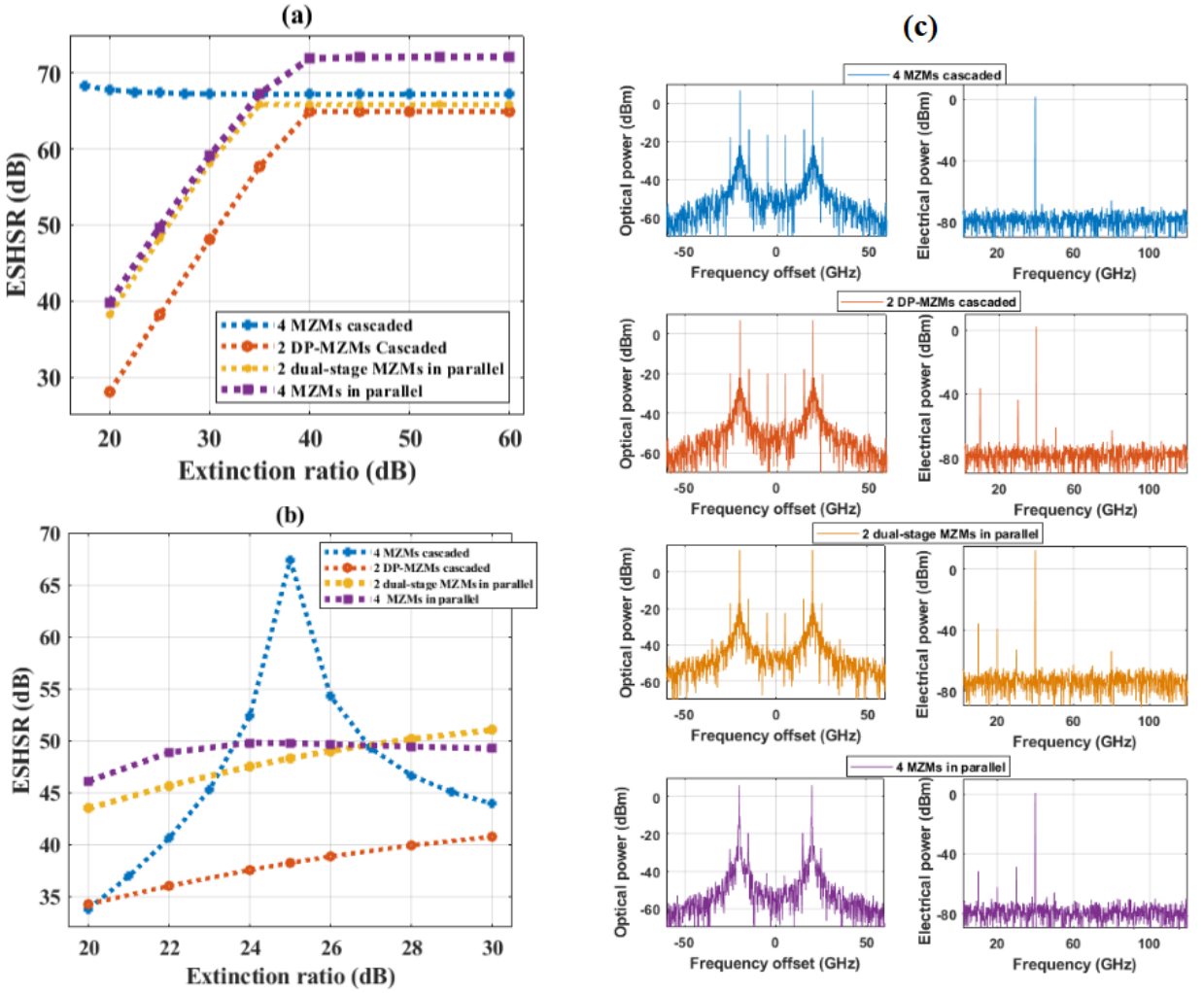


Figure 2.10 ESHSR variation due to the variation of extinction ratio of (a) all MZM, (b) one MZM ($MZM_1$) while other has extinction ratio fixed at 25 dB; (c) Optical and electrical spectrum of the four configurations while each MZM has an extinction ratio of 25 dB

ESHSR greater than 30 dB can be achieved for the range of extinction ratio shown. The symmetry can be exploited in integrated MZM application. The integration of large number of MZM in cascade has been demonstrated where 15 Mach-Zehnder interferometers with 30 thermo-optic phase shifters integrated into a single photonic chip which is electrically and optically interfaced for arbitrary setting of all phase shifters [110]. The trimming strategies emerging in the field of

universal linear optics may be applied to design the extinction ratio of each MZM into close coincidence [111].

Construction of the proposed circuit using discrete components will increase the optical loss due to the introduction of insertion loss at each stage. The commercially available MZM has insertion loss of 3-5 dB in which the major contributor is fiber coupling loss. Besides, the RF phase error effect can be degraded more if the length of the waveguides connecting RF drive to the modulators are mismatched. In addition to the mature $LiNbO_3$ technology, any material platform that offers linear electro-optic modulators can be utilized for fully integrating implementation of the proposed architecture. One of the major advantage of this circuit is its simplicity. A cascaded configuration without any extra coupler/splitter or outer MZI structure favors a compact design with less fabrication difficulty. Development in electro-optic phase modulator in $LiNbO_3$ [112], silicon [113], III-V [105], $BaTiO_3$ [114] platforms augurs very well that the proposed circuit architecture is practical.

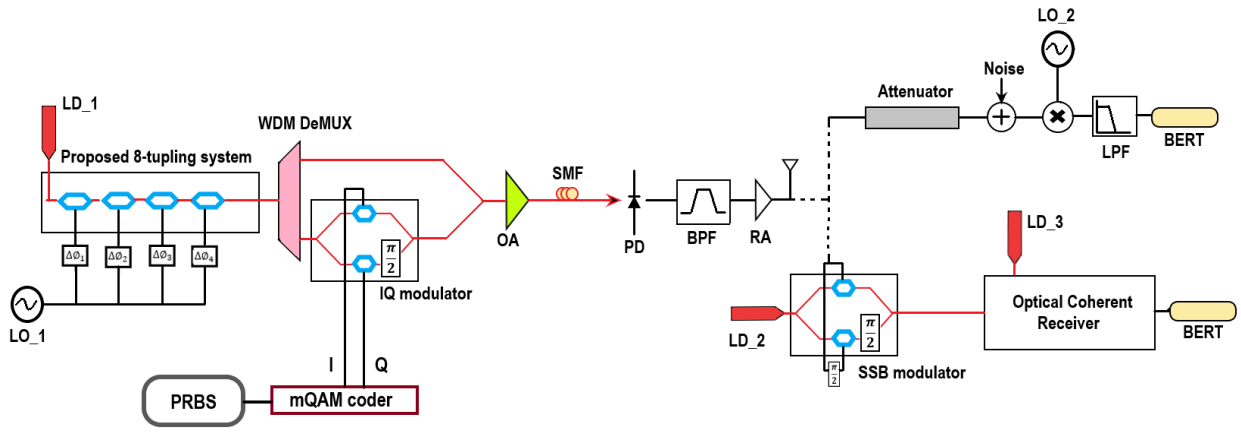


Figure 2.11.Application of the proposed architecture in a radio-over-fiber downlink. LD: laser diode, LO: Local oscillator, OA: Optical amplifier, PD: Photodetector, SMF: Single mode fiber, BPF: Band pass filter, RA: RF amplifier, LPF: Low pass filter, BERT: Bit error rate tester

To illustrate the proposed circuit's application in a RoF system, a numerical simulation of a downlink carrying 10 Gb/s QPSK signal has been implemented. The downlink is complemented by two separate uplink systems. The uplink system are not optimized and they are utilized to evaluate the validity of the adoption of the proposed circuit in a RoF downlink. The adopted architecture for the downlink and the uplink is illustrated in Figure 2.11 and corresponding component specifications utilized in the simulation are mentioned in Table 2.2. In the downlink, the input light is externally modulated by a 5 GHz RF signal and an optical output with two-tone separated by 40 GHz is achieved from the proposed octupling architecture. A WDM demultiplexer is used to separate the two harmonics. A 10 Gbit/s QPSK signal is generated from pseudo random binary sequences (PRBS) of period $2^{15}$-1. This baseband signal modulates the upper sideband in a conventional I/Q modulator. The output of the modulator is then combined with the un-modulated optical carrier at the lower sideband using a 2×1 MMI or Y-combiner. The combined signal is then transported from the transmitter central office (CO) to the remote base station (BS) through a span of single mode optical fiber. An mm-wave carrier of 40 GHz is generated at the BS by the

heterodyne beating of the two components of the combined signal into a photodetector with a sufficient frequency bandwidth. Hence the information signal (PRBS in this case) is imprinted on the 40 GHz carrier. The modulated carrier is then amplified and filtered through a band-pass filter having center frequency at 40 GHz with a bandwidth equal to the 1.5 times the bit rate. The corresponding signal is then transmitted by antenna to provide the down-link of a wireless access system. In this simulation, the wireless link is emulated in one uplink approach (RF uplink) by using an attenuator with a given amount of loss and a Gaussian noise source is used to set the noise floor referred to the input of the receiver. In another uplink (optical uplink), the information channel is converted back to the optical domain after a single sideband modulation scheme. In this case, the intensity of a CW laser is externally modulated by the intermediate frequency (IF) signal at 60 GHz and analyzed through an optical coherent receiver.

Table 2.2: Summary of component specifications utilized in the numerical simulations (simulation parameters are not optimized)

| | Component | Specifications |
|---|---|---|
| Downlink | Continuous-wave DFB laser$_1$ | Emission frequency: 193.1 THz<br>Linewidth: 500 kHz |
| | RF local oscillator$_1$ | Amplitude: 3.1 V<br>Frequency: 5 GHz |
| | Frequency octupling circuit's MZM | MITP biased with $V_\pi$ = 5 V<br>Extinction ratio: 20 dB |
| | WDM demultiplexer | Channel center frequencies: 193.08 GHz and 193.12 GHz<br>3dB filter bandwidth: 20 GHz |
| | I/Q modulator's MZM | Extinction ratio: 25 dB<br>$V_\pi$ = 5 V |
| | Optical amplifier before SMF | Gain: 20 dB |
| | SMF span | Attenuation: 0.2 dB/km<br>Dispersion parameter: 16 ps/(km.nm) |
| | Photodetector | Type: PIN<br>Responsivity: 1A/W |
| | Bandpass filter | Center frequency: 40 GHz<br>Frequency bandwidth: 15 GHz |
| RF uplink | RF amplifier | Gain: 10 dB |
| | RF local oscillator$_2$ | Amplitude: 0.2 V<br>Frequency: 40 GHz |
| Optical uplink | SSB modulator's MZM | $V_\pi$ = 5 V<br>Extinction ratio: 50 dB |
| | Continuous-wave DFB laser$_2$ | Emission frequency: 193.1 THz<br>Average power: 20 kW<br>Linewidth: 500 kHz |
| | Continuous-wave DFB laser$_3$ | Emission frequency: 193.14 THz<br>Average power: 10 kW<br>Linewidth: 800 kHz |

Figure 2.12(a) demonstrates the dependence of error vector magnitude (EVM) and symbol error rate (SER) on signal to noise ratio (SNR) when the mm-wave signal is received by the RF uplink. For an SNR of 15 dB, an EVM of 14.8% and SER of $10^{-11}$ are observed. An almost identical dependence of SER on received power at the optical uplink between two cases where extinction

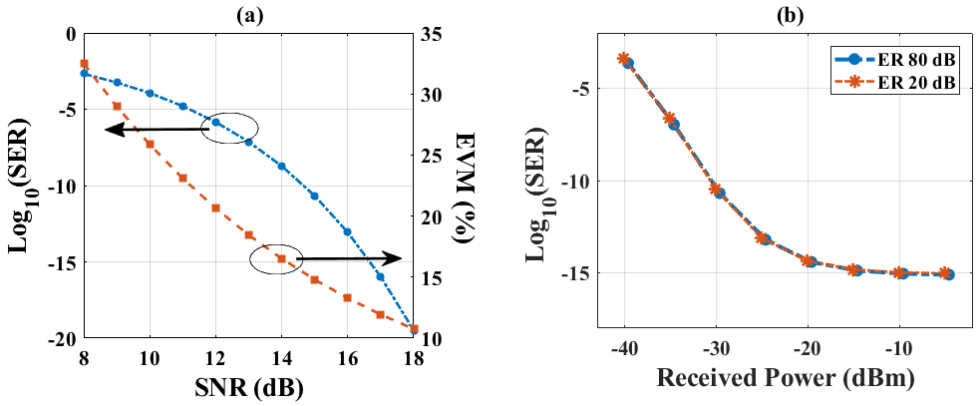


Figure 2.12 RoF system performance illustrated through the corresponding (a) error vector magnitude (EVM) and symbol error ratio (SER) plots of the RF uplink and (b) symbol error ratio plot of the optical uplink with two different extinction ratio for the MZM in the frequency octupling circuit.

ratio of each MZM of the octupling architecture is kept either infinity (80 dB in VPI simulation) or 20 dB is shown in Figure 2.12(b). This represents that the finite extinction ratio of the MZM at the frequency multiplication circuit does not have acute adverse impact on symbol error rate in the described optical coherent system and thus no significant power penalty is introduced.

## 2.5 Summary

In summary, an optical millimeter wave generation architecture is proposed as an energy efficient method with 1.7-6 dB RF advantage compared to functionally equivalent circuits. The functionality of the circuit can be given an exact analytical form using a generalized graphical method. The circuit requires no optical or electrical filtering and satisfactory performance can be obtained over a moderate range of modulation index at low RF operation. A system simulation depicts its validity as an mm-wave generation scheme for a RoF system. Although the simulation parameters are not optimized to improve the results or reflect the real-time situation perfectly, it can be concluded that due to its simple architecture and low RF drive requirement, the proposed architecture in its integrated format can be a candidate to provide access to millimeter-wave band.

# Chapter 3. Frequency Multiplication using Polarization Modulator

## 3.1 Introduction

One of the key ingredients of the radio-over-fiber (RoF) paradigm needed to meet the demand of future broadband wireless access is efficient and cost-effective schemes for the generation and transmission of millimeter-wave (mm-wave) signals. Conventional electrical millimeter-wave generation schemes are costly and complicated due to the limited frequency response of electronic devices and the involvement of multi-stage frequency multiplication. Owing to its conceptual simplicity, the remote heterodyne beating of two phase correlated optical wavelengths impinging onto a high speed photodetector is a feasible approach that facilitates the generation of frequency tunable mm-wave carriers. Among different techniques such as optical heterodyning using mode-locked lasers [116], optical injection locking [100], optical phase locked loop (OPLL) [29] optical nonlinear effect of stimulated Brillouin scattering (SBS) [117] and four wave mixing (FWM) [43], the frequency multiplication based on optical external modulation of a single wavelength laser source is proven to have higher spectral purity, simplicity, stability and the reduction of the local oscillator (LO) frequency required.

For the past two decades, researchers have proposed several techniques based on optical external modulation incorporating Mach-Zehnder modulator (MZM), Sagnac loop, polarization modulator (PolM), phase modulator (PM). A selected list of publication employing external modulation for mm-wave generation with different multiplication factors has been presented in table-1.1. The conventional choice for modulator is the Mach-Zehnder interferometer based modulator because of its integration feasibility and established fabrication facilities. The mature $LiNbO_3$ material platform has already delivered commercial high speed Mach-Zehnder modulator technology. In addition, recent developments of electro-optic phase modulators utilizing other technologies such as silicon, III-V, $BaTiO_3$ or organic thin-films on Si have enabled the realization of mm-wave generation in a compact photonic integrated format.

The conventional MZI structure requires a suitable integration platform for implementation as it is sensitive to the path-length errors between its arms. The schemes using MZMs based on mature $LiNbO_3$ technology suffer from DC bias drift which results in unstable desired sideband power and poor undesired sideband suppression. Hence recently, polarization modulator (PolM) based optical millimeter wave generation has attracted greater attention of researchers due to its bias-free operation, high extinction ratio and robustness to path-length error. Another great advantage of in-line polarizing optics is that it is robust to environmental perturbations even if it is assembled from discrete components. Besides, an integrate-able electro-optic PolM on GaAs platform has been demonstrated having ultra-high-speed operation and lower differential group delay [118]. Photonic frequency multiplication based mm-wave generators employing a dual parallel polarization modulator (DP-PolM) with multiplication factor of two [37]; four and eight [47]; a single PolM in a Sagnac loop providing multiplication factor of four [40]; and two cascaded PolMs enabling tunable multiplication factor [52] have been demonstrated.

This chapter addresses two architectures capable of mm-wave generation. The first architecture involves a dual-parallel structure with each arm containing two cascaded PolMs with analyzers between a Y-power splitter at the input and a polarisation beam combiner and polarizer at the

output. The second single arm architecture consists of four polarization modulators (PolM) in series, each followed by a polarizer (Pol). Both circuits can perform as an optoelectronic method of microwave frequency octupling for a broad range of modulation index. The optical carrier and all sidebands except for harmonics of order equal to an odd integer multiple of four are suppressed without the necessity of any optical or electrical filter or careful adjustment of RF drive voltage. The second circuit offers additional RF power advantages. The robustness of the circuit is also verified by taking different non-ideal factors into consideration.

## 3.2 Contribution

The results provided in the following part of this chapter are published in the Journal of Modern Optics. In the paper, the first architecture mentioned above has been proposed. A theoretical analysis with simulation results showing the performance of the circuit in ideal and non-ideal conditions in terms of optical sideband suppression ratio (OSSR) and electrical side harmonic suppression ratio (ESHSR) have been presented. I drafted the paper, performed the simulations and contributed the original ideas by performing the theoretical analysis using transfer matrix method and evaluated the overall performance of the circuit by considering different non-ideal factors such as deviation in polarizer angle, RF drive phase to attain insight of their practicalities. Mehedi Hasan provided advice on the circuit diagram. Dr. Karin Hinzer and Dr. Trevor Hall were the principal investigators that formulated the research project. Dr. Hall contributed to the theory, provided advice on the interpretation of the results and helped revise the manuscript.

## 3.3 Filterless Frequency Octupling Circuit using Dual Stage Cascaded Polarization Modulators

The following section is a reproduction with permission of an article published in the Journal of Modern Optics [119].

G. M. Hasan, M. Hasan, K. Hinzer, T. Hall, "Filterless frequency octupling circuit using dual stage cascaded polarisation modulators," Journal of Modern Optics, 66:4, pp. 455-461, December 2018, DOI: 10.1080/09500340.2018.1555292

JOURNAL OF MODERN OPTICS
https://doi.org/10.1080/09500340.2018.1555292

Taylor & Francis
Taylor & Francis Group



# Filterless frequency octupling circuit using dual stage cascaded polarization modulators

Gazi Mahamud Hasan, Mehedi Hasan, Karin Hinzer and Trevor Hall

Photonic Technology Laboratory, Centre for Research in Photonics, University of Ottawa, Ottawa, Canada

**ABSTRACT**

This paper demonstrates the photonic generation of millimetre-wave carriers by frequency octupling of a radio frequency (RF) carrier using a circuit with two parallel arms each containing two polarization modulators in series. The low RF drive power required and the absence of optical filters make this architecture suitable for generating highly stable and tunable optical millimetre-waves. A transfer function representation is used to analyse the operation and a simulation using Virtual Photonic Inc. software package is presented as a proof of concept. The simulation results show very high unwanted optical and electrical side harmonic suppression ratio for a wide range of modulation index compared to the prior art. Further, considering the practical scenario, operating tolerance against the imbalances in the key parameters is established. The unwanted RF sidebands are more than 19 dB and 30 dB below the desired signal power even when a deviation of $\pm 3^{\circ}$ is considered in individual RF phase and polarizer angle respectively.

**ARTICLE HISTORY**
Received 30 August 2018
Accepted 29 November 2018

**KEYWORDS**
Optical millimetre wave generation; frequency octupling; polarization modulator; polarizer

## Introduction

One goal of future communication systems such as 5G is the delivery of multi-Gb/s services to customers. As a consequence, deployment of high capacity wireless communication networks is in demand to deliver such super broadband services and to support ever-growing data traffic from wireless mobile customers. The capacity of the systems can be expanded only with the use of a suitable broadband frequency spectrum. The congested lower frequency bands enforce the use of the millimetre wave band which lies in between 30 and 300 GHz. With a 270 GHz bandwidth, it can support a substantially larger traffic volume compared to today's technology. Nevertheless, millimetre wave generation using conventional electronics is costly and complicated due to the limited frequency response of electronic devices and the involvement of multi-stage frequency multiplication. The spectral purity is deteriorated by the emergence of undesired harmonics in the multiplication process. Optical millimetre wave signal generation techniques are becoming more attractive because they offer broad bandwidth, high stability and tunability.

For the past two decades, researchers have proposed several techniques for the generation of optical mm-waves, among them frequency multiplication based on external modulation has gained much attention due to its higher spectral purity, simplicity, stability and the reduction of the local oscillator (LO) frequency required. Many frequency multiplication factors have been demonstrated using external modulators which include frequency doubling (*1*), tripling (*2*), quadrupling (*3*–*5*), sextupling (*6*), octupling (*7*–*20*), 12-tupling (*21*) and 24-tupling (*13*,*17*). In the quest of a frequency octupling function performing with a higher degree of tunability and stability, circuits incorporating Mach–Zehnder modulators (MZM), a Sagnac loop, polarization modulators (PolMs) and multimode intereference (MMI) coupler are proposed. In (*7*), a photonic frequency octupling system based on integrated nested MZM was proposed where modulation indices of the two sub-MZMs should be restricted to 2.405 or 5.52 to suppress the optical carrier. In (*9*), another scheme utilizing two MZMs and a tunable optical phase shifter was proposed and experimentally demonstrated with electrical side harmonic suppression ratio (ESHSR) of 10.5 dB. The operation is limited by the restriction on the modulation index to be 1.699 or the utilization of a fixed fibre Bragg grating (FBG) notch filter to suppress the optical carrier.

Frequency octupling techniques based on two frequency quadrupling systems placed in cascade or in parallel (*8*,*11*); cascading one MZM and one Dual-Parallel MZM (DPMZM) (*12*); four MZMs (eight phase

**CONTACT** Gazi Mahamud Hasan Photonic Technology Laboratory, Centre for Research in Photonics, University of Ottawa, Advanced Research Complex of the University of Ottawa (ARC), 25 Templeton St, Ottawa, ON, Canada K1N 7N9

modulators) in parallel placed between two 4 × 4 MMI couplers (*13*); and a Mach–Zehnder interferometer with each arm containing two cascaded MZMs (*17*) have been proposed. Schemes utilizing a DPMZM in a Sagnac loop (*15*) or cascaded DPMZM and Sagnac loop (*20*) have also demonstrated a frequency octupling function. The stability of the operations is dependent on the Sagnac loop.

A major limitation of a MZM is a drift of its DC operating point leading to unstable desired sideband power and poor undesired sideband suppression. Hence recently, PolMs based optical millimetre wave generation has attracted the attention of researchers due to the bias-free operation and high extinction ratio of PolMs. In (*16*), a photonic frequency octupling technique based on two cascaded PolMs followed by polarization controllers (PC) and polarizers (Pol) was proposed. By tuning the PCs behind the PolMs to introduce a relative phase shift between the two orthogonal phase modulated lightwaves emanating from the PolMs and passing the lightwaves through 45° oriented polarizers relative to the principle axes of PolMs, two cascaded intensity modulators suppressing odd-order sidebands are realized. The ±4th order sidebands with the suppressed optical carrier are achieved for a very narrow range of modulation indices. Another frequency octupler based on a dual-parallel PolM architecture was proposed where the modulation index is limited to 2.405 to obtain satisfactory performance (*18*). In (*19*), a circuit with a tunable multiplication factor was demonstrated. For specific choices of modulation indices, which necessitate critical adjustment of RF drive level, frequency octupling with optical sideband suppression ratio (OSSR) lower than 16 dB is achieved.

In this work, a circuit with a dual-parallel structure with each arm containing two cascaded PolMs with analysers between a Y-power splitter at the input and a polarization beam combiner and polarizer at the output is proposed to perform a frequency octupling function for a broad range of modulation index. A theoretical analysis with simulation results showing the performance of the circuit in ideal and non-ideal conditions in terms of OSSR and ESHSR are presented. There is no requirement for an optical or electrical filter to suppress the optical carrier or unwanted sidebands. The optical carrier and all sidebands except those with orders equal to an odd integer multiple of four are suppressed. The circuit requires no careful adjustment of modulation index to achieve correct operation of frequency octupling with high OSSR and ESHSR. The robustness of the circuit is also verified by taking different non-ideal factors into consideration.

## Principle

The dual stage cascaded PolM configuration proposed for the frequency octupling is shown in Figure 1. A light input from a CW linearly polarized laser source is split using a Y-splitter and injected into the upper arm and the lower arm of the proposed architecture. The polarization state is controlled by a PC. Each arm consists of two stages in cascade containing one PolM followed by a polarizer. The first and second stages are driven in quadrature by the RF signal. The arrangement of a PolM backed by a polarizer with the specified polarization angle converts

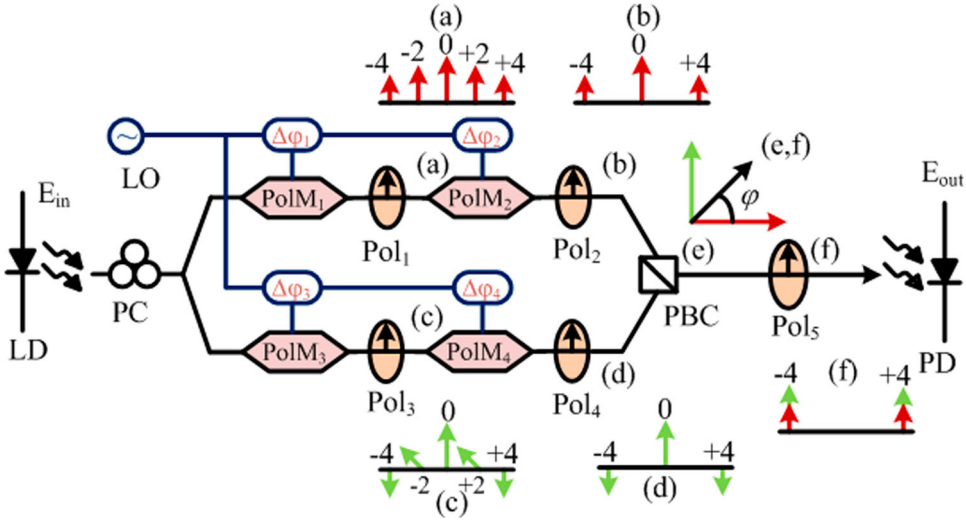


**Figure 1.** Schematic diagram of the frequency octupling circuit using PolM. LD: laser diode; PD: photo diode. In (a–d) and (f), the harmonics with phase information generated by the individual intensity modulator and the final polarizer are shown. In (e,f) the output of the PBC is shown in a polarization diagram.

the PolM to an intensity modulator. The alignment of the state of the polarization of the input light and the polarizer angle relative to the principle axis of the PolM control the biasing condition of the intensity modulator. A selection of 45° determines the PolMs to be biased at their maximum transmission point (MATP). In the sequel it is shown that each arm generates optical sidebands with orders equal to an integer multiple of four alongside the optical carrier. When combined by the outer polarizer with an angle −45° relative to the principle axis of the PolMs, the carrier and even integer multiples of the 4th harmonics are suppressed; only orders equal to an odd integer multiple of four (±4, ±12, ±20 . . . ) are permitted. On photodetection, a high-quality frequency octupled microwave signal is generated.

Consider a pair of PolMs with principal axes aligned with the $x$- and $y$-axes. The amplitude transmission function of a PolM with polarizer (blocks (a–d) in Figure 1) is given by:

$$T = [\cos(\phi)\ \sin(\phi)] \begin{bmatrix} \exp(i\varphi) & 0 \\ 0 & \exp(-i\varphi) \end{bmatrix} \begin{bmatrix} \cos(\theta) \\ \sin(\theta) \end{bmatrix}$$
$$\Rightarrow$$
$$T = \cos(\phi-\theta)\cos(\varphi) + i\cos(\phi+\theta)\sin(\varphi) \tag{1}$$

where $\varphi = \pi v_{\mathrm{RF}}(t)/v_\pi$ is the optical phase shift induced by the RF signal, $v_{\mathrm{RF}}(t)$ is the RF drive voltage, $v_\pi$ is the half-wave voltage of the modulator, $\phi$ is the angle of the polarizer with respect to the $x$-axis and $\theta$ is the linear polarization state of the input light of the PolM with respect to the $x$-axis. Taking $\phi = \pi/4$, $\theta = \pi/4$, the transmission function becomes $T = \cos(\varphi)$ which ensures the MATP biasing condition. Since $\phi = \pi/4$, $\theta = \pi/4$, the output of the polarizer is in the same polarization state as the input of the PolM. It follows that the transmission of the upper arm and lower arm are respectively:

$$T_{ab} = T_a T_b = \cos(\varphi_1)\cos(\varphi_2) \tag{2}$$

$$T_{cd} = T_c T_d = \cos(\varphi_3)\cos(\varphi_4) \tag{3}$$

The output electric field can be written as:

$$E_{\mathrm{out}} = [\cos(\phi_5)\ \sin(\phi_5)] \begin{bmatrix} \cos(\varphi_1)\cos(\varphi_2) & 0 \\ 0 & \cos(\varphi_3)\cos(\varphi_4) \end{bmatrix} \frac{1}{\sqrt{2}} \begin{bmatrix} 1 \\ 1 \end{bmatrix} E_{\mathrm{in}}$$
$$\Rightarrow$$
$$E_{\mathrm{out}} = \frac{1}{\sqrt{2}} E_{in}[\cos(\varphi_1)\cos(\varphi_2)\cos(\varphi_5) + \cos(\varphi_3)\cos(\varphi_4)\sin(\varphi_5)] \tag{4}$$

Taking the polarizer 5 angle as $\phi_5 = -\pi/4$, the output field becomes:

$$E_{\mathrm{out}} = \frac{1}{4} E_{\mathrm{in}}[\cos(\varphi_1-\varphi_2) + \cos(\varphi_1+\varphi_2) - \cos(\varphi_3-\varphi_4) - \cos(\varphi_3+\varphi_4)] \tag{5}$$

Assume that the RF drive voltage is given by $v_{\mathrm{RF}}(t) = V_{\mathrm{RF}}\cos(\omega_{\mathrm{RF}}t + \Delta\varphi_n)$, where $V_{\mathrm{RF}}$ is the peak amplitude, $\omega_{\mathrm{RF}}$ is the RF angular frequency, $t$ is the time and $\Delta\varphi_n$ is the phase shift of the $n$th RF drive introduced to the $n$th PolM. Setting the RF phase shifts to $\Delta\varphi_1 = 0$, $\Delta\varphi_2 = \pi/2$, $\Delta\varphi_3 = \pi/4$, $\Delta\varphi_4 = 3\pi/4$ and applying the Jacobi–Anger expansion, the output field in Equation (5) can be rewritten:

$$E_{\mathrm{out}} = \tfrac{1}{4}E_{\mathrm{in}} \left\{ \begin{array}{l} \left[J_0(m) + 2\sum_{n=1}^{\infty} J_{2n}(m)\cos\left(2n\omega_{\mathrm{RF}}t + n\tfrac{\pi}{2}\right)\right] \\ +\left[J_0(m) + 2\sum_{n=1}^{\infty}(-1)^n J_{2n}(m)\cos\left(2n\omega_{\mathrm{RF}}t + n\tfrac{\pi}{2}\right)\right] \\ -\left[J_0(m) + 2\sum_{n=1}^{\infty}(-1)^n J_{2n}(m)\cos(2n\omega_{\mathrm{RF}}t)\right] \\ -\left[J_0(m) + 2\sum_{n=1}^{\infty} J_{2n}(m)\cos(2n\omega_{\mathrm{RF}}t)\right] \end{array} \right\}$$
$$\Rightarrow$$
$$E_{\mathrm{out}} = \tfrac{1}{2}E_{\mathrm{in}} \left\{\sum_{n=1}^{\infty}[1+(-1)^n]J_{2n}(m)\left[\cos\left(2n\omega_{\mathrm{RF}}t + n\tfrac{\pi}{2}\right) - \cos(2n\omega_{\mathrm{RF}}t)\right]\right\} \tag{6}$$

where $J_p$ is the Bessel function of the first kind of order $p$ and $m = \sqrt{2}\pi V_{\mathrm{RF}}/v_\pi$ is the modulation index. Equation (6) may be simplified and the first few terms evaluated:

$$\begin{aligned} E_{\mathrm{out}} &= -2E_{\mathrm{in}}\sum_{q=0}^{\infty} J_{4(2q+1)}(m)\cos[4(2q+1)\omega_{\mathrm{RF}}t] \\ &\approx -2E_{\mathrm{in}}[J_4(m)\cos(4\omega_{\mathrm{RF}}t) + J_{12}(m)\cos(12\omega_{\mathrm{RF}}t) \\ &\quad + J_{20}(m)\cos(20\omega_{\mathrm{RF}}t) + \ldots] \end{aligned} \tag{7}$$

It can be observed that all the orders are suppressed except the odd multiples of four. From the magnitude of the Bessel functions of order 12 and higher, it can be seen that their contribution is negligible while $m < 7.3$, so frequency octupling can be achieved within this prescribed range of modulation index.

## Results and discussion

The proposed circuit architecture is simulated using the Virtual Photonic Inc. (VPI) software package. Linearly polarized light output from a continuous-wave DFB laser operating at a vacuum wavelength of 1550 nm with a linewidth of 200 kHz and average power of 10 mW is equally split by a Y-splitter and then injected into the upper and lower arms of the circuit. The RF drive frequency is set to 10 GHz and the half-wave voltage for the

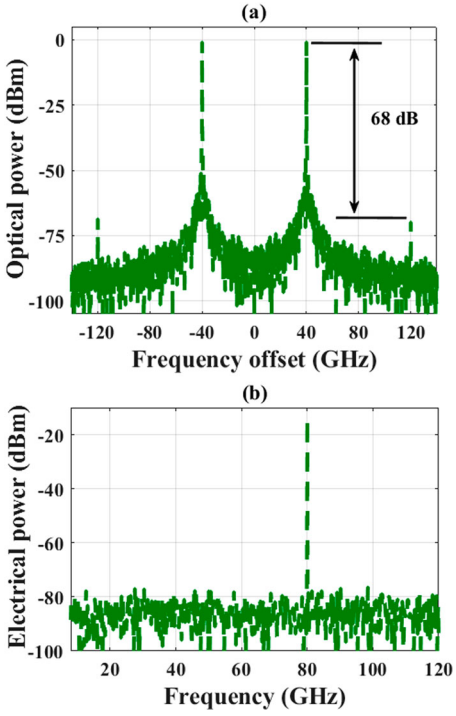


**Figure 2.** (a) Optical spectrum and (b) electrical spectrum of the frequency 8-tupling signal.

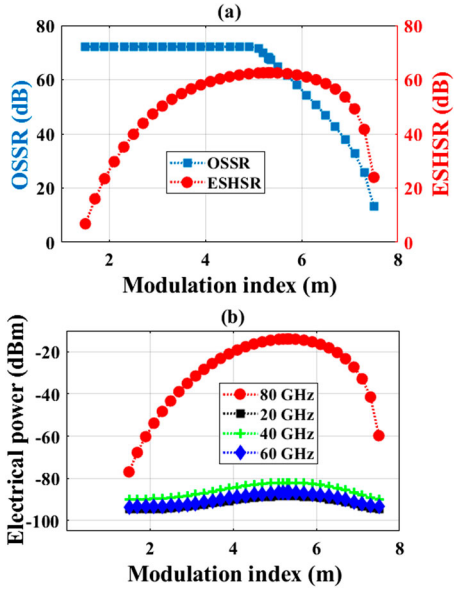


**Figure 3.** (a) Numerically calculated OSSR and ESHSR for a wide range of modulation index. (b) Electrical peak power of the harmonics of interest and unwanted harmonics.

PolM is taken as 1 V. The peak RF voltage is then chosen to be 1.2 V to obtain the maximum electrical power at the output. At each PolM ($\text{PolM}_n$), a RF drive voltage with the specified amplitude and phase shift is applied. In the ideal case to obtain frequency octupling, the light input at each arm is linearly polarized at 45° with respect to the principal axis of the PolM, the Y-splitter is perfectly balanced, the PBC is oriented along the principle axis of the PolMs, the four polarizers at the dual-parallel structure are oriented at 45° and the 5th polarizer behind the PBC is oriented at −45° with respect to the principal axes of the PolMs, the RF phase shifts are exactly equal to the values specified in the theoretical analysis.

Figure 2 shows the optical and electrical spectra at the output of the circuit. As shown in Figure 2(a), the unwanted $12^{\text{th}}$ harmonics at ±120 GHz (12 × 10 GHz) are 67.68 dB smaller than the $4^{\text{th}}$ harmonics at ±40 GHz (4 × 10 GHz) and the other sidebands are completely suppressed by design. After passing through a photodetector with responsivity of 0.8 A/W, the desired beat signal with frequency 80 GHz, eight times that of the RF drive signal, is generated without any significant unwanted harmonics, as shown in Figure 2(b).

In practice, circuit parameters are subject to errors due to the operating environment and component tolerances, hence the expected results may vary from the ideal results due to the introduction of circuit imbalance. Figure 3(a) shows the variations of OSSR and ESHSR due to a variation of modulation index arising from the variation of the peak RF drive voltage while the half-wave voltage of the modulators are taken to be equal and constant. It can be observed that the OSSR is quite constant at 72.166 dB over a range of modulation index. At lower values of modulation index ($m \leq 4.9$), the prominent unwanted harmonics are $5^{\text{th}}$ order harmonics at ±50 GHz. After that, the unwanted $12^{\text{th}}$ order harmonics emerge and cause a deterioration of the OSSR. From the perspective of ESHSR, the circuit can achieve octupling with satisfactory unwanted sideband suppression without careful adjustment of the RF drive to the PolM. Circuit operation with OSSR and ESHSR greater than 20 dB can be obtained for a wide range of modulation index ($1.9 \leq m \leq 7.3$). The relationship among the peak electrical power of the harmonic of interest (80 GHz) and the other unwanted harmonics with even multiple of the RF drive frequency (20, 40 and 60 GHz) for a wide range of modulation index, as shown in Figure 3(b), depicts the complete suppression of unwanted electrical harmonics when modulation index variation is taken into consideration.

OSSR and ESHSR calculated for a constant RF peak amplitude at 1.2V while varying polarizer angle are plotted in Figure 4(a,b). It can be observed that both OSSR and ESHSR are sensitive to the polarizer angle variation. The variation is symmetric with respect to the ideal condition. OSSR and ESHSR with values greater than 30 dB can be achieved when individual polarizer angle deviation is restricted to an interval of ±3° from its ideal value. From the simulation results, drifts in the Polarizer 1 and

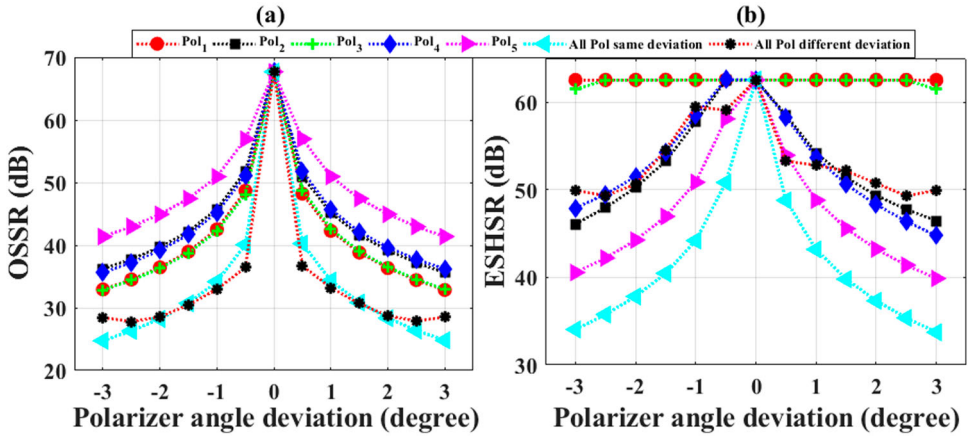


**Figure 4.** Variation of (a) OSSR and (b) ESHSR due to the drift of polarizer angle from ideal condition. When all the polarizers are suffering from different angular deviation, the points on the x-axis represent different cases i.e. $\pm0.5°$ ($\Delta Pol_1 = 0$, $\Delta Pol_2 = \pm0.5°$, $\Delta Pol_3 = \pm1°$, $\Delta Pol_4 = \pm1.5°$, $\Delta Pol_5 = \pm0.5°$), $\pm1°$($\Delta Pol_1 = 0$, $\Delta Pol_2 = \pm1°$, $\Delta Pol_3 = \pm1.5°$, $\Delta Pol_4 = \pm2°$, $\Delta Pol_5 = \pm1°$), $\pm1.5°$($\Delta Pol_1 = 0$, $\Delta Pol_2 = \pm1.5°$, $\Delta Pol_3 = \pm2°$, $\Delta Pol_4 = \pm2.5°$, $\Delta Pol_5 = \pm1.5°$), $\pm2°$($\Delta Pol_1 = 0$, $\Delta Pol_2 = \pm2°$, $\Delta Pol_3 = \pm2.5°$, $\Delta Pol_4 = \pm3°$, $\Delta Pol_5 = \pm2°$), $\pm2.5°$($\Delta Pol_1 = 0$, $\Delta Pol_2 = \pm2.5°$, $\Delta Pol_3 = \pm3°$, $\Delta Pol_4 = \pm2.5°$, $\Delta Pol_5 = \pm2.5°$), $\pm3°$($\Delta Pol_1 = 0$, $\Delta Pol_2 = \pm3°$, $\Delta Pol_3 = \pm2.5°$, $\Delta Pol_4 = \pm2°$, $\Delta Pol_5 = \pm3°$).

Polarizer 3 angle have negligible impacts on the desired $8^{th}$ order RF harmonic since the additional unwanted RF harmonics are more than 60 dB below the desired signal power even when the deviation is $\pm3°$. When all polarizer suffer from the same angle deviation, the situation deteriorates but still circuit operation with greater than 20 dB for OSSR and 30 dB for ESHSR can be attained for a $\pm3°$ polarizer angle variation. To observe more practical situations, simulations are done with different polarizer having different polarizer angle deviation. Each point on the axis defining the deviation of polarizer angle represents different cases. It can be observed that for different deviation, the behaviour of OSSR is similar to the case with the same deviation for all polarizer. Operation with greater that 45 dB for ESHSR can be obtained for all these cases.

Non-ideal phases of the RF drives to the individual PolMs are also considered. Figure 5 shows the almost identical ESHSR variations due to individual RF drive signal phase error. Phase deviation of each RF LO from its ideal condition induces unwanted optical sidebands and corresponding RF sidebands at the detector. However, when the phase deviation is within $\pm3°$, the unwanted RF sidebands are 19 dB lower than the desired component and hence the quality of the generated mm-wave carriers can be maintained even when the individual phase deviation is around $\pm3°$.

To observe the robustness of the configuration to RF phase deviation, any two of the RF phases to the individual PolMs are varied while the others are kept at their ideal condition. Figure 6 shows the dependence of ESHSR on the simultaneous phase deviation at PolM1 and another PolM (PolM2 or PolM3 or PolM4). In

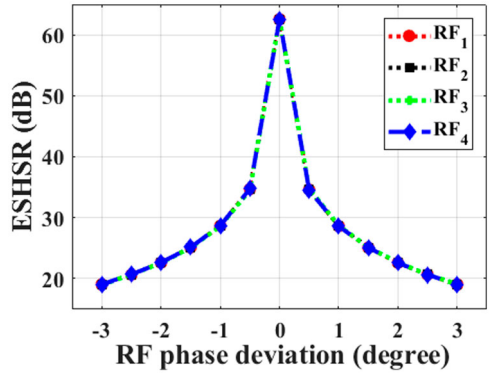


**Figure 5.** ESHSR variation due to the deviation of individual RF drive phase from ideal condition. $RF_n$ represents the RF phase variation of the corresponding $PolM_n$.

Figure 6(a), identical RF phase deviation is applied to the PolM1 and either of the remaining PolMs. It can be observed that the operation is more sensitive to the simultaneous phase error in one arm of the parallel branches. Circuit performance with ESHSR more than 19 dB is achieved when the deviation of RF drive phases of PolM1 and another PolM varies between $-2°$ and $+2°$. Figure 6(b) shown a more practical situation where differential deviation of RF drive phase is applied simultaneously to PolM1 and another PolM. In this case, circuit operation is more sensitive to the phase variations at PolMs in the same branch. In this case, ESHSR of greater than 19 dB can be obtained for a differential phase deviation of $\pm1.5°$ from ideal condition. From the observation, it can be concluded that maintaining RF drive phases at their specific values is critical for successful operation of

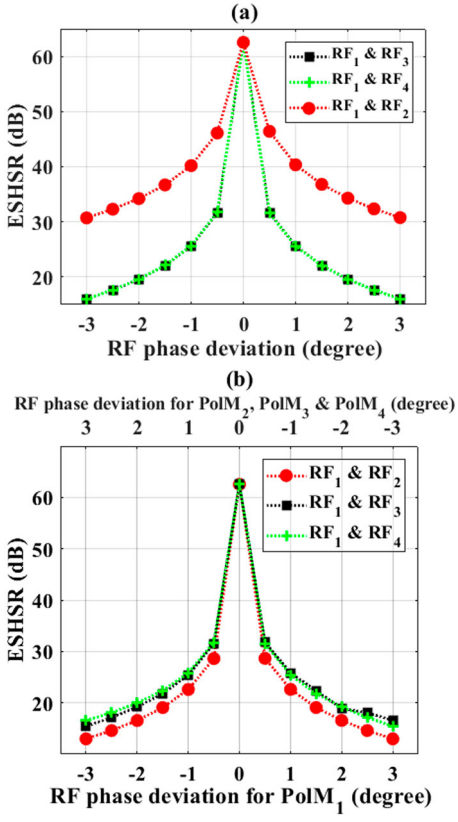


**Figure 6.** ESHSR variation due to the simultaneous phase drift in two RF drives (a) at same direction, (b) at opposite direction. $RF_n$ represents the RF phase variation of the corresponding $PolM_n$.

the proposed circuit. Several approaches can be taken into consideration to maintain precision over RF drive phase. In (*22*), a photonic integrated microwave phase shifter is proposed and experimentally demonstrated to be capable of controlling the phase of microwave signal in a range of more than 360° with a bandwidth of more than 6 GHz around an RF carrier flexibly selectable between 10 and 16 GHz.

## Conclusion

In summary, a photonic circuit consisting of four PolMs and five polarizers has been proposed for implementing frequency octupling and its operation has been theoretically analysed. Computer simulations verify its functionality. The operation of the circuit is not restricted to the careful selection of the amplitude of the drive voltage to maintain higher OSSR and ESHSR. The proposed system can be operated over a modulation index from 1.9 to 7.3, a far wider range than other octupling techniques utilizing PolM (*16*,*18*,*19*). Moreover, the circuit requires no DC bias and no optical filtering for sideband suppression. The effect on the optical and RF sidebands of a variety of non-ideal values of parameters such as RF drive amplitude, phase and the polarizer angles have been evaluated. From the results it is found that the proposed circuit is robust to practical values of component error.

## Disclosure statement

No potential conflict of interest was reported by the authors.

## Funding

Mehedi Hasan acknowledges the Natural Sciences and Engineering Research Council of Canada (NSERC) for their support through the Vanier Canada Graduate Scholarship programme. Karin Hinzer is grateful to D & T Photonics and MITACS for their support through the MITACS accelerate programme. Trevor Hall is grateful to the University of Ottawa for their support of his University Research Chair.

## ORCID

*Gazi Mahamud Hasan* http://orcid.org/0000-0001-9196-5104

## References

(1) O'Reilly, J.J.; Lane, P.M.; Heidemann, R.; Hofstetter, R. Optical Generation of Very Narrow Linewidth Millimeter Wave Signals. *Electron. Lett.* 1992, *28* (25), 2309–2311.
(2) Thakur, M.P.; Medeiros, M.C.R.; Laurencio, P.; Mitchell, J. E. Optical Frequency Tripling with Improved Suppression and Sideband Selection. *Opt. Express.* 2011, *19* (26), B457–B468.
(3) Qi, G.H.; Yao, J.P.; Seregelyi, J.; Paquet, S.; Belisle, C. Optical Generation and Distribution of Continuously Tunable Millimeter-Wave Signals Using an Optical Phase Modulator. *J. Light. Technol.* 2005, *23* (9), 2687–2695.
(4) Lin, C.-T.; Shih, P.-T.; Chen, J.; Xue, W.-Q.; Peng, P.-C.; Chi, S. Optical Millimeter-Wave Signal Generation Using Frequency Quadrupling Technique and no Optical Filtering. *IEEE Photonics Technol. Lett.* 2008, *20* (12), 1027–1029.
(5) Yu, S.; Gu, W.; Yang, A.; Jiang, T.; Wang, C. A Frequency Quadrupling Optical MM-Wave Generation for Hybrid Fiber-Wireless Systems. *IEEE J. Sel. Areas Commun.* 2013, *31* (12), 797–803.
(6) Mohamed, M.; Zhang, X.; Hraimel, B.; Wu, K. Frequency Sixupler for Millimeter-Wave Over Fiber Systems. *Opt. Express.* 2008, *16* (14), 10141–10151.
(7) Ma, J.; Xin, X.; Yu, J.; Yu, C.; Wang, K.; Huang, H.; Rao, L. Optical Millimeter Wave Generated by Octupling the Frequency of the Local Oscillator. *J. Opt. Netw.* 2008, *7* (10), 837–845.
(8) Lin, C.-T.; Shih, P.-T.; Jiang, W.; Chen, J.J.; Peng, P.; Chi, S. A Continuously Tunable and Filterless Optical Millimeter-Wave Generation via Frequency Octupling. *Opt. Express.* 2009, *17* (22), 19749–19756.
(9) Li, W.; Yao, J. Microwave Generation Based on Optical Domain Microwave Frequency Octupling. *IEEE Photonics Technol. Lett.* 2010, *22* (1), 24–26.

(10) Shang, L.; Wen, A.; Li, B.; Wang, T.; Chen, Y.; Li, M. An Optical mm-Wave Generation Scheme by Frequency Octupling Using a Nested MMI. *Opt. Commun.* 2011, *284*, 5618–5622.
(11) Shang, L.; Wen, A.; Li, B.; Wang, T.; Chen, Y.; Li, M. A Filterless Optical Millimeter-Wave Generation Based on Frequency Octupling. *Optik*. 2012, *123*, 1183–1186.
(12) Qin, Y.; Sun, J.; Du, M.; Liao, J. Simplified Optical Millimeter-Wave Generation Configuration Based on Frequency Octupling. *Opt. Commun.* 2014, *315*, 280–285.
(13) Hasan, M.; Guemri, R.; Maldonado-basilio, R.; Lucarz, F.; Tocnaye, J.-L.B.; Hall, T.J. Theoretical Analysis and Modeling of a Photonic Integrated Circuit for Frequency 8-Tupled and 24-Tupled Millimeter Wave Signal Generation. *Opt. Lett*. 2014, *39* (24), 6950–6953.
(14) Gao, Y.; Wen, A.; Jiang, W.; Liang, D.; Liu, W.; Xiang, S. Photonic Microwave Generation With Frequency Octupling Based on a DP-QPSK Modulator. *IEEE Photonics Technol. Lett*. 2015, *27* (21), 2260–2263.
(15) Gao, Y.; Wen, A.; Li, N.; Wu, X.; Zhang, H. Microwave Generation with Photonic Frequency Octupling Using a DPMZM in a Sagnac Loop. *J. Mod. Opt*. 2015, 62 (16), 1291–1296.
(16) Yang, Y.; Ma, J.; Zhang, R.; Zhang, J. Generation of Optical Millimeter Wave Using Two Cascaded Polarization Modulators Based on Frequency Octupling Without Filtering. *Fiber Int. Opt*. 2015, *34*, 230–242.
(17) Hasan, M.; Hall, T.J. A Photonic Frequency Octo-Tupler with Reduced RF Drive Power and Extended Spurious Sideband Suppression. *Opt. Laser Technol.* 2016, *81*, 115–121.
(18) Zhu, Z.; Zhao, S.; Li, X.; Huang, A.; Qu, K.; Lin, T. Photonic Generation of Frequency-Octupled and Frequency-Quadrupled Microwave Signals Using a Dual-Parallel Polarization Modulator. *Opt. Quant. Electron*. 2016, *48* (398). doi:10.1007/s11082-016-0671-2.
(19) Zhu, Z.; Zhao, S.; Tan, Q.; Liang, D.; Li, X.; Qu, K. Photonically Assisted Microwave Signal Generation Based on Two Cascaded Polarization Modulators With a Tunable Multiplication Factor. *IEEE Trans. Micro. Theory Technol.* 2016, *64* (11), 3748–3756.
(20) Zhang, W.; Wen, A.; Gao, Y.; Shang, S.; Zheng, H.; He, H. Filterless Frequency-Octupling mm-Wave Generation by Cascading Sagnac Loop and DPMZM. *Opt. Laser Technol.* 2017, *97*, 229–233.
(21) Shih, P.-T.; Chen, J.; Lin, C.-T.; Jiang, W., Jr.; Huang, H.-S.; Peng, P.-C.; Chi, S. Optical Millimeter-Wave Signal Generation Via Frequency 12-Tupling. *J. Light. Technol.* 2010, *28* (1), 71–78.
(22) Porzi, C.; Serafino, G.; Sans, M.; Falconi, F.; Sorianello, V.; Pinna, S.; Mitchell, J.; Romagnoli, M.; Bogoni, A.; Ghelfi, P. Photonic Integrated Microwave Phase Shifter up to the mm-Wave Band With Fast Response Time in Silicon-on-Insulator Technology. *J. Light. Technol.* 2018, *36* (19), 4494–4500.

## 3.4 Contribution

In the following part of the chapter, the second configuration enabling optical frequency octupling is presented. Its operation is analyzed theoretically using a transfer matrix approach. The theoretical predictions are then validated by the results of computer simulation. These results are published in Optical and Quantum Electronics. I drafted the paper, performed the simulations and contributed the original ideas by performing the theoretical analysis using transfer matrix method and evaluated the overall performance of the circuit by considering different non-ideal factors such as deviation in polarizer angle, RF drive phase to attain insight of their practicalities. Mehedi Hasan provided advice on the circuit diagram. Hongpeng Shang and DeGui Sun replicated and validated the results using different software. Peng Liu gave advices on the setup for practical verification and is providing assistance in experimentation with discrete components. Dr. Karin Hinzer and Dr. Trevor Hall were the principal investigators that formulated the research project. Dr. Hall contributed to the theory, provided advice on the interpretation of the results and helped revise the manuscript.

## 3.5 Energy Efficient Photonic Millimeter-wave Generation Using Cascaded Polarization Modulators

The following section is a reproduction of an article published in Optical and Quantum Electronics [59]

Optical and Quantum Electronics (2019) 51:217
https://doi.org/10.1007/s11082-019-1927-4

# Energy efficient photonic millimeter-wave generation using cascaded polarization modulators

Gazi Mahamud Hasan[1] · Mehedi Hasan[1] · Hongpeng Shang[2] · DeGui Sun[1] · Karin Hinzer[1] · Peng Liu[1] · Trevor Hall[1]

Received: 30 November 2018 / Accepted: 10 June 2019


## Abstract

A filter-less millimeter-wave generation scheme consisting of four polarization modulators in series, each followed by a polarizer is proposed to achieve optoelectronic frequency octupling. The cascade of polarization modulator and polarizer provides an intensity modulator whose biasing condition can be set by the polarizer angle and polarization state of the input light to each polarization modulator. A theoretical analysis of the architecture is performed using a transfer function method and validated by industry-standard software simulation tools. The circuit shows high potential in achieving desired performance with lower input RF power when compared to the another configuration based on a generalized Mach–Zehnder interferometer structure. Although the operating range in terms of applied RF drive becomes narrow, low RF input operation can be achieved by this circuit. The effect of imbalances in the key circuit parameters is also investigated in terms of electrical side harmonic suppression ratio.

**Keywords** Optical millimeter-wave generation · Frequency octupling · Polarization modulator · Polarizer

This article is part of the Topical Collection on Numerical Simulation of Optoelectronic Devices, NUSOD' 18.

Guest edited by Paolo Bardella, Weida Hu, Slawomir Sujecki, Stefan Schulz, Silvano Donati, Angela Traenhardt.

✉ Gazi Mahamud Hasan

[1] Photonic Technology Laboratory, Centre for Research in Photonics, University of Ottawa, Ottawa, Canada

[2] School of Opto-electronic Engineering, Changchun University of Science and Technology, Changchun, China

Published online: 19 June 2019

## 1 Introduction

One of the key ingredients of the radio-over-fiber (ROF) paradigm needed to meet the demand of future broadband wireless access is efficient and cost-effective schemes for the generation and transmission of millimeter-wave signals. Conventional electrical millimeter-wave generation schemes are costly and complicated due to the limited frequency response of electronic devices and the involvement of multi-stage frequency multiplication. Optical millimeter-wave signal generation techniques are becoming more attractive. Several techniques are proposed for the generation of optical millimeter-wave, including optical heterodyning using mode-locked lasers (Jung et al. 1999), optical nonlinear effect of stimulated Brillouin scattering (SBS) (Li et al. 2011) and external modulation of a single wavelength laser source. Among them frequency multiplication based on external modulation is proven to have higher spectral purity, simplicity and stability. Frequency doubling (O'Reilly et al. 1992), quadrupling (Lin et al. 2008), sextupling (Hasan et al. 2018), and octupling (Ma et al. 2008; Hasan and Hall 2016) techniques have been demonstrated to achieve millimeter-wave generation capability.

To achieve higher multiplication factors with a high degree of tunability and stability, different schemes incorporating Mach–Zehnder modulator (MZM) (Qin et al. 2014), Sagnac loop (Zhang et al. 2017), polarization modulator (PolM) (Yang et al. 2015), phase modulator (PM) (Hasan et al. 2015) have been proposed. Ma et al. (2008) proposed a frequency octupling system based on a dual-parallel MZM (DP-MZM) with modulation indices of the sub-MZMs to be restricted 2.405 or 5.52 to suppress the optical carrier. Two cascaded MZMs biased at their maximum transmission point with a narrow operating range at certain RF drive level has also been proposed as an optical millimeter-wave signal generation technique in a Radio-over Fiber (RoF) system (Chen et al. 2010). V-band 60-GHz and W-band 80-GHz optical millimeter-wave signal are experimentally generated from 7.5 and 10 GHz driving signals with 30 dB undesired sideband suppression ratios by cascading two DP-MZM (Lin et al. 2009). A Mach–Zehnder interferometer (MZI) structure with arms having two cascaded MZMs biased at points symmetrically deviated from null transmission have been proposed for filterless frequency octupling operation (Shang et al. 2012). Qin et al. (2014) experimentally demonstrated the generation of 80 GHz optical millimeter-wave signal with an optical side harmonic suppression ratio of 34 dB utilizing a cascade of MZM and DP-MZM from 10 GHz RF drive. A frequency octupler with a wide operating range utilizing progressive RF phase shift in a MZI structure having two MZMs on each arms was proposed by Hasan and Hall (2016).

A dual function photonic integrated circuit capable of frequency octupling by exploiting the intrinsic relative phases between the ports of MMI couplers to provide substantially all the static optical phases needed to the phase modulators has also been reported (Hasan et al. 2015). Schemes utilizing eight parallel phase modulator placed between two 4×4 MMI couplers (Hasan et al. 2014), a DPMZM in a Sagnac loop (Gao et al. 2015) or cascaded DPMZM and Sagnac loop (Zhang et al. 2017) have also demonstrated frequency octupling function.

The conventional MZI structure needs the implementation of a suitable integration platform as it is sensitive to the path-length errors between its arms. The schemes using MZMs based on matured $LiNbO_3$ technology suffer from DC bias drift which results in unstable desired sideband power and poor undesired sideband suppression. Hence recently, polarization modulator based optical millimeter wave generation have attracted greater attention of researchers due to its bias-free operation, high extinction

ratio and robustness to path-length error which offer discrete component implementation. Photonic frequency octupling techniques based on two cascaded polarization modulator (Yang et al. 2015) or dual-parallel polarization modulator (Zhu et al. 2016) have been proposed which offer satisfactory performance over a limited operating range with.

In this report, a single arm architecture consisting of 4 polarization modulators (PolM) in series, each followed by a polarizer (Pol) is proposed as an optoelectronic method of microwave frequency octupling. The optical carrier and all sidebands except the odd integer multiples of 4th harmonics are suppressed without the necessity of any optical or electrical filter or careful adjustment of RF drive voltage. The circuit can operate at very low input RF power. Different non-ideal factors are taken into consideration to evaluate the overall performance in terms of electrical side harmonic suppression ratio (ESHSR).

## 2 Operational principle

The single arm cascaded PolM configuration proposed for the frequency octupling is shown in Fig. 1. The circuit consists of four polarization modulators, each followed by a polarizer. A CW linearly polarized laser diode is used as the optical input. The key functional element is the intensity modulator formed by a polarization modulator followed by a polarizer. The alignment of the polarizer angle and the state of the polarization of the input light relative to the principal axis of the respective PolM determine the bias condition of the intensity modulator. In this proposed architecture, each intensity modulator is biased at its minimum transmission point (MITP) and driven differentially with a RF drive signal having a $\pi/4$ progressive phase shift. The optical carrier and all sidebands except those with orders equal to the odd integer multiple of four are naturally suppressed at the output of the circuit.

Consider all the polarization modulators with principal axes aligned with the x and y direction. Suppose the linear polarization state of the input light to a specific $\text{PolM}_n$ is denoted by $\theta_n$. Taking the input polarization state into account, the amplitude transmission function of each polarization modulator followed by a polarizer is given by:

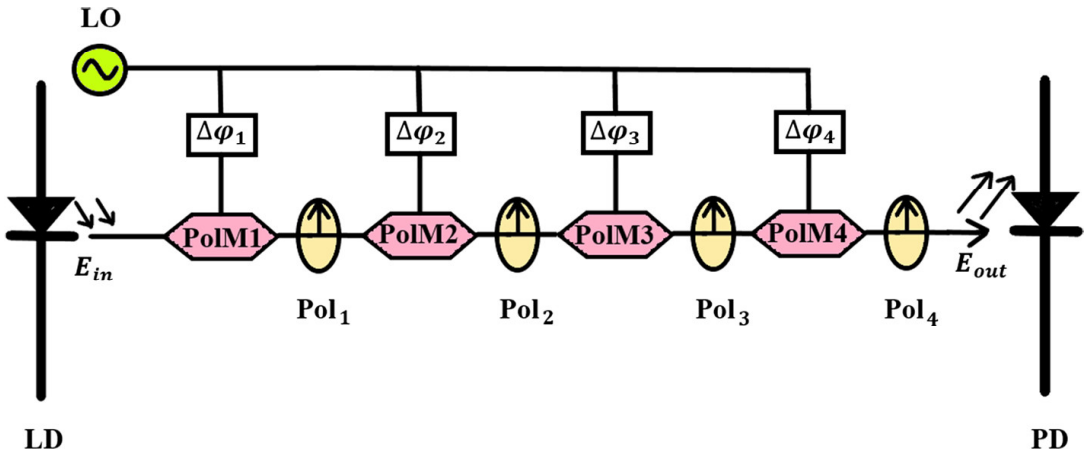


**Fig. 1** Schematic diagram of the proposed frequency octupling architecture. LD: laser diode, PD: photodiode, LO: local oscillator

$$T_n = \left[\cos\left(\Psi_n\right)\ \sin\left(\Psi_n\right)\right]\begin{bmatrix}\exp\left(i\varphi_n\right) & 0\\ 0 & \exp\left(-i\varphi_n\right)\end{bmatrix}\begin{bmatrix}\cos\left(\theta_n\right)\\ \sin\left(\theta_n\right)\end{bmatrix}$$
$$\Rightarrow$$
$$T_n = \cos\left(\Psi_n - \theta_n\right)\cos\left(\varphi_n\right) + \mathrm{i}\cos\left(\Psi_n + \theta_n\right)\sin\left(\varphi_n\right) \tag{1}$$

where $\Psi_n$ is the polarizer angle with respect to the x-axis, $\varphi_n = \left(\pi v_{\mathrm{RF}}/v_\pi\right)\cos\left(\omega_{\mathrm{RF}}\mathrm{t} + \Delta\varphi_n\right)$ is the optical phase shift induced by the RF signal, $v_{\mathrm{RF}}$ is the peak amplitude, $v_\pi$ is the half wave voltage, $\omega_{\mathrm{RF}}$ is the RF angular frequency and $\Delta\varphi_n$ is the phase shift of the nth RF drive introduced to the nth polarization modulator. To bias each intensity modulator at MITP, the polarizer angles are chosen to be $\Psi_{\mathrm{n}} = \pm 45^{\circ}$ while $\theta_n$ is of opposite polarity with same magnitude. The transfer function of each intensity modulator can be expressed as:

$$T_n = i\sin\left[m\cos\left(\omega_{\mathrm{RF}}t + \Delta\varphi_n\right)\right] \tag{2}$$

where $m = \left(\pi\, v_{\mathrm{RF}}/\mathrm{v}_\pi\right)$. Taking $\Delta\varphi_n = n\pi/4 \quad n = 0, 1, 2, 3$, the total transmission function of the proposed architecture is given by:

$$T = \sin\left[m\cos\left(\omega_{\mathrm{RF}}\mathrm{t}\right)\right]\sin\left[m\cos\left(\omega_{\mathrm{RF}}\mathrm{t} + \pi/4\right)\right]$$
$$\cdot\sin\left[m\cos\left(\omega_{\mathrm{RF}}\mathrm{t} + \pi/2\right)\right]\sin\left[m\cos\left(\omega_{\mathrm{RF}}\mathrm{t} + 3\pi/4\right)\right]$$
$$\Rightarrow$$
$$T = \frac{1}{4}\left\{\sum_{n=1}^{\infty}\left[1 + (-1)^n\right]\left[J_{2n}\left(m_1\right) + J_{2n}\left(m_2\right)\right]\cos\left(2n\omega_{RF}t + n\frac{3\pi}{4}\right)\right.$$
$$\left. - \sum_{n=1}^{\infty}\left[1 + (-1)^n\right]\left[J_{2n}\left(m_1\right) + J_{2n}\left(m_2\right)\right]\cos\left(2n\omega_{RF}t + n\frac{\pi}{4}\right)\right\} \tag{3}$$

where the second equation follows from application of the Jacobi-Anger expansion (Abramowitz and Stegun 1964), $J_n$ is the Bessel function of the first kind of order $n$, and:

$$m_1 = \sqrt{2}\left(\sqrt{2 - \sqrt{2}}\right)\pi\, v_{\mathrm{RF}}/v_\pi \tag{4}$$

$$m_2 = \sqrt{2}\left(\sqrt{2 + \sqrt{2}}\right)\pi\, v_{\mathrm{RF}}/v_\pi \tag{5}$$

The strict periodic characteristic of the time-dependent transmission function of individual intensity modulator expressed in (2) determines eight position independent zeros of the total transmission function expressed by (3) at $\omega t\ \epsilon[-\pi, \pi)$ for $|m| < \pi$ (Hasan et al. 2018). This results in the conversion of the co-sinusoidal RF drive signal into a periodic amplitude modulation of the optical carrier with a fourfold submultiple of the period of RF signal. The first few non-zero terms in the expansion in (3) are considered here to express the suppression of the harmonics which are not a multiple of 4:

$$E_{out} = E_{in}\left\{\left[J_4\left(m_1\right) + J_4\left(m_2\right)\right]\sin\left(4\omega_{RF}t\right) - \left[J_{12}\left(m_1\right) + J_{12}\left(m_2\right)\right]\sin\left(12\omega_{RF}t\right)\right.$$
$$\left. + \left[J_{20}\left(m_1\right) + J_{20}\left(m_2\right)\right]\sin\left(20\omega_{RF}t\right)\ldots\right\} \tag{6}$$

It can be seen from (6) that all the sidebands alongside the optical carrier are suppressed by design except the odd multiples of the 4th harmonic. The equation also shows that circuit operation is not restricted to a critical adjustment of RF drive level to suppress the carrier or any unwanted harmonic. Frequency octupling can be achieved by this circuit after passing the optical output onto a photodiode. Selection of $\Psi_n = \theta_n = 45°$ could yield the frequency 16-tupling (Baskaran and Prabakaran 2018) but the operation is restricted to a very narrow range of RF drive level as the carrier suppression cannot be achieved by design. Adjustment of the RF drive level or implementation of an optical filter is needed to suppress the carrier in order to obtain the desired frequency 16-tupling function which makes the operation more complicated.

## 3 Simulation and results

The proposed system is simulated using the Virtual Photonics Inc. (VPI) software package. A continuous wave distributed feedback (DFB) laser at a wavelength of 1550 nm with average power of 10 mW is used as the optical input. Four PolMs with their principal axes aligned with the x and y directions are cascaded. The half wave voltage of each PolM is taken as 1 V. The input light is linearly polarized at 45° which can be controlled by a polarizer controller. To bias the PolM-polarizer intensity modulators at the minimum transmission point (MITP), polarizer angles are selected accordingly (i.e. $-45°$ for $Pol_1$, $Pol_3$ and $+45°$ for $Pol_2$ and $Pol_4$ respectively). A 10 GHz sinusoidal RF drive signal having amplitude of 0.67 V is applied with appropriate RF phase relation (i.e. 0°, 45°, 90° and 135° for $PolM_1$, $PolM_2$, $PolM_3$ and $PolM_4$ respectively). A PIN diode with a responsivity of 0.8 A/W is used for detecting the output signal. No optical or electrical filter is needed to suppress any unwanted harmonics. The simulations are done without employing any optical or electrical amplifier.

Figure 2 shows the optical and electrical spectra at the output of the configuration. As shown in Fig. 2a, the optical carrier and all the sidebands except the odd multiple of 4th order are effectively suppressed. The power of the two 4th order harmonics is 66.9 dB higher than that of the other pronounced unwanted harmonics. After beating at the photodetector, a pristine frequency component at 80 GHz is obtained as shown in Fig. 2b.

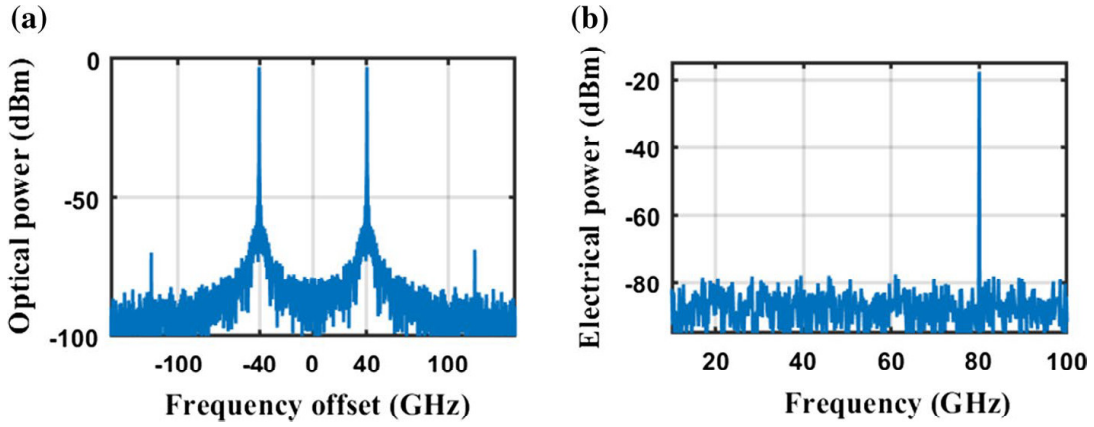


**Fig. 2** **a** Optical spectrum and **b** electrical spectrum of the frequency 8-tupling signal

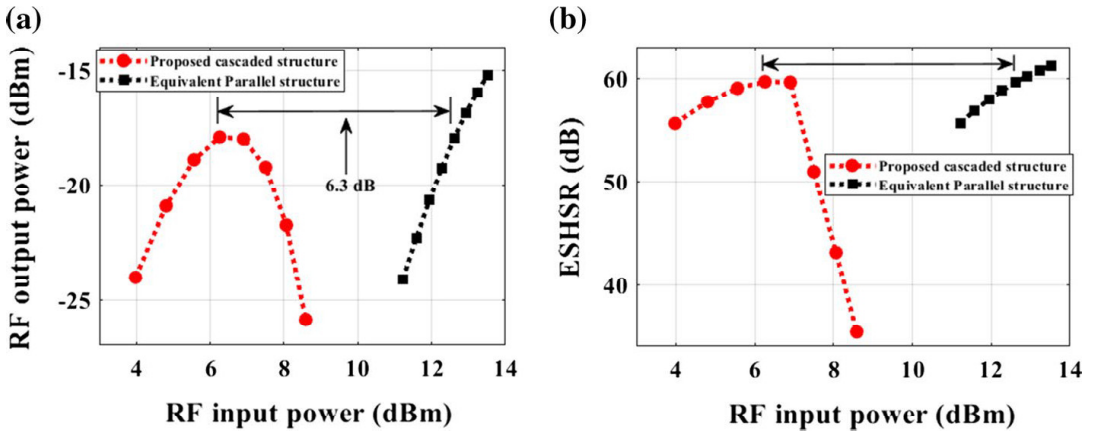


**Fig. 3** Comparison between the proposed cascaded architecture and equivalent parallel architecture in terms of **a** RF input–output power and **b** ESHSR

Figure 3 shows a comparison based on the RF power efficiency of the proposed architecture and another functionally equivalent 8-tupling architecture consisting of 4 parallel MZMs. The parallel structure is based on the generalized Mach–Zehnder interferometer (MZI) architecture where the MZMs are biased at their maximum transmission point (MATP) (Maldonado-Basilio et al. 2015). To suppress the carrier by design, the MZMs are connected to achieve the functionality of a dual parallel DP-MZMs biased at MATP. The outer MZI is biased at the minimum transmission point. The setups have similar parameters with the same half-wave voltage for each modulator. The x axis of the plot shows the applied RF input power to each modulator in dBm, while the y axis depicts the generated RF power for a load resistance of 50 Ω. To observe the unwanted higher order electrical harmonics, the RF frequency is taken as 5 GHz. The comparison of the two structures in terms of input–output RF power and ESHSR are shown in Fig. 3a, b respectively. It can be observed that for the same output power and ESHSR, the proposed circuit needs ~6 dB less in input RF power to each modulator than the parallel architecture. The operating range of the proposed architecture becomes small compared to the other but it can be used for a range of input RF power as low as 4 dBm to achieve output power greater than −23 dBm with ESHSR > 55 dB. The MZMs in the parallel circuit can be replaced by polarization modulator followed by polarizer which yields same performance. This choice can avoid the problems related to DC bias drift and unbalanced splitting ratio intrinsic to the MZM. The optical biasing of the parallel architecture needs the employment of an optical delay line, Y-splitter and combiner. The same bias arrangement can be achieved by directional couplers or polarization beam combiner followed by polarizer also. These biasing schemes will introduce additional excess optical loss relative to the proposed cascaded architecture.

Drifts from the ideal condition are also investigated. Figure 4 shows the variation of ESHSR due to the deviation in polarization angle from their ideal condition. It can be observed from Fig. 4 that the first polarizer in the cascaded structure has the most pronounced effect on the performance, but still operation with ESHSR greater than 40 dB can be achieved with ±2° drift in any polarizer angle.

ESHSR calculated for a constant RF peak amplitude at 0.67 V while varying individual RF drive phases are plotted in Fig. 5. It can be observed that the ESHSR dependence on RF drive phase is more severe. The error in the phase of the drive to each stage displaces

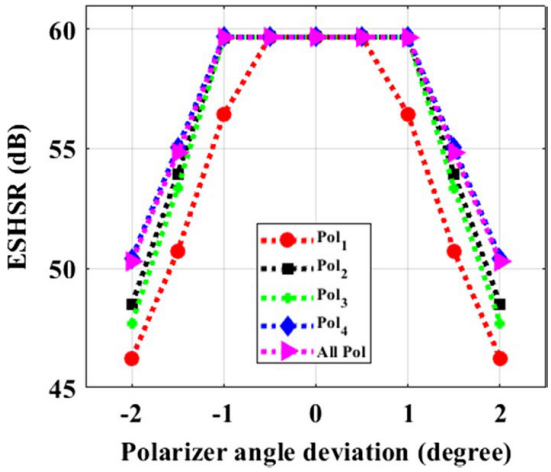


**Fig. 4** ESHSR variation due to the drift of polarizer angle

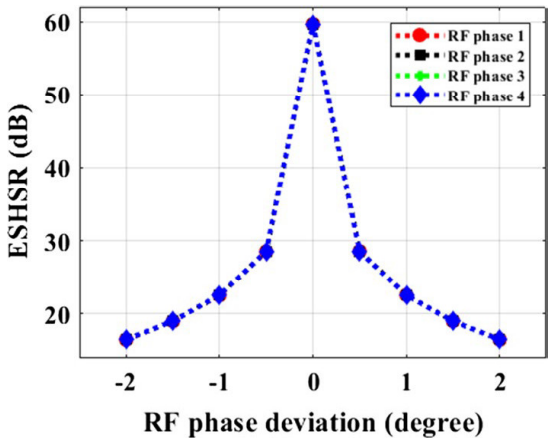


**Fig. 5** ESHSR variation due to the drift of RF drive phase

the zeros from their ideal position which breaks the sub-periodicity of the transmission function of (3) and thereby results in a loss of complete suppression of the unwanted harmonics. Figure 5 shows an almost identical performance degradation for individual RF drive phase deviation. Careful RF phase maintenance can limit the phase drift into $\pm 1^\circ$ to achieve ESHSR greater than 20 dB. Different mechanisms can be exploited to achieve RF phase stability. Porzi et al. (2018) proposed and experimentally demonstrated a stable photonic-integrated microwave phase shifter with a range of more than 360° phase shift over broad bandwidth of more than 6 GHz around an RF carrier flexibly selectable between 10 and 16 GHz. Another filterless $1 \times N$ hybrid RF photonic splitter capable of producing arbitrary phase shift and amplitude ratio is reported in reference (Zhu et al. 2019).

The proposed circuit is robust to the amplitude errors provided they are not so great that additional zeros are introduced into the waveform. The effects of the RF drive amplitude deviation is shown in Fig. 6. In Fig. 6a, the RF drive employed to $\text{PolM}_2$ is subjected to the peak amplitude variation while others are kept at 0.67 V. Figure 2b is a more practical case where all the RF drives are having different peak amplitude. The ESHSR is observed for this case is 19 dB. The phase shifter proposed by Porzi et al. (2018) has been demonstrated that the power oscillation is well confined within 0.8 dB over the 360° phase shift range. Spectral impurity due to RF drive amplitude variation can be minimized by the application of variable attenuator (Urick et al. 2016).

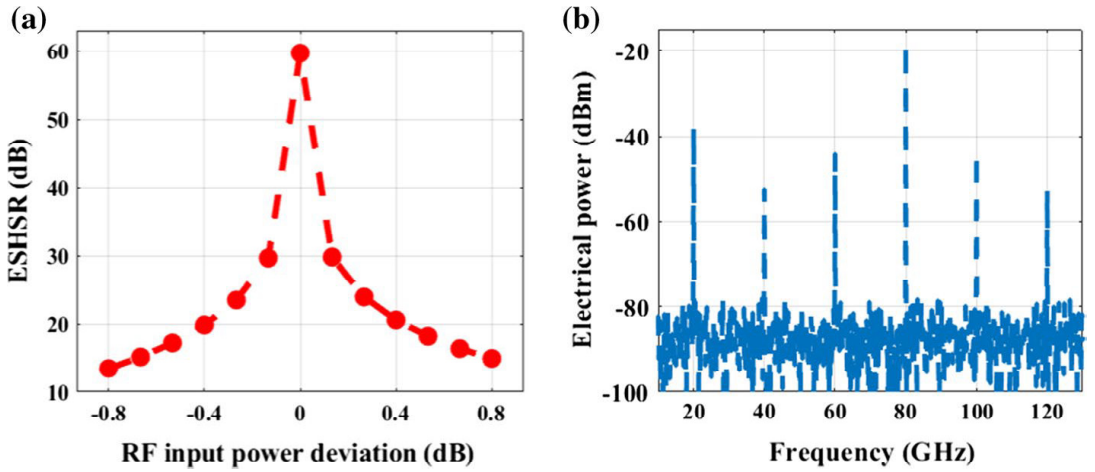


**Fig. 6** The effect of RF drive amplitude deviation **a** the amplitude of RF drive employed to $PolM_2$ is varied, while others are kept at constant value, **b** electrical spectrum of the proposed circuit when different RF drives are having different amplitude

## 4 Conclusion

In summary, a photonic circuit architecture consisting of four intensity modulator in cascade is proposed as a RF energy efficient method to perform frequency octupling. The combination of polarizer and polarization modulator with specific RF drive phases is an alternative to a conventional MZM which is prone to DC bias shift. The circuit can operate at lower RF drive level with ~6 dB RF advantage compared to functionally equivalent circuit. Moreover, the circuit requires no DC bias, optical filtering or careful adjustment of RF drive level for carrier and unwanted sideband suppression. Effects of imbalances of the various circuit parameters have also been investigated. The results show it is robust to component error.

**Acknowledgements** Mehedi Hasan acknowledges the Natural Sciences and Engineering Research Council of Canada (NSERC) for their support through the Vanier Canada Graduate Scholarship program. Karin Hinzer is grateful to D & T Photonics and MITACS for their support through the MITACS accelerate award number IT07662. Trevor Hall is grateful to the University of Ottawa for their support of his University Research Chair.

**Availability of data and material** The datasets used and analyzed during the current study are available from the corresponding author on reasonable request.

## Compliance with ethical standards

**Conflict of interest** The authors declare that they have no conflict of interest.

## References

Abramowitz, M., Stegun, I.A.: Handbook of Mathematical Functions: With Formulas, Graphs, and Mathematical Tables. United States Department of Commerce, National Bureau of Standards, Washington D.C. (1964)

Baskaran, M., Prabakaran, R.: Optical millimeter wave signal generation with frequency 16-tupling using cascaded MZMs and no optical filtering for radio over fiber system. J. Eur. Opt. Soc. Rapid Publ. (2018). https://doi.org/10.1186/s41476-018-0080-1

Chen, Y., Aijun Wen, A., Shang, L.: Analysis of an optical mm-wave generation scheme with frequency octupling using two cascaded Mach–Zehnder modulators. Opt. Commun. **283**, 4933–4941 (2010)

Gao, Y., Wen, A., Li, N., Wu, X., Zhang, H.: Microwave generation with photonic frequency octupling using a DPMZM in a Sagnac loop. J. Mod. Opt. **62**, 1291–1296 (2015)

Hasan, M., Hall, T.J.: A photonic frequency octo-tupler with reduced RF drive power and extended spurious sideband suppression. Opt. Laser Technol. **81**, 115–121 (2016)

Hasan, M., Guemri, R., Maldonado-basilio, R., Lucarz, F., Tocnaye, J.-L.B., Hall, T.J.: Theoretical analysis and modeling of a photonic integrated circuit for frequency 8-tupled and 24-tupled millimeter wave signal generation. Opt. Lett. **39**, 6950–6953 (2014)

Hasan, M., Maldonado-Basilio, R., Hall, T.J.: Dual-function photonic integrated circuit for frequency octo-tupling or single-side-band modulation. Opt. Lett. **40**, 2501–2504 (2015)

Hasan, M., Hinzer, K., Hall, T.J.: Cascade circuit architecture for RF-photonic frequency multiplication with minimum RF energy. J. Mod. Opt. (2018). https://doi.org/10.1080/09500340.2018.1519607

Jung, T., Shen, J.-L., Tong, D.T.K., Murthy, S., Wu, M.C., Tanbun-Ek, T., Wang, W., Lodenkamper, R., Davis, R., Lembo, L.J., Brock, J.C.: CW injection locking of a mode-locked semiconductor laser as a local oscillator comb for channelizing broad-band RF signals. IEEE Trans. Microw. Theory Tech. **47**, 1225–1232 (1999)

Li, W., Zhu, N.H., Wang, L.X.: Harmonic RF carrier generation and broadband data up-conversion using stimulated Brillouin scattering. Opt. Commun. **284**, 3437–3439 (2011)

Lin, C.-T., Shih, P.-T., Chen, J., Xue, W.-Q., Peng, P.-C., Chi, S.: Optical millimeter-wave signal generation using frequency quadrupling technique and no optical filtering. IEEE Photonics Technol. Lett. **20**, 1027–1029 (2008)

Lin, C.-T., Shih, P.-T., Jiang, W., Chen, J.J., Peng, P., Chi, S.: A continuously tunable and filterless optical millimeter-wave generation via frequency octupling. Opt. Express **17**, 19749–19756 (2009)

Ma, J., Xin, X., Yu, J., Yu, C., Wang, K., Huang, H., Rao, L.: Optical millimeter wave generated by octupling the frequency of the local oscillator. J. Opt. Netw. **7**, 837–845 (2008)

Maldonado-basilio, R., Hasan, M., Guemri, R., Lucarz, F., Hall, T.J.: Generalized Mach–Zehnder interferometer architectures for radio frequency translation and multiplication: suppression of unwanted harmonics by design. Opt. Commun. **354**, 22–127 (2015)

O'Reilly, J.J., Lane, P.M., Heidemann, R., Hofstetter, R.: Optical generation of very narrow linewidth millimeter wave signals. Electron. Lett. **28**, 2309–2311 (1992)

Porzi, C., Serafino, G., Sans, M., Falconi, F., Sorianello, V., Pinna, S., Mitchell, J.E., Romagnoli, M., Bogoni, A., Ghelfi, P.: Photonic integrated microwave phase shifter up to the mm-wave band with fast response time in silicon-on-insulator technology. J. Lightw. Technol. **36**, 4494–4500 (2018)

Qin, Y., Sun, J., Du, M., Liao, J.: Simplified optical millimeter-wave generation configuration based on frequency octupling. Opt. Commun. **315**, 280–285 (2014)

Shang, L., Wen, A., Li, B., Wang, T., Chen, Y., Li, M.: A filterless optical millimeter-wave generation based on frequency octupling. Optik **123**, 1183–1186 (2012)

Urick, V.J., Mondich, M.J., Sunderman, C.E., Kozak, D.A., Goetz, P.G., Rabinovich, W.S., Pruessner, M.W., Mahon, R., Williams, K.J.: Microwave phase shifting using coherent photonic integrated circuits. IEEE J. Sel. Top. Quantum Electron. **22**, 353–360 (2016)

Yang, Y., Ma, J., Zhang, R., Zhang, J.: Generation of optical millimeter wave using two cascaded polarization modulators based on frequency octupling without filtering. Fiber Integr. Opt. **34**, 230–242 (2015)

Zhang, W., Wen, A., Gao, Y., Shang, S., Zheng, H., He, H.: Filterless frequency-octupling mm-wave generation by cascading Sagnac loop and DPMZM. Opt. Laser Technol. **97**, 229–233 (2017)

Zhu, Z., Zhao, S., Li, X., Huang, A., Qu, K., Lin, T.: Photonic generation of frequency-octupled and frequency-quadrupled microwave signals using a dual-parallel polarization modulator. Opt. Quantum Electron. (2016). https://doi.org/10.1007/s11082-016-0671-2

Zhu, S., Li, M., Wang, X., Zhu, N.H., Li, W.: 1 × N hybrid radio frequency photonic splitter based on a dual-polarization dual-parallel Mach Zehnder modulator. Opt. Commun. **431**, 10–13 (2019)

## 3.6 Summary

In summary, two photonic circuit architecture are proposed that have the ability of millimeter-wave generation using the optical external modulation technique. Both circuits employ polarization modulators instead of conventional Mach-Zehnder modulator or phase modulator. The cascade of polarization modulator and polarizer provides the operation of an intensity modulator whose biasing condition can be set by the polarizer angle and polarization state of the input light to each polarization modulator. A frequency multiplication factor of eight is achieved by both circuits which eases the requirement of the RF local oscillator to access the millimeter-wave band. Complete suppression of carrier and unwanted sidebands except harmonics of order equal to odd integer multiples of four is achieved by design which nullifies the adoption of optical and electrical filters and simplifies the circuits' operation and configuration. The operation of the frequency multiplication circuits is not restricted by any requirement to set the amplitude of the drive signal to a precise level which has the associated advantage of wide operating range in terms of modulation index with excellent spectral purity. The adoption of a polarization modulator instead of a MZM facilitates the DC bias free operation. Besides, the conventional MZI suffers from the path-length errors between its two arms whereas, in a polarization modulator, spatial overlap between the two-modes and propagation through identical physical path offers robust operation against relative optical path-length difference. This facilitates demonstration of the operation of both of the proposed circuits with discrete components. Moreover, developments in polarization modulators integrated on material platforms such as GaAs/AlGaAs [118], InP/InGaAsP [120] and progress on photonic integration technology [121] provide prospects of photonic integrated circuit implementation. The predictions of the theoretical analysis have been verified by computer simulations. Both circuits achieve unwanted optical harmonic suppression of more than 65 dB when ideal conditions are considered. A 10 GHz RF input signal can be translated to 80 GHz with electrical side harmonic suppression ratio (ESHSR) of >60 dB after beating the optical signal at a photodetector. The proposed system analysed in the first part of the chapter can provide operation over a modulation index from 1.9 to 7.3. The second architecture can operate at lower RF drive level with ~6 dB RF advantage compared to functionally equivalent parallel circuit. Non-ideal situations are also acknowledged for both circuits and it can be observed that the performance is limited mostly due to the errors in RF conditions. Operation with ESHSR greater than 20 dB can be obtained with practical values of component errors.

# Chapter 4. Performance Analysis of a Multi-function Photonic Architecture on SOI employed as a Frequency Shifter

## 4.1 Introduction

The ever-growing data traffic and super broadband services demanded by the end users have led the wireless communication network to undergo rapid development in terms of capacity, bandwidth, cost and mobility. The low-power, mature lower frequency bands are already congested and offer small capacity in wireless communication. On the other hand, the high capacity high frequency wireless system is inherently power hungry, costly and imposes complicated coverage schemes. This bottleneck has introduced the radio-over-fiber (RoF) system as a viable solution for broadband wireless access networks [122-123]. RoF technology can exploit the low loss, lower power consumption and broad bandwidth offered by optical fiber communication by distributing the radio signals over the optical fiber. Traditionally, RoF employs analogue intensity-modulated direct detection (IM-DD) optical links [124-125] which is prone to high power consumption, limited dynamic range and periodic RF power fading. Hall et al. reasoned that broadband wireless access network using distributed antenna system architecture deployed in cluttered urban environments complemented by a digital coherent optical RoF link provides an energy efficient solution [3]. The millimeter-wave (mm-wave) carrier generation at downlink and efficient single sideband (SSB) modulation at uplink are two major factors to be considered for improvement of digital coherent optical transport of RF signal [23-25]. Numerous researches have been undertaken on photonic mm-wave generation techniques. The simplest approach is the heterodyne beating of two phase correlated optical carriers separated in frequency at a high speed photo-detector. The conventional methods are based on a dual-mode laser [126], a dual lasers with phase locking [127-128] or mode-lock lasers [129] which all suffer low RF coherency or limited tunability. External modulation based photonic mm-wave generation techniques are emerging as a feasible candidate due to its higher spectral purity, simplicity, stability and low RF frequency requirement [34],[59],[115]. A common feature of most external modulation based architectures is that the pair of high-order harmonics separated by the desired RF carrier frequency is emitted from the same output port. Hence, optical frequency selective components such as arrayed wavelength grating (AWG), frequency de-multiplexer are needed to separate these sub-carriers in order that they may be modulated individually. This introduces complexity in system implementation in terms of tuning, selectivity and temperature sensitivity [130-131].

Yamazaki et al. demonstrated that a complementary frequency shifter capable of spatial frequency separation can be implemented and integrated along with an in-phase quadrature-phase (IQ) modulator to obtain separate subcarrier modulation without using any optical frequency de-multiplexer and achieved data rates up to 400 Gbit/s using dual-polarization (DP) 16-level QAM [132-133]. A digital coherent RoF system with downlink utilizing a higher order SSB modulator as a frequency shifter to generate mm-wave has been proposed by Hassan & Hall [134]. Their architecture exploits the spatial separation of higher order sideband for frequency multiplication and consequently can be operated in a low RF frequency regime.

A multi-functional photonic circuit consisting of four differentially driven MZMs in parallel has been proposed in [135]. Sub-carrier generation, frequency multiplication, complex modulation and frequency conversion can be achieved by the same architecture. Each functionality is associated with a combination of MZM biasing, optical phase shifting and RF relative phase relationship which can be obtained by outside control. Table 4.1 describes the conditions for achieving these function. Figure 4.2 shows the schematic of the proposed circuit. In this chapter, the frequency shifting capability of the proposed architecture [135] is demonstrated. The silicon-on-insulator (SOI) platform has been used for the fabrication of the circuit. Multimode interference (MMI) couplers are used as the splitter/combiner of the MZI structures to avoid DC bias drift problem. Besides, MMI offers wideband operation, less sensitivity to slight fabrication defects and low loss. The circuit had been fabricated to prove its implementation feasibility and so, to avoid complexity, tuning mechanism had been avoided in the design. The observations obtained from our experiments is encouraging for future fabrication with proper tuning mechanism and implementation in the digital coherent RoF link of a viable sub-carrier generator with higher order frequency multiplication at downlink and SSB modulator at uplink.

Table 4.1: List of parameters necessary to obtain target application (MATP: Maximum transmission point; MITP: Minimum transmission point; Complex signal $= V_I + iV_Q$ )

| | | Sub-carrier generation | Frequency conversion/SSB modulation | IQ modulation | Frequency 8-tupling |
|---|---|---|---|---|---|
| MZM DC bias point | $MZM_A$ | MITP | MITP | MITP | MATP |
| | $MZM_B$ | MITP | MITP | MITP | MATP |
| | $MZM_C$ | MITP | MITP | MITP | MATP |
| | $MZM_D$ | MITP | MITP | MITP | MATP |
| Optical phase shift | $MZM_A$ | $\pi/4$ | 0 | 0 | 0 |
| | $MZM_B$ | 0 | 0 | 0 | 0 |
| | $MZM_C$ | $2\pi/4$ | 0 | 0 | 0 |
| | $MZM_D$ | $3\pi/4$ | 0 | 0 | 0 |
| Modulating signal | $MZM_A$ | $V_{RF}\sin(\omega_{RF}t)$ | $V_{RF}\sin(\omega_{RF}t)$ | $V_I$ | $V_{RF}\cos(\omega_{RF}t)$ |
| | $MZM_B$ | $V_{RF}\sin(\omega_{RF}t+\pi/4)$ | $V_{RF}\sin(\omega_{RF}t+\pi/2)$ | $V_Q$ | $V_{RF}\cos(\omega_{RF}t+\pi/4)$ |
| | $MZM_C$ | $V_{RF}\sin(\omega_{RF}t+3\pi/4)$ | $V_{RF}\sin(\omega_{RF}t+\pi/2)$ | $V_Q$ | $V_{RF}\cos(\omega_{RF}t+\pi/2)$ |
| | $MZM_D$ | $V_{RF}\sin(\omega_{RF}t+2\pi/4)$ | $V_{RF}\sin(\omega_{RF}t)$ | $V_I$ | $V_{RF}\cos(\omega_{RF}t+3\pi/4)$ |

## 4.2 Contribution

The results described in this chapter are being prepared for publication. A primary draft has been archived in arXiv.org. This chapter provides a theoretical verification of the frequency shifting functionality of the fabricated circuit. A short review on silicon modulator is presented. The results collected from experiments are delivered and explained. Circuit and design modifications needed for better performance are prescribed for future fabrication. I prepared the set up for testing and measurement, conducted the experiment and collect data, characterized the results and prescribe future fabrication modifications needed. Mehedi Hasan helped me in conducting experiment and described the functionalities in a publication [135]. Dr. Jessica Zhang from CMC microsystem prepared the layout. Dr. Ramón Maldonado-Basilio did the wirebonding of the chip and conducted an experiment before to evaluate the diode characteristics of the individual phase modulator [137].

Dr. Trevor Hall developed the theory, designed the circuit, provided advice on the interpretation of the results and helped revise the manuscript.

## 4.3 Theory

The conventional waveguide-based method for frequency shifting utilizing single sideband modulation (SSB) by an in-phase/quadrature (IQ) modulator was first described by Izutsu et al. [81]. Their architecture consists of a dual parallel Mach-Zehnder modulator (DPMZM) which has two differential MZMs, each on one arm of an outer Mach-Zehnder interferometer (MZI) structure. The MZMs are set to their minimum transmission bias points and act as amplitude modulators.

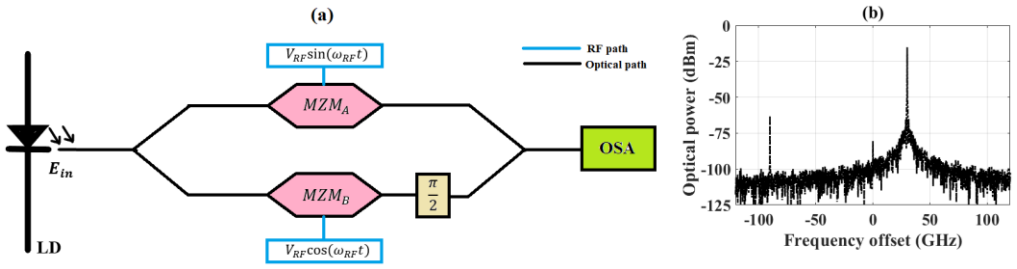


Figure 4.1 (a) Schematic diagram of conventional IQ modulator based optical frequency shifter. The MZMs are differentially driven. π/2 optical phase shift is applied to bias the outer MZI to its quadrature point (b) Optical spectrum of the corresponding circuit showing frequency shifting of the carrier by the RF frequency 30 GHz. Simulation is done using Virtual photonics Inc. (VPI) software package. MZM: Mach-Zehnder modulator, OSA: Optical spectrum analyzer, LD: Laser diode

The outer MZI is set to its quadrature bias point i.e. one arm has a phase shift of π/2 with respect to the other. Figure 4.1 shows the architecture and the output optical spectrum of this IQ modulator.

The circuit shown in Figure 4.1(a) can perform the SSB frequency electro-optical up-conversion function if an RF electrical signal is applied to I channel and a π/2 phase-shifted replica of the same RF electrical signal is applied to the Q channel. In the ideal situation, each of the Y-splitters has a perfect 3-dB splitting ratio which leads to the transmission function of the circuit to be:

$$\begin{aligned} f_1(t) &= \frac{i}{2}\{\sin[m\cos(\omega_{RF}t)] + i\sin[m\sin(\omega_{RF}t)]\} \\ &\Longrightarrow \\ f_1(t) &= i\{J_1(m)\exp[j\omega_{RF}t] - J_3(m)\exp[-j3\omega_{RF}t] \ldots\} \end{aligned} \tag{4.1}$$

where $m = \pi V_{\mathrm{RF}}/v_\pi$ is the modulation index, $v_\pi$ is the half-wave voltage of the modulator, $J_p$ is the Bessel function of the first kind of order $p$ and $\omega_{RF}$ is the RF angular frequency. The optical spectrum shown in Figure 4.1(b) is achieved for $V_{\mathrm{RF}} = 0.1v_\pi$. Restricting operation in small signal modulation range results in lower conversion efficiency but high side-harmonic suppression [90]. A polarity change at the phase in the outer MZI can switch the upper sideband (USB) to lower sideband (LSB) operation.

Maldonado-Basilio et al. proposed an electro-optical up-conversion mixer which utilizes the intrinsic relative phase relationships between the ports of MMI coupler to provide necessary static

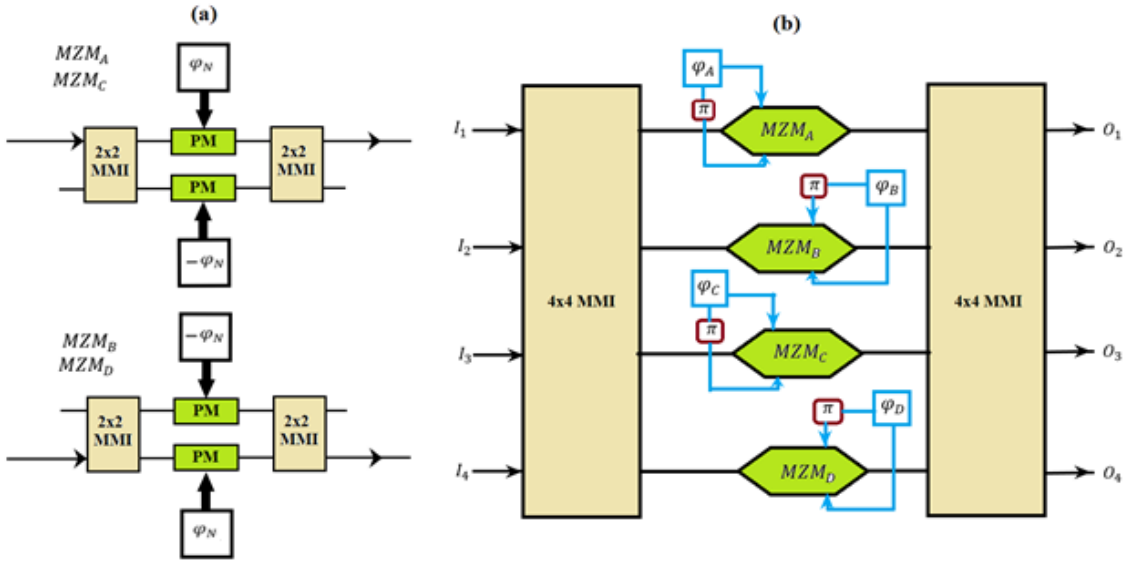


Figure 4.2 (a) Schematic of the differentially driven MZMs; (b) Schematic diagram of the proposed frequency shifter circuit. Each MZM is driven differentially with modulating signals $\varphi_A, \varphi_B, \varphi_C$ and $\varphi_D$ respectively. MMI: Multimode interference coupler, PM: Phase modulator, MZM: Mach-Zehnder modulator

phase, eliminating the need of static bias, static phase element and trimming [136]. Another photonic frequency multiplier circuit uses the same concept of exploiting the phase relationship of input and output signals in the MMI coupler to obtain an 8-fold multiplication of the electric local oscillator frequency [58],[137]. Mehedi Hassan et al. extended the circuits functionality to have dual-carrier complex modulation, sub-carrier generation and frequency up-conversion [135]. This photonic circuit consists of eight phase modulator situated in the arms between an interconnected 4×8 distribution tree and a complementary 8×4 combination tree. The 4×8 distribution tree starts with an outer stage of 4×4 MMI coupler which is followed by an inner stage consisting of two parallel pairs of 2×2 MMI couplers. The 8×4 combination tree maintains a reciprocal structure of the distribution tree. Four MZI structures can be formed by connecting each pair of phase modulators to the inner stage MMIs as shown in Figure 4.2(a). Each MZI configuration can act as an MZM when differentially driven. A little modification in the connections between the outer and inner stages at the distribution and combination sides which would translate into the bias point reversal converts the frequency 8-tupling circuit in [58] to the IQ modulator in [135]. The schematic diagram of the modified IQ modulator is shown in Figure 4.2(b).

To achieve the IQ modulator operation, each MZM is to be biased at its minimum transmission point (MITP). This can be maintained by selecting appropriate input and output ports of each MZI which offers the necessary static optical phase difference between the arms of MZM due to the intrinsic relative phase relationships between the ports of MMI coupler. Figure 4.2(a) shows the choice of input-output ports for which MITP condition for each MZM can be achieved by design. The transfer matrix of individual MZM can be expressed as:

$$\begin{bmatrix} b_1 \\ b_2 \end{bmatrix} = T_{2\times2} \begin{bmatrix} \exp(i\varphi_1) & 0 \\ 0 & \exp(i\varphi_2) \end{bmatrix} T_{2\times2} \begin{bmatrix} a_1 \\ a_2 \end{bmatrix} \tag{4.2}$$

where $T_{2\times2} = \frac{1}{\sqrt{2}}\begin{bmatrix} 1 & -i \\ -i & 1 \end{bmatrix}$ is the transfer matrix of a 2×2 MMI coupler and $\varphi_n$ is the phase shift applied to the n$^{th}$ arm of an MZM. Based on the input/ output ports of each MZM chosen and the phase shift applied to drive each MZM differentially, the transmission function of each MZM can be obtained as:

$$f_{MZM_N} = i\sin(\varphi_N) \tag{4.3}$$

The four parallel MZMs biased at MITP provide the framework of two parallel IQ modulators. The necessary optical phase difference between two MZMs of each IQ modulator can be obtained by a proper interconnection between the inner MZM stage and the 4×4 MMI couplers at the outer stages. The detailed schematic diagram in Figure 4.2(b) shows a mirror symmetry in terms of circuit connection. Several ways for the application of RF inputs satisfying the condition of biasing the outer MZI of each IQ modulator at its quadrature point are possible. Figure 4.2(b) shows one example which retains the mirror symmetry. In this architecture, the upper two MZMs form one IQ modulator and the lower two MZMs form the other one.

The total transfer matrix of the architecture can be expressed as [58]:

$$\begin{bmatrix} O_1 \\ O_2 \\ O_3 \\ O_4 \end{bmatrix} = i\,T_{4\times4}\begin{bmatrix} \sin(\varphi_A) & 0 & 0 & 0 \\ 0 & \sin(\varphi_B) & 0 & 0 \\ 0 & 0 & \sin(\varphi_C) & 0 \\ 0 & 0 & 0 & \sin(\varphi_D) \end{bmatrix} T_{4\times4}\begin{bmatrix} I_1 \\ I_2 \\ I_3 \\ I_4 \end{bmatrix} \tag{4.4}$$

where $T_{4\times4} = \frac{1}{\sqrt{4}}\begin{bmatrix} 1 & -\zeta & \zeta & 1 \\ -\zeta & 1 & 1 & \zeta \\ \zeta & 1 & 1 & -\zeta \\ 1 & \zeta & -\zeta & 1 \end{bmatrix}$ is the transfer matrix of a 4×4 MMI coupler. Here, $\zeta = e^{i\pi/4}$.

Assuming only $I_1$ to be connected to the optical source and two modulating signals $V_1 = V_{I1} + iV_{Q1}$ and $V_2 = V_{I2} + iV_{Q2}$ to be applied in such a way that $\varphi_A = \pi V_{I1}/v_\pi$ , $\varphi_B = \pi V_{Q1}/v_\pi$, $\varphi_C = \pi V_{Q2}/v_\pi$ and $\varphi_D = \pi V_{I2}/v_\pi$, the outputs of the architecture can be expressed as:

$$\begin{bmatrix} O_1 \\ O_2 \\ O_3 \\ O_4 \end{bmatrix} = \frac{i}{4}\begin{bmatrix} \sin(\pi V_{I1}/v_\pi) + i\sin(\pi V_{Q1}/v_\pi) + \sin(\pi V_{I2}/v_\pi) + i\sin(\pi V_{Q2}/v_\pi) \\ \zeta\{-\sin(\pi V_{I1}/v_\pi) - \sin(\pi V_{Q1}/v_\pi) + \sin(\pi V_{I2}/v_\pi) + \sin(\pi V_{Q2}/v_\pi)\} \\ \zeta\{\sin(\pi V_{I1}/v_\pi) - \sin(\pi V_{Q1}/v_\pi) - \sin(\pi V_{I2}/v_\pi) + \sin(\pi V_{Q2}/v_\pi)\} \\ \sin(\pi V_{I1}/v_\pi) - i\sin(\pi V_{Q1}/v_\pi) + \sin(\pi V_{I2}/v_\pi) - i\sin(\pi V_{Q2}/v_\pi) \end{bmatrix}[I_1] \tag{4.5}$$

For $(V_{I1}/v_\pi, V_{Q1}/v_\pi, V_{I2}/v_\pi, V_{Q2}/v_\pi) \ll 1$, equation (4.5) can be written as:

$$\begin{bmatrix} O_1 \\ O_2 \\ O_3 \\ O_4 \end{bmatrix} = \frac{i\pi}{4v_\pi}\begin{bmatrix} V_1 + V_2 \\ \zeta\{(V_{I2} - V_{I1}) + (V_{Q2} - V_{Q1})\} \\ \zeta\{(V_{I1} - V_{I2}) + (V_{Q2} - V_{Q1})\} \\ {V_1}^* + {V_2}^* \end{bmatrix}[I_1] \tag{4.6}$$

where (*) stands for complex conjugate. In the case of a pure tone modulating signal, i.e. $\varphi_A = \varphi_D = m\cos(\omega_{RF}t)$ and its companion π/2 phase shifted replica, i.e. $\varphi_B = \varphi_C = m\cos(\omega_{RF}t + \pi/2)$, the outputs of the architecture can be expressed as:

$$\begin{bmatrix} O_1 \\ O_2 \\ O_3 \\ O_4 \end{bmatrix} = \begin{bmatrix} -i\sum_{n=1}^{\infty} J_{2n-1}(m)\{(-1)^n \cos[(2n-1)\omega_{RF}t] + i\sin[(2n-1)\omega_{RF}t]\} \\ 0 \\ 0 \\ -i\sum_{n=1}^{\infty} J_{2n-1}(m)\{(-1)^n \cos[(2n-1)\omega_{RF}t] - i\sin[(2n-1)\omega_{RF}t]\} \end{bmatrix} [I_1]$$

$$\Longrightarrow$$

$$\begin{bmatrix} O_1 \\ O_2 \\ O_3 \\ O_4 \end{bmatrix} = \begin{bmatrix} i\{J_1(m)\exp[-j\omega_{RF}t] - J_3(m)\exp[j3\omega_{RF}t] \dots\} \\ 0 \\ 0 \\ i\{J_1(m)\exp[j\omega_{RF}t] - J_3(m)\exp[-j3\omega_{RF}t] \dots\} \end{bmatrix} [I_1] \tag{4.7}$$

It can be observed from equation (4.7) that for this specific input/output combination and local oscillator setting, this photonic architecture performs an electrical to optical frequency up-conversion with the lower optical sideband available from output port $O_1$ and the upper optical sideband available from output port $O_4$. In principle, all even order harmonics, including the carrier are suppressed. Among the odd order harmonics, for output port $O_1$, positive orders equal to (2p+1), with p even, and negative orders equal to –(2p+1) , with p odd, are suppressed and vice versa for output port $O_4$. By energizing other input ports individually, the LSB-USB operations shift to other output ports. Interchanging the local oscillator setting, i.e. $\varphi_A = \varphi_D = m\cos(\omega_{RF}t + \pi/2)$ and $\varphi_B = \varphi_C = m\cos(\omega_{RF}t)$ leads the LSB-USB operation to swap their respective output ports, maintaining their distinct spatial separation. Table 4.2 lists all the input-output combination that leads the electrical to optical frequency up-conversion for the RF setting shown in Figure 4.2(b).

It is possible to remove one IQ modulator completely from the operation by disconnecting the RF local oscillators to it. For equal phase shift at both arms of an MZI architecture, it will act as a cross-over if there is no external perturbation in phase. From Figure 4.2, it can be observed that all the cross-ports are unused which means that any MZI can be cut-off completely at the expense of optical power. Taking $\varphi_C = \varphi_D = 0$ leads the removal of the lower IQ modulator to be from the end-to-end optical path which modifies equation (4.4) to:

$$\begin{bmatrix} O_1 \\ O_2 \\ O_3 \\ O_4 \end{bmatrix} = i\,T_{4\times4} \begin{bmatrix} \sin(\varphi_A) & 0 & 0 & 0 \\ 0 & \sin(\varphi_B) & 0 & 0 \\ 0 & 0 & \sin(\varphi_C) & 0 \\ 0 & 0 & 0 & \sin(\varphi_D) \end{bmatrix} T_{4\times4}[I_1]$$

$$\Longrightarrow$$

$$\begin{bmatrix} O_1 \\ O_2 \\ O_3 \\ O_4 \end{bmatrix} = \frac{1}{2} \begin{bmatrix} -i\sum_{n=1}^{\infty} J_{2n-1}(m)\{(-1)^n \cos[(2n-1)\omega_{RF}t] + i\sin[(2n-1)\omega_{RF}t]\} \\ e^{i3\pi/4}\sum_{n=1}^{\infty} J_{2n-1}(m)\{(-1)^n \cos[(2n-1)\omega_{RF}t] + \sin[(2n-1)\omega_{RF}t]\} \\ -e^{i3\pi/4}\sum_{n=1}^{\infty} J_{2n-1}(m)\{(-1)^n \cos[(2n-1)\omega_{RF}t] - \sin[(2n-1)\omega_{RF}t]\} \\ -i\sum_{n=1}^{\infty} J_{2n-1}(m)\{(-1)^n \cos[(2n-1)\omega_{RF}t] - i\sin[(2n-1)\omega_{RF}t]\} \end{bmatrix} [I_1] \tag{4.8}$$

$$\Longrightarrow$$

$$\begin{bmatrix} O_1 \\ O_2 \\ O_3 \\ O_4 \end{bmatrix} = \frac{1}{2} \begin{bmatrix} i\{J_1(m)\exp[-j\omega_{RF}t] - J_3(m)\exp[j3\omega_{RF}t] \dots\} \\ \sqrt{2}e^{i3\pi/4}\{-J_1(m)\cos(\omega_{RF}t + \pi/4) + J_3(m)\cos(3\omega_{RF}t - \pi/4)\} \\ \sqrt{2}e^{i3\pi/4}\{J_1(m)\cos(\omega_{RF}t - \pi/4) - J_3(m)\cos(3\omega_{RF}t + \pi/4)\} \\ i\{J_1(m)\exp[j\omega_{RF}t] - J_3(m)\exp[-j3\omega_{RF}t] \dots\} \end{bmatrix} [I_1]$$

Table 4.2: List of the transfer functions and optical spectra at the output ports for individual input port excitation. 4 MZM means all four differentially driven MZMs are active. 2 MZM means only $MZM_A$ and $MZM_B$ are active, other MZMs are acting as cross-over.

| | **Only one input port is energized** | | | |
|---|---|---|---|---|
| | $\boldsymbol{I_1}$ | $\boldsymbol{I_2}$ | $\boldsymbol{I_3}$ | $\boldsymbol{I_4}$ |
| $\boldsymbol{O_1}$ | $f_{4\,MZM} = i\begin{Bmatrix} J_1(m)\exp[-j\omega_{RF}t] \\ -J_3(m)\exp[j3\omega_{RF}t]\ldots \end{Bmatrix}$<br>$f_{2\,MZM} = \frac{i}{2}\begin{Bmatrix} J_1(m)\exp[-j\omega_{RF}t] \\ -J_3(m)\exp[j3\omega_{RF}t]\ldots \end{Bmatrix}$ | $f_{4\,MZM} = 0$<br>$f_{2\,MZM} = \sqrt{2}e^{\frac{i3\pi}{4}} \times \begin{Bmatrix} -J_1(m)\cos\left(\omega_{RF}t \pm \frac{\pi}{4}\right) \\ +J_3(m)\cos\left(3\omega_{RF}t \mp \frac{\pi}{4}\right) \end{Bmatrix}$ | $f_{4\,MZM} = 0$<br>$f_{2\,MZM} = \sqrt{2}e^{\frac{i3\pi}{4}} \times \begin{Bmatrix} J_1(m)\cos\left(\omega_{RF}t \mp \frac{\pi}{4}\right) \\ -J_3(m)\cos\left(3\omega_{RF}t \pm \frac{\pi}{4}\right) \end{Bmatrix}$ | $f_{4\,MZM} = i\begin{Bmatrix} J_1(m)\exp[j\omega_{RF}t] \\ -J_3(m)\exp[-j3\omega_{RF}t]\ldots \end{Bmatrix}$<br>$f_{2\,MZM} = \frac{i}{2}\begin{Bmatrix} J_1(m)\exp[j\omega_{RF}t] \\ -J_3(m)\exp[-j3\omega_{RF}t]\ldots \end{Bmatrix}$ |
| $\boldsymbol{O_2}$ | $f_{4\,MZM} = 0$<br>$f_{2\,MZM} = \sqrt{2}e^{\frac{i3\pi}{4}} \times \begin{Bmatrix} -J_1(m)\cos\left(\omega_{RF}t \pm \frac{\pi}{4}\right) \\ +J_3(m)\cos\left(3\omega_{RF}t \mp \frac{\pi}{4}\right) \end{Bmatrix}$ | $f_{4\,MZM} = i\begin{Bmatrix} J_1(m)\exp[j\omega_{RF}t] \\ -J_3(m)\exp[-j3\omega_{RF}t]\ldots \end{Bmatrix}$<br>$f_{2\,MZM} = \frac{i}{2}\begin{Bmatrix} J_1(m)\exp[j\omega_{RF}t] \\ -J_3(m)\exp[-j3\omega_{RF}t]\ldots \end{Bmatrix}$ | $f_{4\,MZM} = i\begin{Bmatrix} J_1(m)\exp[-j\omega_{RF}t] \\ -J_3(m)\exp[j3\omega_{RF}t]\ldots \end{Bmatrix}$<br>$f_{2\,MZM} = \frac{i}{2}\begin{Bmatrix} J_1(m)\exp[-j\omega_{RF}t] \\ -J_3(m)\exp[j3\omega_{RF}t]\ldots \end{Bmatrix}$ | $f_{4\,MZM} = 0$<br>$f_{2\,MZM} = \sqrt{2}e^{\frac{i3\pi}{4}} \times \begin{Bmatrix} -J_1(m)\cos\left(\omega_{RF}t \pm \frac{\pi}{4}\right) \\ +J_3(m)\cos\left(3\omega_{RF}t \mp \frac{\pi}{4}\right) \end{Bmatrix}$ |
| $\boldsymbol{O_3}$ | $f_{4\,MZM} = 0$<br>$f_{2\,MZM} = \sqrt{2}e^{\frac{i3\pi}{4}} \times \begin{Bmatrix} J_1(m)\cos\left(\omega_{RF}t \mp \frac{\pi}{4}\right) \\ -J_3(m)\cos\left(3\omega_{RF}t \pm \frac{\pi}{4}\right) \end{Bmatrix}$ | $f_{4\,MZM} = i\begin{Bmatrix} J_1(m)\exp[-j\omega_{RF}t] \\ -J_3(m)\exp[j3\omega_{RF}t]\ldots \end{Bmatrix}$<br>$f_{2\,MZM} = \frac{i}{2}\begin{Bmatrix} J_1(m)\exp[-j\omega_{RF}t] \\ -J_3(m)\exp[j3\omega_{RF}t]\ldots \end{Bmatrix}$ | $f_{4\,MZM} = i\begin{Bmatrix} J_1(m)\exp[j\omega_{RF}t] \\ -J_3(m)\exp[-j3\omega_{RF}t]\ldots \end{Bmatrix}$<br>$f_{2\,MZM} = \frac{i}{2}\begin{Bmatrix} J_1(m)\exp[j\omega_{RF}t] \\ -J_3(m)\exp[-j3\omega_{RF}t]\ldots \end{Bmatrix}$ | $f_{4\,MZM} = 0$<br>$f_{2\,MZM} = \sqrt{2}e^{\frac{i3\pi}{4}} \times \begin{Bmatrix} J_1(m)\cos\left(\omega_{RF}t \mp \frac{\pi}{4}\right) \\ -J_3(m)\cos\left(3\omega_{RF}t \pm \frac{\pi}{4}\right) \end{Bmatrix}$ |
| $\boldsymbol{O_4}$ | $f_{4\,MZM} = i\begin{Bmatrix} J_1(m)\exp[j\omega_{RF}t] \\ -J_3(m)\exp[-j3\omega_{RF}t]\ldots \end{Bmatrix}$<br>$f_{2\,MZM} = \frac{i}{2}\begin{Bmatrix} J_1(m)\exp[j\omega_{RF}t] \\ -J_3(m)\exp[-j3\omega_{RF}t]\ldots \end{Bmatrix}$ | $f_{4\,MZM} = 0$<br>$f_{2\,MZM} = \sqrt{2}e^{\frac{i3\pi}{4}} \times \begin{Bmatrix} -J_1(m)\cos\left(\omega_{RF}t \pm \frac{\pi}{4}\right) \\ +J_3(m)\cos\left(3\omega_{RF}t \mp \frac{\pi}{4}\right) \end{Bmatrix}$ | $f_{4\,MZM} = 0$<br>$f_{2\,MZM} = \sqrt{2}e^{\frac{i3\pi}{4}} \times \begin{Bmatrix} J_1(m)\cos\left(\omega_{RF}t \mp \frac{\pi}{4}\right) \\ -J_3(m)\cos\left(3\omega_{RF}t \pm \frac{\pi}{4}\right) \end{Bmatrix}$ | $f_{4\,MZM} = i\begin{Bmatrix} J_1(m)\exp[-j\omega_{RF}t] \\ -J_3(m)\exp[j3\omega_{RF}t]\ldots \end{Bmatrix}$<br>$f_{2\,MZM} = \frac{i}{2}\begin{Bmatrix} J_1(m)\exp[-j\omega_{RF}t] \\ -J_3(m)\exp[j3\omega_{RF}t]\ldots \end{Bmatrix}$ |

It can be seen from equation (4.8) that frequency shifting utilizing the SSB modulation in one IQ modulator can be obtained by the proposed two parallel IQ modulator architecture. Removing a part of the circuit from the operation without physically disconnecting it offers a valuable degree of freedom in any photonic integrating architecture. Equation (4.8) verifies that apart from the optical loss, the reduced circuit can still offer electric to optical frequency up-conversion with the same spatial specification and spectral purity.

It can be observed from equation (4.7) and (4.8) that the lower and upper optical first-order harmonics are conveniently spatially separated and available from output port $O_1$ and $O_4$ when only input port $I_1$ is coupled to the optical source. The 3rd order harmonics can be suppressed by properly selecting the RF amplitude. Table 4.2 lists all the complementary frequency shifting

combination possible when only one input port is operating. This facilitates remote heterodyning for wireless access network using a digital coherent RoF system. One of the two harmonics can be modulated by a second IQ modulator and the two harmonics combined and propagated through the optical fiber. After its transmission to a high-speed photodetector at the remote antenna, the two harmonics beat to produce a modulated RF carrier with a center frequency equal to the double of the RF frequency. The multiplication factor is small and so, high RF frequency is needed to access the millimeter-wave regime.

## 4.4 Silicon Photonic Modulator

One of the key components of the proposed dual-parallel IQ modulator is the MZI structure with a phase modulators in in each arm. Balanced and identical operation in terms of amplitude/power and phase relationship is mandatory to obtain the ideal outcome. Up-conversion at high frequencies requires the modulators to have large bandwidth. Power dissipation, insertion loss, footprint etc. are also important factors to be considered. Besides, the RF and DC bias sources that drive the modulators must be of high quality to avoid compromising performance.

The mature $LiNbO_3$ technology offers large bandwidth, minimized effects of dispersion and stable operation over temperature [138-139]. Its lack of inversion symmetry causes the Pockels effect to dominate which offers linear electro-optic phase modulation. Another material platform offering high speed performance is group III–V semiconductor compounds [140-141] but Si has emerged as a strong competitor by taking advantages of the mature CMOS manufacturing infrastructure. The combination of photonic and electronic functionalities in a monolithic integrated structure offers the benefits of volume manufacturing e.g. reduced cost to fabricate, ease of large scale integration, miniaturisation, repeatability and improvement of component reliability. The important characteristics that a Si modulator should have includes low power consumption, high modulation speed, small footprint, large optical bandwidth and robust thermal sensitivity. In addition to the SOI modulator platform, excellent progress has been made in hybrid devices where other materials are incorporated with the SOI waveguides to achieve modulation, including electro-optic polymers [142-143], germanium [144-146], GeSi [147-150], group III–V materials [151], $LiNbO_3$ [139] and graphene [152-153]. Table 4.3 summarises the designs and performances of some of the key devices which have contributed to the evolution of Si photonic modulation.

The linear electro-optic (Pockels) effect is absent in unstrained pure crystalline silicon. However, the quadratic electro-optic (Kerr) effect and the Franz-Keldysh (FK) effect are present. The required electric field for these effects to introduce change in refractive index of Si on the order of $\Delta n \approx 10^{-4}$-$10^{-6}$ is very high and wavelength dependent [154]. Application of these weak effects alone in the pure silicon is not sufficient to obtain high performance modulation in telecommunication wavelengths of 1.3 μm and 1.55 μm. Another technique is to utilize the thermal modulation of pure Si which has a significant thermo-optic coefficient ($\Delta n/\Delta T \approx 1.86 \pm 0.08\ K^{-1}$ at wavelength 1.5 μm) [155]. This effect is rather slow (<1 MHz), and cannot be applied to the high frequency applications in the modern telecommunication system [156].

The most conventional method of achieving modulation in Si devices so far has been to exploit the plasma dispersion effect, in which the variation of the free charges concentration in silicon is

responsible for the changes in the real and imaginary parts of the local refractive index and thus phase modulation of a guided wave travelling through the active region. Soref and Bennett quantified the variations in refractive index and absorption due to the changes in the free carrier densities in silicon [154]. For a vacuum wavelength of 1.55 μm, these variations can be expressed as:

$$\Delta n = -[(8.8 \times 10^{-22})\Delta N_e + (8.5 \times 10^{-18})(\Delta N_h)^{0.8}]$$
$$\Delta \alpha = [(8.5 \times 10^{-18})\Delta N_e + (6.0 \times 10^{-18})\Delta N_h] \quad (1)$$

where $\Delta n$ and $\Delta \alpha$ are the changes in refractive index and absorption of Si, and $\Delta N_e$ and $\Delta N_h$ are the variations in free-electron and free-hole densities. Most studies, which are based on the plasma dispersion effect, have employed three common methods to electrically manipulate the charge density interacting with the propagating light in the Si waveguide: carrier accumulation, injection and depletion.

Most of the early Si modulator researches have exploited the carrier injection into a region in the silicon waveguide where light is propagating. In general, Si waveguide with embedded p-i-n diode structure acts as a charge injection-based electro-optic phase modulator (Figure 4.3(a)). Modulation of the forward bias of the diode leads the injected carrier concentration in the intrinsic region to vary, resulting in a variation of local refractive index [157-163]. The interaction of the optical field and variation of refractive index results in phase modulation of the field, which can be maximized by carefully profiling the doping concentration and optimizing the waveguide

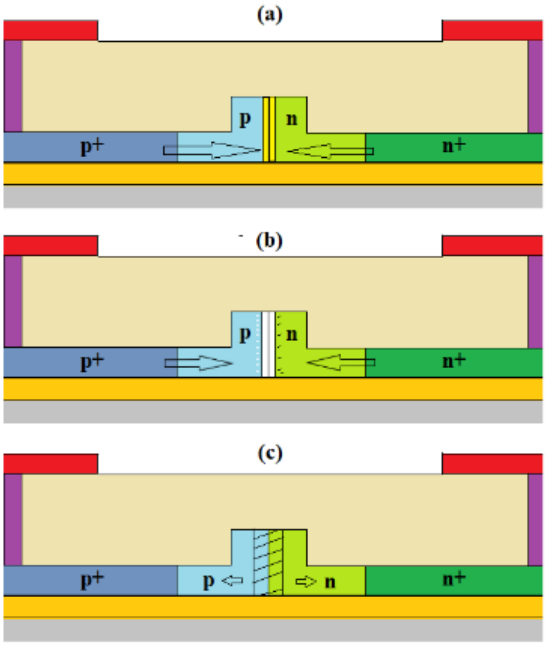


Figure 4.3 Cross sections of typical plasma dispersion based Si modulator device structures (a) carrier injection based diode structure where forward biasing causes the carrier flow in the intrinsic region; (b) carrier accumulation structure where electric field applied causes the charge density to change around the insulating layer; and (c) carrier depletion based diode structure where carrier are swept away from the depletion region by the application of reverse bias voltage

dimensions. This forward biased p-i-n diode approach can offer high modulation efficiency and small device scale. However, the slow carrier generation and/or recombination processes limits the modulation speed unless the carrier lifetime can be significantly reduced [163].

Figure 4.3(b) shows the generalized carrier accumulation structure where the phase shifting element is a MOS-type capacitor embedded in Si rib waveguide. The application of electric field leads to the accumulation of free carriers on either side of the dielectric layer which modifies the refractive index profile of the waveguide and ultimately the optical phase of the light passing through.

The functionality of this type of devices does not involve slow carrier generation and/or recombination processes and so, faster operation can be achievable [164-167]. Although plasma dispersion effect is polarization independent in nature, the oxide layer in the waveguide induces birefringence of the modal characteristics which leads to strong polarization dependence of the phase modulation efficiency. [154],[164].

A carrier depletion based optical phase modulator consists of a reverse biased p-n diode formed in a Si waveguide which tailors the refractive index profile by depleting the waveguide of free carriers. The overlap between the optical mode and the depletion width where the change in effective index occurs is a critical condition to obtain high modulation efficiency with low optical loss. Faster functionality can be achieved as phase modulation is established by pushing the majority carrier away from the junction, which does not demand slow carrier generation and/or recombination processes [168-183]. Figure 4.3(c) shows the general structure of a depletion-type phase modulator.

Optimization of the structure, variation in doping profiling, junction engineering, reduction in device dimension, and implementation of faster electrodes have led to performance enhancement over the years. Most attention has been given to increasing modulation speed with a smaller footprint to meet every increasing bandwidth demands. Other important concerns are the insertion loss, modulation depth, power budget, ease-of-fabrication, optical bandwidth and temperature sensitivity. A comparative study based on several performance metrics is given in Table 4.3 which shows that over the past few decades, researchers have employed various design strategies to tailor the modulator characteristics. Horizontal [182], vertical [169] and interleaved [186] diode structures are mostly exploited. Optimization of the Si waveguide geometry is necessary to control the single mode propagation [168], polarization dependence [164], [174] and optical mode confinement [187]. Greater overlap between the charge modulation area, e.g. the depletion region of a depletion-type diode, and the optical mode is necessary for efficient phase modulation. In addition to that, optical loss can be minimized by reducing sidewall roughness and placing metallic contact regions far from regions where light propagates. Doping profiling and positioning of the p-n junction also play important roles. The speed of the Si modulator is mostly RC time constant limited. The concentration and placement of highly doped regions should be carefully chosen as they induce absorption of photon and high capacitance [173]. On the other hand, they offer lower access resistance. Different low-level doping configurations are discussed in the literature [169-178],[180],[183]. The aim is to increase modulation efficiency, decrease device length and optical

Table 4.3: Summary of some Si based modulators alongside their performance metrics for comparison. Performance metrics which are not mentioned in the publications explicitly are left blank

| **Modulator structure** | **Modulation principle** | **Material platform** | **Modulation efficiency** | **Modulation speed** | **Modulation depth** | **Insertsion loss** |
|---|---|---|---|---|---|---|
| MZI with vertical p-i-n diode on its arms [157] | Carrier injection by forward biasing the p-i-n devices | Si | – | $\tau_{response}$ = 50 ns | -4.9 dB | – |
| Fabry-Perot etalon [155] | Heating of the etalon structure | Si | – | – | – | – |
| Free space MZI with vertical p-i-n diode in one arm [158-159] | Carrier injection by forward biasing the p-i-n devices | SOI | 0.85 V-mm | – | – | – |
| Planar Fabry-Perot optical cavity [156] | Electric heating of the cavity | Si | – | 3 dB BW ≈ 700 kHz | – | – |
| Integrated MZI with MOS capacitor structure with poly-Si gate embedded in Si waveguide [164-166] | Accumulation of free carriers due to the gate voltage | SOI | 77-80 V-mm | Intrinsic BW ≈ 2.5 GHz<br>Data rate ≈ 1-4 Gb/s | DC >16 dB<br>5 dB @ 1Gb/s<br>1.3 dB @ 4Gb/s | ~15.3 dB (including coupling loss) |
| Integrated MZI with MOS capacitor with crystalline Si gate embedded in Si waveguide [167] | Accumulation of free carriers due to the gate voltage | SOI | 33 V-mm | Intrinsic BW ≈ 10 GHz<br>Data rate ≈ 10 Gb/s | 3.8 dB @ 10Gb/s | ~19 dB (including coupling loss) |
| MZI with vertical $p^+pnn^+$ diodes (simulation)[168] | Carrier depletion by reverse biasing the p-n junction | SOI | 25 V-mm | $\tau_{rise}$ ~ 0.007 ns | – | ~2 dB |
| p-i-n ring resonator coupled to a single waveguide [160] | Resonant wavelength modification by forward biasing the p-i-n junction | SOI | – | Data rate ≈ 0.4-1.5 Gb/s | DC≈15 dB | ~9 dB (including coupling loss) |
| Vertical $p^+$-nid-$n^+$ diode with a doped $p^+$ layer inserted in the non-intentionally doped (nid) region [169] | Carrier depletion by reverse biasing the p-n junction | SOI | 31 V-mm | – | – | – |
| MZI with vertical p-n diode with thin $n^+$-Si cap layer for electrical contact and capacitance limiter [170-171] | Carrier depletion by reverse biasing the p-n junction | SOI | <40 V-mm | ~20 GHz @ 30 Gb/s[170]<br>~30 GHz @ 40 Gb/s[171] | DC>20 dB<br>1 dB @ 30 Gb/s<br>1.1 dB @ 40Gb/s | <22 dB (including coupling loss) |
| Integrated MZI with horizontal $p^+$-i-$n^+$ diodes [161] | Carrier injection by forward biasing the p-i-n devices | SOI | 0.36 V-mm | Data rate ≈ 10 Gb/s (pre-emphasis) | 6-10 dB | ~12 dB |
| Horizontal p-i-n diodes with a p-doped slit embedded in the intrinsic region on the arms of MZI structure [172] | Carrier depletion by reverse biasing the p-n junction | SOI | 50 V-mm | Intrinsic BW≈10 GHz | DC ≈ 14 dB | ~5 dB |
| Thermo-optic switch based on photonic wire waveguides arranged in a dense, double spiral geometry on MZI arms [192] | Electric heating by a thin-film heater | SOI | – | ~25 kHz | DC ≈ 22 dB | ~6 dB (without coupling loss) |
| Slotted photonic crystal waveguide in SOI with void regions are infiltrated with nonlinear optical polymer [190] | Application of electric field across the slotted waveguides to exploit the Pockels' effect | SOH | – | ~40 GHz | – | – |
| Slotted photonic crystal waveguide in SOI with highly $\chi^{(2)}$ nonlinear material cover [187] | Application of electric field across the slotted waveguides to exploit the nonlinear effect | SOH | – | Intrinsic BW ≈ 78 GHz<br>Data rate ≈ 100 Gb/s | – | – |
| Lateral p-n junctions with p implant dependent junction position in the rib waveguide on MZI arms [173] | Carrier depletion by reverse biasing the p-n junction | SOI | 25.6 V-mm | Data rate ≈ 10 Gb/s | 6.1 dB @ 10 Gb/s | – |

| | | | | | | |
|---|---|---|---|---|---|---|
| Rib waveguide comprising n-region wrapped around p-region to form p-n diode [174] | Carrier depletion by reverse biasing the p-n junction | SOI | 110 V-mm (TE)<br>140 V-mm (TM) | Data rate ≈ 40 Gb/s | DC > 8 dB<br>6.5 dB @ 40 Gb/s | ~15 dB (excluding coupling loss) |
| Slotted SOI waveguide spin-coated with nonlinear organic material M1 [142] | Gate voltage applied between the Si substrate and metal electrode to obtain modulation | SOH | 58 V-mm | Intrinsic BW ≈ 60 GHz<br>Data rate ≈ 42.7 Gb/s<br>(limited by test equipment) | – | ~40 dB(due to fabrication error) |
| Lateral p-n junction with the rib section formed of only p-Si (Data for 3.5mm MZI are given only) [175-176] | Carrier depletion by reverse biasing the p-n junction | SOI | 27 V-mm [175]<br>28 V-mm [176] | Data rate ≈ 40 Gb/s[175]<br>Data rate ≈ 50 Gb/s[176] | DC ≈ 25 dB<br>10 dB @ 40 Gb/s<br>3.1 dB @ 50 Gb/s | ~15 dB[175]<br>~7.4 dB [176] |
| Lateral p-i-n diodes with a p-doped slit embedded in the intrinsic region [177-178] | Carrier depletion by reverse biasing the p-n junction | SOI | 60 V-mm [177]<br>35 V-mm [178] | Data rate ≈ 10 Gb/s[177]<br>Data rate ≈ 40 Gb/s[178] | 8.1 dB @ 10 Gb/s<br>6.6 dB @ 40 Gb/s | ~6 dB [177-178] |
| MZI with horizontal $p^+$-i-$n^+$ diode on its arms [162] | Carrier injection by forward biasing the $p^+$-i-$n^+$ devices | SOI | 0.22 V-mm | Data rate ≈ 3 Gb/s (pre-emphasis) | DC ≈ 18 dB | – |
| Lateral p-i-n GeSi diode is buttcoupled to the SOI waveguide [147] | Reverse biasing the GeSi diode to enhance absorption coefficient | GeSi | – | Intrinsic BW ≈ 38 GHz<br>Data rate ≈ 28 Gb/s | DC ≈ 5.9 dB<br>6.3 dB @ 28 Gb/s | ~4.8 dB |
| Microring modulator based on a p-n junction [179] | Carrier depletion by reverse biasing the p-n junction to shift the resonance wavelength dynamically | SOI | – | Intrinsic BW ≈ 15 GHz<br>Data rate ≈ 25 Gb/s<br>Data rate ≈ 30 Gb/s | 10.4 dB@ 25 Gb/s<br>9.4 dB @ 30 Gb/s | ~2 dB (Microring) |
| Periodically interleaved PN junctions [180] | Carrier depletion by reverse biasing the p-n junction | SOI | 24 V-mm | Intrinsic BW ≈ 55 GHz<br>Data rate ≈ 60 Gb/s<br>Data rate ≈ 70 Gb/s | 7.4 dB@ 60 Gb/s<br>6.1 dB @ 70 Gb/s | ~3.34 dB |
| SOI slot waveguide covered by electro-optic material (chromophores YLD124 and PSLD41) on MZI arms[191] | Strong interaction of the guided light within the EO cladding due to the applied electric field | SOH | 0.53 V-mm | 56 Gb/s (QPSK)<br>112 Gb/s (16QAM) | – | ~27 dB |
| Selectively grown GeSi as p-i-n diode in a recessed Si region [148-149] | Enhancement of absorption coeficient by band-tilting due to the application of electric field | GeSi | – | 3dB BW > 50 GHz [148]<br>Data rate ≈ 50 Gb/s [148]<br>Data rate ≈ 100Gb/s [149]<br>(pre-emphasis) | DC ≈ 4.2 dB[148]<br>3 dB @ 50Gb/s<br>6 dB @ 100Gb/s | ~4.4 dB [148]<br>~6 dB [149] |
| Selectively grown Ge as p-i-n diode in a recessed Si region [144] | Application of electric field modulates the absorption coefficient of Ge | Ge | – | Intrinsic BW > 50 GHz<br>Data rate ≈ 56 Gb/s | DC ≈ 4.6 dB<br>3.3 dB @ 50 Gb/s | ~5.5 dB |
| MZI with lateral p-n diode on its arms. Substrate is removed to reduce electrode transmission loss, achieve the electro-optical group index matching and realize 50-ohm impedance matching [181-182] | Carrier depletion by reverse biasing the p-n junction | SOI | – | 3dB BW > 50 GHz<br>Data rate ≈ 80 Gb/s OOK & 50 Gbaud[181]<br>Data rate ≈ 90Gb/s [182] | – | – |
| SOI slot waveguide covered by electro-optic material (SEO100) [143] | Interaction of electric field and EO organic cladding leads to the change in refractive index | SOH | 1 V-mm | 6 dB BW ≈ 25 GHz<br>Line rate ≈ 100 Gb/s | DC ≈ 14 dB<br>5-7 dB@100 Gb/s | – |
| U shaped p-n junction [183] | Carrier depletion by reverse biasing the p-n junction | SOI | 33-51 V-mm | 3dB BW ≈ 14.7 GHz<br>32 Gb/s (OOK)<br>64 Gb/s (PAM-4) | DC ≈ 25 dB<br>4.12 dB@ 32 Gb/s | ~9.8 dB |

absorption by doping profiling around the junction. It can be observed from the majority of works that the junction offset or the embedded doped slit are chosen such that the majority of the light propagating region is formed of p-type silicon. This is because the hole density change results in a larger refractive index change with lower optical absorption compared to the electron density change according to Kramers-Kronig analysis [154]. Any misalignment of the p-n junction results in a reduction in modulation efficiency which shows that tight fabrication accuracy is needed for satisfactory performance [184],[189]. Liu et al. presented a design where a single sided asymmetric silicon cap layer over the p-n junction is employed to reduce the capacitance of the phase shifter [170]. The interleaved design offers high modulation efficiency if the period of n-type and p-type region is small [180],[186]. Although junction alignment error free operation can be obtained using the interleaved structure, high volume of depletion region results in high capacitance and so high frequency operation is limited.

To minimize the RC limitation of the frequency response of the modulator, a travelling wave electrode based on a coplanar waveguide structure is incorporated to match the electrical group delay and the optical phase velocity [170]. Back reflection can be suppressed by optimizing the electrode termination impedance which maximises transfer of the RF power from the source to the device. Xiao et al. showed that the application of a substrate removal technique reduces the electrode transmission loss, achieves the electro-optical group index matching and realizes 50-ohm impedance matching, simultaneously [181-182]. Si optical modulators with generation and transmission of up to 100 Gb/s OOK signal have been presented [143],[182].

Conventional Si depletion-type phase shifter based MZIs tend to require long interaction length which results in a larger footprint, higher insertion loss, cost and power consumption. It can be seen in Table 4.3 that the $V_{\pi}L_{\pi}$ product is larger for depletion-type modulators as the propagation constant perturbation is fairly low and so modulation efficiency is comparatively smaller. The footprint of the modulator based on resonant light-confining structure, on the other hand, is typically smaller. This type of modulator consists of a ring resonator coupled to a single waveguide which enhances modulation efficiency utilizing its sharp spectral resonances. By tuning the effective index of the ring waveguide utilizing the embedded diode structure, the resonance wavelength is modified, which induces a strong modulation of the transmitted signal [160],[179]. However, these structures are highly sensitive to small variations in bias conditions, operating temperature, and fabrication tolerances due to the same narrowband resonant behavior [184].

Another alternative modulation scheme is the utilization of the strong electro-absorption (EA) effect possessed by Ge/GeSi epitaxially grown on silicon-on-insulator (SOI) wafers [144],[147-149]. The Franz–Keldysh effect (FKE) in bulk semiconductors or the quantum-confined Stark effect (QCSE) in quantum-well (QW) structures which is responsible for the EA effect permits high speed operation, smaller footprint and lower power consumption.

The hybrid material system merging silicon and nonlinear optical (NLO) polymer incorporates the strong light-confining abilities of silicon with the superior NLO properties of the polymer. This polymer employs the electronic polarization of π- conjugated organic molecules which provides extremely high Pockels coefficients for high modulation speeds extending up to frequencies in the terahertz range [188]. The slotted photonic crystal waveguide structure can exploit slow light

mechanism with low voltage application to achieve compact devices with high modulation efficiency [142-143],[187],[190-191]. The performance of the Silicon-Organic hybrid (SOH) modulator is limited by complex poling method and stability issue of the organic material due to photo-oxidation and temperature variation.

## 4.5 Device Fabrication

Figure 4.4(a) and 4.4(b) show the top-view microscope image and the mask layout of the frequency up-converter. Device fabrication was performed using the A*Star Institute of Microelectronics (IME) CMOS compatible process on a SOI wafer. The SOI wafer has a top Si thickness of 220 nm and buried oxide thickness of 2 μm [173]. The circuit consists of four 2×2 MMI-MZMs connected in parallel in between two 4×4 MMIs. The large width of the electro-optic modulator stack in comparison to the I/O-end-MMIs introduces bends. So, path-length matching becomes a critical design point. From Figure 4.4(b), it can be observed that racetrack method has been applied where

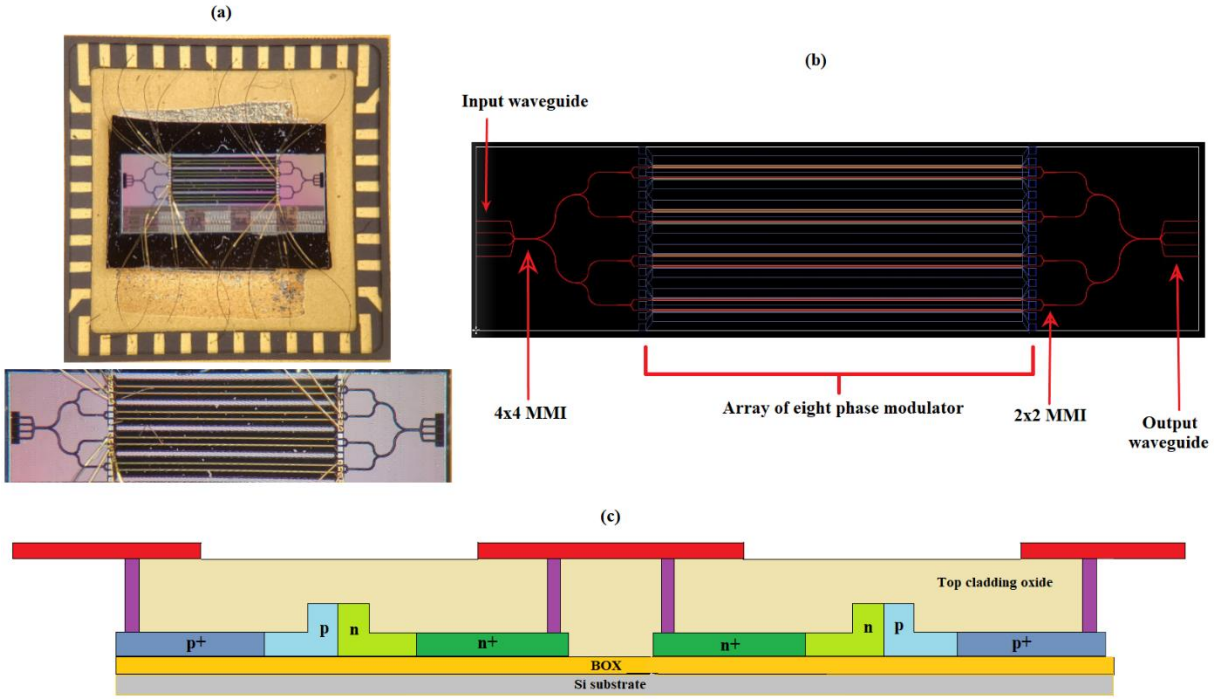


Figure 4.4 (a) Top-view microscopic image of the fabricated chip; (b) Mask layout of the device; (c) Cross-sectional diagram of the MZI arm

concentric circles are used to ensure that each lane encounters compensating short and long paths around bends. The absence of any mechanism for efficient coupling of light to and from the circuit at the edges of the chip is the primary limiter of functionality in terms of insertion loss.

Each intensity modulator is a Mach-Zehnder interferometer (MZI) with a reverse biased p-n diode structure embedded in each of the two arms. The p-n junction is formed at the middle of the Si rib waveguide between lightly doped p and n regions which extend to the slab. Figure 4.4(c) shows the cross-sectional schematic of the MZI modulation arms. To ensure good ohmic contact between

silicon and metal contacts, two slab regions are heavily doped; the distance from the rib edges is maintained so that for the rib height-slab thickness ratio, the additional optical loss due to absorption in the heavily doped region is negligible [173]. After doping, the implanted dopants were activated using a rapid thermal anneal (RTA) at 1030$^{o}$ C for 5 seconds. Two level metal system is used for interconnect. Travelling wave electrode based on coplanar waveguide structure are formed for the input of modulating signal. No termination impedance have been fabricated on the chip or applied in the experiment.

## 4.6 Experimental Result and Discussion

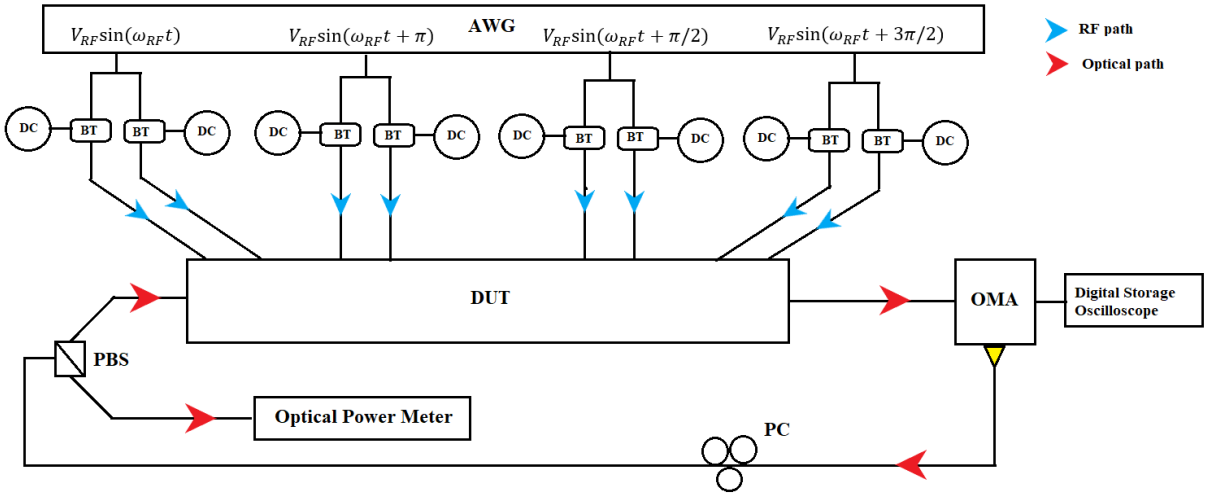


Figure 4.5 Schematic of the measurement setup. The built-in laser diode of the optical modulation analyzer (OMA) is used as the input light source to maintain better coherency at the receiver side. Light is coupled to the access waveguide at the input/output ends of the chip utilizing lensed polarization maintaining fiber. DC sources are connected to the RF signals generated from arbitrary waveform generator (AWG) via bias tees (BT). Polarization controller (PC) and polarization beam splitter (PBS) are used so that only TE is transmitted through the chip. Optical power meter is to observe the stability of the input polarization state.

The setup used for experimental demonstration of the phase shifter is sketched in Figure 4.5. The built-in laser diode of an optical modulation analyzer (Agilent N4391A) is used as the optical source. To maintain polarization of the light input to the silicon chip to be TE, a polarization controller (PC) followed by a polarization beam-splitter (PBS) is connected between the light source and the DUT. An optical power meter (Anritsu ML910B) is used to measure the power of TM component. By adjusting the PC, the TM component can be minimized and the stability of the polarization state of the input light can be observed and maintained. Lensed fibers are used for input-output coupling. The output of the silicon chip is fed back to the OMA which is connected to the digital storage oscilloscope (Infiniium DSO-20-91604A). Polarization maintaining fiber is used for all connections.

### 4.6.1 Static Assessment

To isolate individual MZI's DC characteristic, it is imperative that the other MZIs on the parallel structure are perfectly balanced and biased at their null point. The 4×4 MMIs at the edges should also be balanced in terms of splitting ratio and phase relationship. Ideally, from the structure shown in Figure 4.2(a), the MZIs are biased at their null point by design and due to the equal path length between the internal 2×2 MMIs, they are acting as a cross-over in the absence of any outside perturbation. But any minute width deviation in the high contrast SOI platform due to fabrication tolerance or poor design can create huge phase error. So in practice, for SOI one might as well assume every MZI is randomly unbalanced.

Figure 4.6 shows the variation of optical output power due to the reverse bias voltage change. Two MZMs ($MZM_A$ and $MZM_B$) are considered for the DC test and two input-output port combinations ($I_1 \rightarrow O_3$ and $I_2 \rightarrow O_3$) are taken. It can be observed from Figure 4.6(a) that over the range of the bias voltage, the notch in the transmission (minimum transmission) for biasing one arm of $MZM_A$

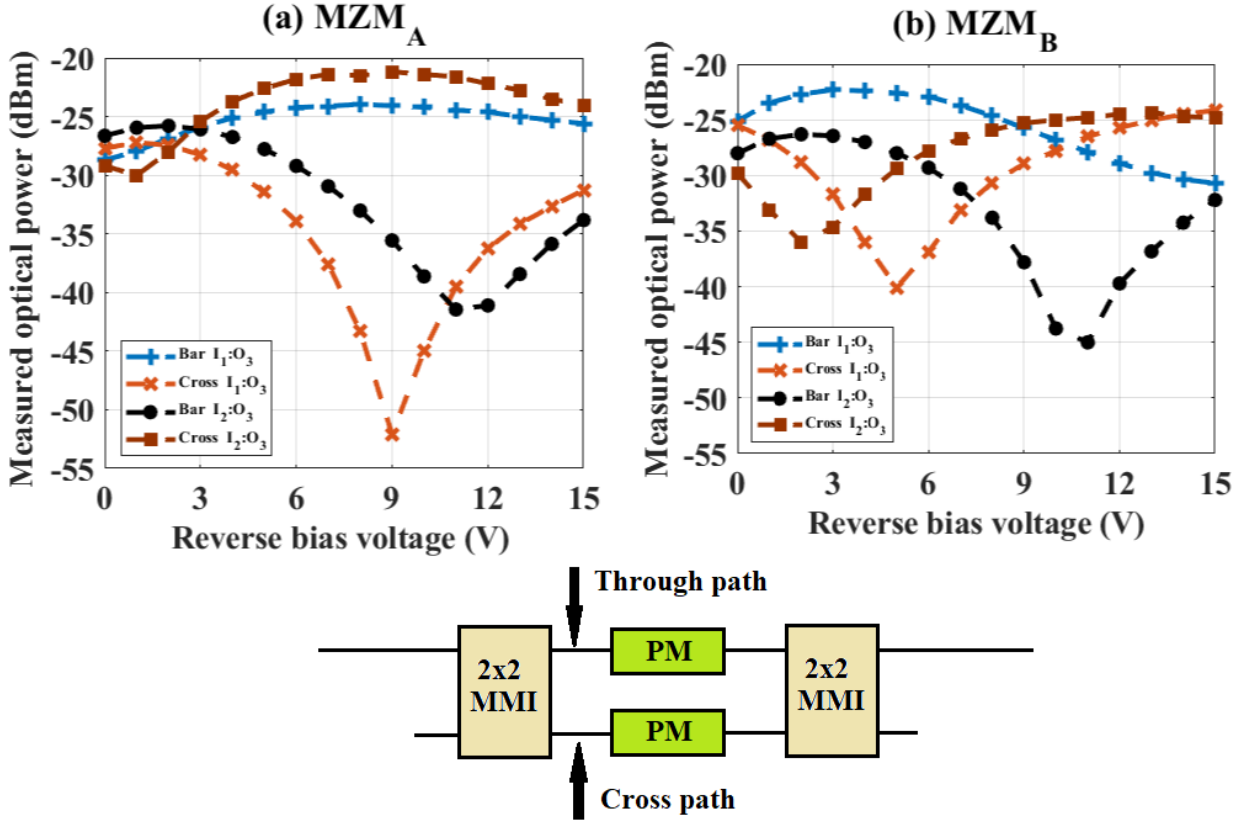


Figure 4.6 DC characteristics of the MZMs ($MZM_A$ and $MZM_B$) in terms of output optical power due to the variation of reverse bias voltage. Input port 1 & 2 are considered for light input. Output is taken from output port 3. Each MZM is asymmetrically driven which means reverse bias is applied to only one arm of the corresponding MZM: Reverse bias voltage is applied to only (a) $MZM_A$ and (b) $MZM_B$

corresponds to a flat peak transmission (maximum) for biasing the other arm. This can be expected as the light propagating through the cross arm is subjected to a total π phase shift. Their roles have been interchanged with noteworthy deviations when the input condition was changed. Similar

behaviour can be observed for $MZM_B$ as shown in Figure 4.6(b), although there are obvious shifts in its responses relative to $MZM_A$. These data suggest that biasing of the MZMs in the device needs individual fine tuning. In addition, the contributions of the off-state, imbalanced MZMs cannot be neglected.

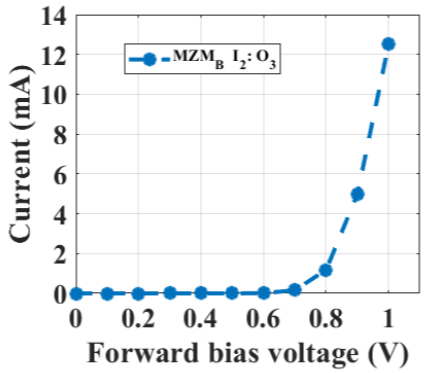


Figure 4.7 Measured forward bias I-V characteristic of a phase modulator on $MZM_B$

Figure 4.7 shows the forward bias I-V characteristic of a phase modulator in one arm of $MZM_B$. A similar measurement can be found in [135],[137] which determines that the diode performance has not deteriorated over the years.

### 4.6.2 Dynamic assessment

Individual characterization of the MZMs continued with the application of RF input. An arbitrary waveform generator (Fluke 294) with sinusoid frequency limited to 40 MHz is used as the RF source. $MZM_B$ is driven differentially. Two channels from the arbitrary waveform generator (AWG) provide two 10 MHz sinusoidal signals with one is π phase shifted relative to the other.

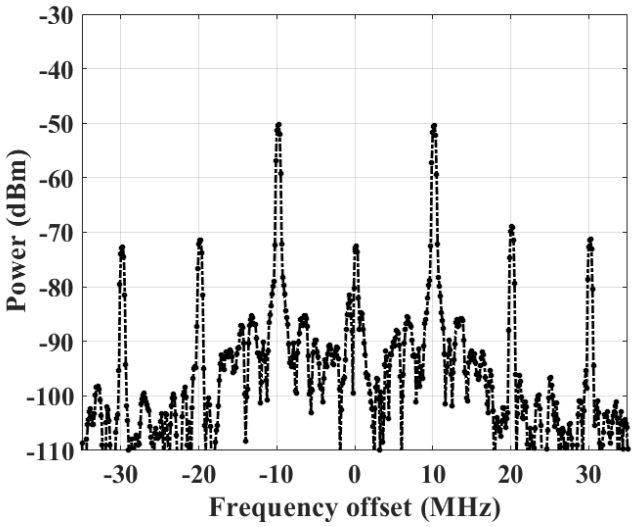


Figure 4.8 Optical spectrum of the circuit when only one MZM ($MZM_B$) is modulating.

The RF amplitude has not been adjusted to maximize the desired harmonic. The output optical spectrum is shown in Figure 4.8. The horizontal axis is the relative frequency with respect to the optical frequency of the input light and the vertical axis is the optical spectrum received at the OMA. The carrier frequency is 193.4125 THz and the resolution bandwidth of the OMA is 477.42 kHz. In an ideal scenario, a differentially driven MZM biased at its MITP acts as an intensity modulator. For a pure tone modulating signal, carrier and even order harmonics are completely suppressed where harmonics are spaced by the value of RF frequency. The odd harmonics remain with intensity weighted by Bessel functions of modulation index with the same order as the harmonic. Figure 4.8 shows deviation from the ideal case. The carrier and 2$^{nd}$ order harmonics are present which reflect the fact that other MZMs are contributing to the carrier breakthrough. The imbalance in the $MZM_B$ results the imperfect suppression of the 2$^{nd}$ or any other even order harmonics. The dual-drive configuration can be exploited so that individual adjustment of the modulation voltage of each phase shifter can be performed to suppress the unwanted harmonics.

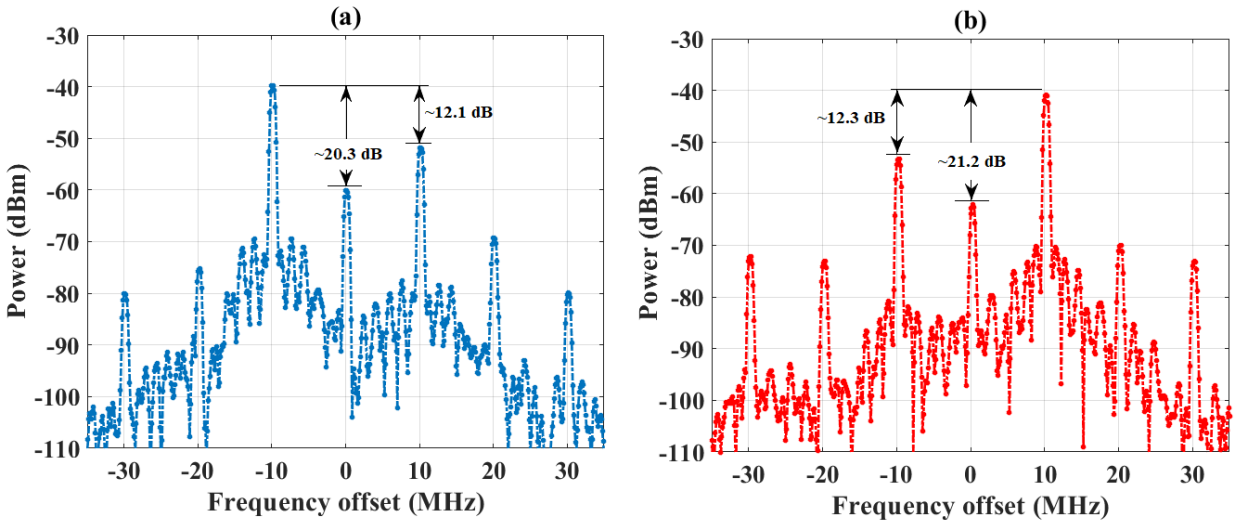


Figure 4.9 Optical spectra representing frequency shifting functionality of the fabricated circuit. (a) Frequency down-conversion at output port 1 and (b) frequency up-conversion at output port 4. The resolution bandwidth of the optical modulation analyzer is 668.388 kHz

Appropriate RF outputs from the AWG are applied to the frequency shifter circuit, shown in Figure 4.5. Light is launched into the chip through input port 1 and outputs are taken from port 1 and 4. The optical spectrums are shown in Figure 4.9. It can be observed that frequency up-conversion has been achieved. Figure 4.9(a) and 4.9(b) represent the LSB and USB modulation based frequency shifting operation. The theoretically pristine performance of the circuit is limited by the presence of carrier and undesired spurious sidebands. A carrier suppression of ~20 dB and lowest spurious harmonic suppression of ~12 dB relative to the desired harmonic have been measured.

From the optical spectra of the frequency shifter, it can be concluded that the finite extinction ratio of the MZMs, power imbalance and phase errors between the ports of the MMIs are imposing the deviations from the ideal situation. Mehedi et al. have analyzed the performance of the circuit by simulation considering these impairments [135]. They modelled their MMIs based on the results obtained in [193]. By comparing their simulation results and experimental data obtained here, it can be estimated that the impairments due to the fabrication errors are more severe than simulated. The only tuning mechanism adopted in our experiment is the adjustment of DC bias voltage. Further tuning can be done at fabrication level by incorporating additional phase shifter [194] or integrated variable coupler and variable attenuator [195] components. In addition, Miller described a self-adjustment approach to compensate for imperfect extinction ratio which could be adopted to minimize amplitude and phase imbalance [196]. Furthermore, broadband sub-wavelength engineered MMI offers reduced phase error and power imbalance which could be a viable solution [197-198].

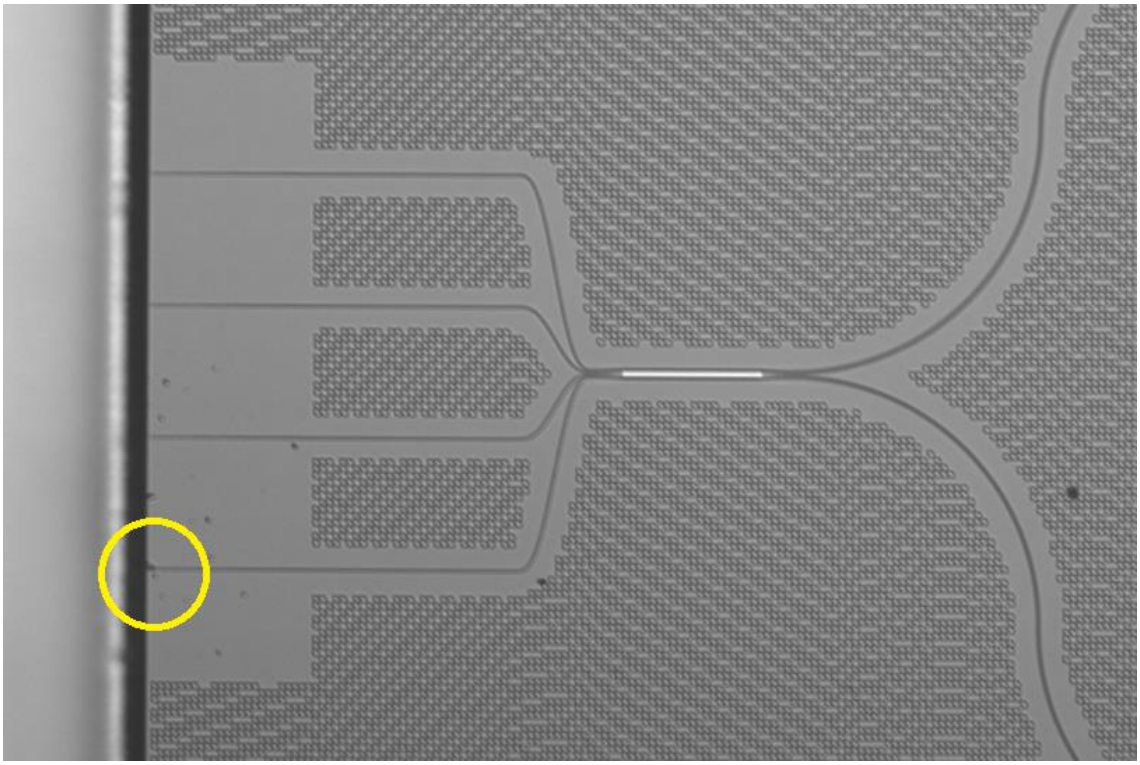

Figure 4.10 Microscopic image of the defect at the edge-end of the access waveguide

Another important observation is the high insertion loss (~20-30 dB). The principle reason is the absence of any mechanism for matching between the fiber mode and high-contrast access guide mode which could lead huge coupling loss. The lack of test structure on the chip prevents the author to measure insertion loss of individual component. It is observed that the loss varies depending upon the choice of input-output port combination. Several defects have been observed on the chip. Figure 4.10 shows a defect at one of the access guide which shows the highest loss. It is imperative that for future fabrication, the access guides should have proper coupling mechanism.

A variety of edge coupling schemes for low-loss coupling between the optical fiber and silicon photonic wire on high-contrast material platform have been proposed which can be adopted [199-200]. In addition to the structural issues, the RF amplitude has not been tuned to critically adjust the modulation index of each modulator and thus maximize 1$^{st}$ order harmonics at the output.

## 4.7 Summary

In summary, we have demonstrated an optical SSB modulation based frequency shifter on SOI platform and its performance has been evaluated. A carrier suppression ratio of ~20 dB and spurious sideband suppression ratio of ~12 dB have been achieved by only limited DC bias tuning. No additional imbalance compensating mechanism has been adopted. The quality of the operation can be improved by reducing fabrication errors, optimizing the phase shifter and MMI design and implementing integrated edge coupling and imbalance compensating technique. Although only low RF frequency operation is being reported due to the limit imposed by equipment, this device should be capable of operating in the full bandwidth of the modulators (~10 GHz).

The architecture is a multi-functional device which offers operations other than optical frequency shifting. Complex modulation, frequency multiplication for millimeter-wave application and sub-carrier generation to facilitate high data rate transmission using OFDM technology can be achieved without any modification inside the circuit. The DC bias-less design with inherently off-state MZM in parallel offers freedom to choose any modulator and flexibility to exploit and further extend its functionality. The demonstrated circuit has been fabricated using 'off-the-shelf' components as a proof of implementation feasibility. There is still scope for improvements in terms of component design and state-of-the-art fabrication to achieve compact device with low loss, low power, spectrally pure and high bandwidth operation. In addition to SOI, the circuit can be fabricated in any other material platform offering electro-optic modulator such as $LiNbO_3$, III-V or hybrid technology to exploit the advantages they render.

# Chapter 5. Phase Modulator Circuits for Vector Modulation

## 5.1 Introduction

The rapid advancement of technology demands larger quantities of information to be transferred in a faster pace with higher signal quality, greater security and digital data compatibility. The ever increasing bandwidth demand with the evolution of communication systems motivated the employment of multi-level modulation formats based on coherent technologies [201]. Among different choices of modulation techniques, IQ modulators offer high speed data transmission, advanced modulation formats and better control over generation and transmission of signals [202].

In this chapter, a generalized theory of complex modulation utilizing a generalized Mach-Zehnder interferometer (GMZI) is presented. The theory suggests that any number of phase modulator greater than two arranged in a parallel cascade can perform vector modulation scheme. A circuit consisting of three phase modulators (PM) in parallel, in contrast to the conventional architectures with four PM, can act as an IQ modulator with distortion-limited functionality. Increment of the dimension of the GMZI structure and adoption of a linear combination of in-phase and quadrature signal as the drive to constituent modulators are conjectured to be one of the condition of the ideal operation. Numerical simulation validates the operation of IQ modulator based on 3 PM-GMZI structure.

## 5.2 Contribution

A short report on vector modulation using odd number of phase modulator had been presented in the 2019 International Conference on Numerical Simulation of Optoelectronic Devices (NUSOD) [203]. This chapter discusses an elaborated and extended version of the theory utilizing phase modulator network and generalized Mach-Zehnder interferometer (GMZI) structure for linear IQ modulation. A system consisting of three parallel phase modulators as an approach to vector modulation is investigated. I drafted the papers, performed the simulations and contributed the original ideas by performing the system simulation to prove the proposed scheme's validity. Mehedi Hasan helped with circuit simulation. Dr. Karin Hinzer and Dr. Trevor Hall were the principal investigators that formulated the research project. Dr. Hall contributed to the theory, provided advice on the interpretation of the results and helped revise the manuscript.

## 5.3 Theory

A generalized Mach-Zehnder interferometer consisting of a $1\times N$ uniform splitter and a $N\times N$ discrete Fourier transform processor interconnected by an array of $N$ identical phase modulators is illustrated in Figure 5.1. The complex amplitudes $b_q$ at the output of the circuit are given by:

$$b_q = \frac{1}{\sqrt{N}} \sum_{\boldsymbol{p=0}}^{\boldsymbol{N-1}} a_p \, exp(-ipq\, 2\pi/N) \tag{5.1}$$

where $p$ and $q$ are integers that index the input and output ports of the DFT processor. Let the voltage $v_p$ applied to the phase modulator with index $p$ be a co-sinusoidal waveform of peak amplitude $v_m$, angular frequency $\Omega$ and phase shift $p2\pi/N$:

$$v_p = v_m \cos[\Omega t + p(2\pi/N)] \tag{5.2}$$

The complex amplitude $a_p$ of the carrier modulated by phase modulator $p$ is:

$$a_p = \frac{1}{\sqrt{N}} exp\left(i\pi\, v_p/v_\pi\right) = \frac{1}{\sqrt{N}} exp\{im\, cos[\Omega t + p(2\pi/N)]\} \tag{5.3}$$

where $m = \pi(v_m/v_\pi)$ is the modulation index and $v_\pi$ is the half-wave voltage of the phase modulator. Substituting equation (5.3) into equation (5.1) and invoking the Jacobi-Anger expansion yields:

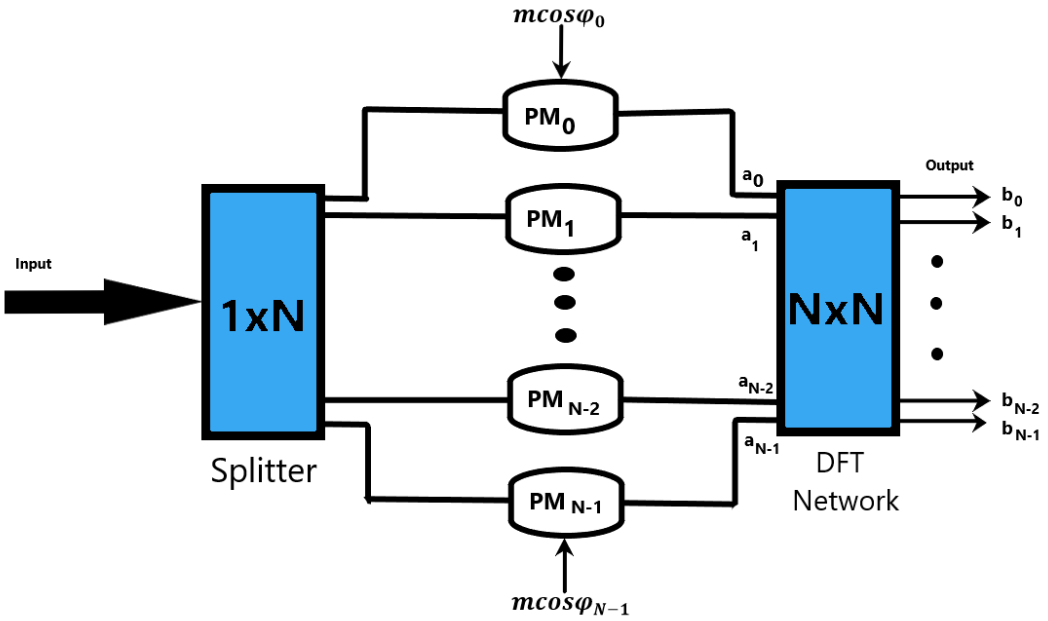


Figure 5.1 Schematic diagram of an array of $N$ phase modulators in parallel between a $1\times N$ splitter and $N\times N$ DFT network. PM: phase modulator; DFT: discrete Fourier transform.

$$\begin{gathered} b_q = \frac{1}{N}\sum_{p=0}^{N-1}\sum_{r=-\infty}^{\infty} i^r J_r(m) exp(ir\Omega t) exp(ip(r-q)\, 2\pi/N) \\ \Longrightarrow \\ b_q = \sum_{s=-\infty}^{\infty} i^{(q+sN)} J_{(q+sN)}\,(m) exp(i(q+sN)\Omega t) \end{gathered} \tag{5.4}$$

It can be observed that all carriers of order $q\ mod\ N$ exit output port $q$. The circuit architecture subsumes most RF photonic circuits in the prior art for radio frequency (RF) multiplication; in- and quadrature (IQ) phase modulation; single sideband modulation; electro-optic frequency up-conversion and frequency comb-generation given an appropriate choice of output port(s) and phase-modulator dimension $N$ as is listed in Table 5.1.

Table 5.1: Circuit architecture configurations

| Function | Dimension | Port(s) used |
|---|---|---|
| IQ modulation, SSB & electro-optic frequency conversion | N > 2 | q = 1, N - 1 |
| × N RF frequency multiplication | N = 2q | q |
| Spatially separated carrier generation | N | $q$ = 0, … , $N$ - 1 |

The general analysis of co-sinusoidal modulation predicts that the carrier of order $q\ mod\ N$ exits from port $q$. That is each port outputs a comb of carriers separated in frequency by $N\Omega$. For $N > 2$, q= -1 and $m \ll 1$ the unwanted orders are suppressed and approach zero as $m \rightarrow 0$ relative to the principal order. In that limit one can invoke linearity to extend the co-sinusoidal drive case to the general case of arbitrary IQ modulation. $N = 2$ is an exception. Two examples of $N = 4$ and $N = 3$ are given below:

### 5.3.1 Example 1 with a GMZI configuration of $N = 4$, $q = -1$

For a GMZI configuration of $N = 4$, $q = -1$, the corresponding modulation phase shifts and carrier phase shifts on each of the four arms are given in Table 5.2

Table 5.2: GMZI configuration of $N = 4$, $q = -1$

| Arm index $p$ | Modulation phase shift $\boldsymbol{\varphi = p(2\pi/N)}$ | Carrier phase shift $\boldsymbol{\phi = -pq\ 2\pi/N}$ |
|---|---|---|
| 0 | 0 | 0 |
| 1 | $\pi/2$ | $\pi/2$ |
| 2 | $\pi$ | $\pi$ |
| 3 | $3\pi/2$ | $3\pi/2$ |

The transmission of the 4 phase modulator GMZI is given by:

$$T_{4\ PM} = \frac{1}{4}[exp(i\pi\ v_0/v_\pi) + i\ exp(i\pi\ v_1/v_\pi) - exp(i\pi\ v_2/v_\pi) - i\ exp(i\pi\ v_3/v_\pi)] \quad (5.5)$$

For the special case of co-sinusoidal modulation where $v_0 = v_I = -v_2$ and $v_1 = v_Q = -v_3$, equation (5.5) becomes:

$$T_{4\ PM} = i\frac{1}{2}[\sin(\pi\ v_1/v_\pi) + i\sin(\pi\ v_q/v_\pi)] \quad (5.6)$$

A Taylor series expansion of the equation (5.6) to first order of the transmission yields:

$$T_{4\ PM} = i\frac{1}{2}\frac{\pi}{v_\pi}(v_1 + iv_Q) \quad (5.7)$$

which confirms to first order that the circuit performs general IQ modulation in the desirable Cartesian representation. This configuration corresponds to a dual parallel Mach-Zehnder modulator (DPMZM) based standard means of IQ modulation shown in Figure 5.2. Arms 0 and 2 form a first differential drive MZM driven by the in-phase component of the applied modulation and arms 1 and 3 form a second differential drive MZM driven by the quadrature-phase component of the applied modulation. The MZM pair are combined together with a relative carrier phase shift of $\pi/2$.

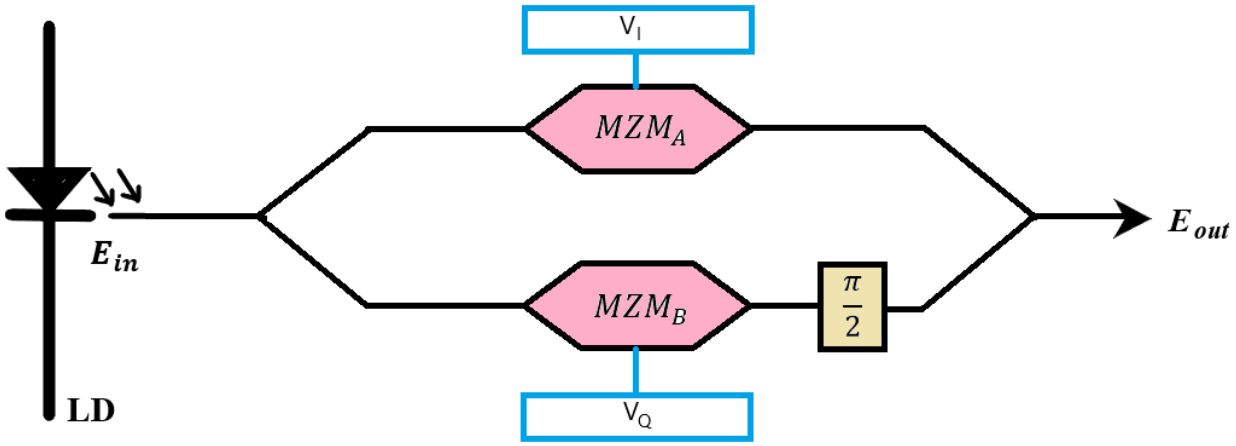


Figure 5.2 DP-MZM IQ modulator corresponding to a GMZI structure with N=4

The total transmission can be written as:

$$T_{4\,PM} = T_x + iT_y = \frac{1}{2}\sin(\pi v_I/v_\pi) + i\frac{1}{2}\sin(\pi v_Q/v_\pi) \tag{5.8}$$

where two real electrical signals are mapped linearly to the four real phase modulator electrical driving voltages. This mapping is non-invertible i.e. the four drive voltages are linearly dependent. For $N$ even this linear dependence is precisely that the drives may be arranged into $N/2$ pairs of differential drives. $N = 4$ is a special case: there are two equations for the mapping, two equations for the constraints and four unknowns.

### 5.3.2 Example 2 with a GMZI configuration of $N = 3$, $q = -1$

For a GMZI configuration of $N = 3$, $q = -1$, the corresponding modulation phase shifts and carrier phase shifts on each of the three arms are given in Table 5.3.

Table 5.2: GMZI configuration of $N = 3$, $q = -1$

| Arm index $p$ | Modulation phase shift $\boldsymbol{\varphi = p(2\pi/N)}$ | Carrier phase shift $\boldsymbol{\phi = -pq\ 2\pi/N}$ |
|---|---|---|
| 0 | 0 | 0 |
| 1 | $2\pi/3$ | $2\pi/3$ |
| 2 | $4\pi/3$ | $4\pi/3$ |

The schematic of three phase modulator GMZI structure is shown in Figure (5.3). The transmission of the GMZI is given by:

$$T_{3\,PM} = \frac{1}{3}[exp(i\pi v_0/v_\pi) + exp(i\,2\pi/3)\,exp(i\pi v_1/v_\pi) + exp(i\,4\pi/3)\,exp(i\pi v_2/v_\pi)] \tag{5.9}$$

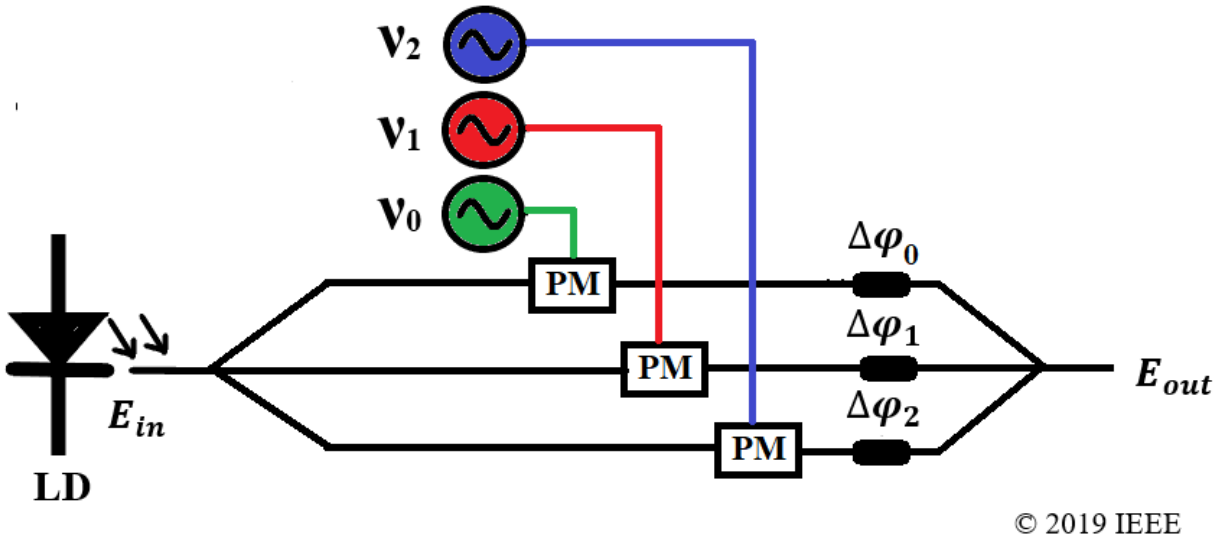


Figure 5.3 GMZI structure with 3 phase modulator

Expanding the exponentials in equation (5.9) to the first order and using the identity $[1 + \exp(i2\pi/3) + \exp(i4\pi/3) = 0]$ leads to:

$$T_{3\,PM} = \frac{1}{2} i\pi \frac{1}{v_\pi} [v_0 + v_1\, exp(i\, 2\pi/3) + v_2\, exp(i\, 4\pi/3)] + \cdots \tag{5.10}$$

For IQ modulation purpose:

$$\begin{gathered} v_0 + v_1\, exp(i\, 2\pi/3) + v_2\, exp(i\, 4\pi/3) = \; v_I + i v_Q \\ \Longrightarrow \\ \begin{bmatrix} 1 & \cos(2\pi/3) & \cos(4\pi/3) \\ 0 & \sin(2\pi/3) & \sin(4\pi/3) \end{bmatrix} \begin{bmatrix} v_0 \\ v_1 \\ v_2 \end{bmatrix} = \begin{bmatrix} v_I \\ v_Q \end{bmatrix} \end{gathered} \tag{5.11}$$

Equation (5.11) represents an under-determined system of the form **Ax = y** that does not have a unique solution. The rank of the augmented matrix is less than the unknown which corresponds to an infinitude of solutions. Rather than solving the equation, one way is to minimize the error function:

$$\boldsymbol{E = ||y - Ax||^2 = (y - Ax, y - Ax)} \tag{5.12}$$

which leads to:

$$\begin{gathered} \boldsymbol{D_x E(\cdot) = -(A\,\cdot, y - Ax) - (y - Ax, A\,\cdot)} \\ \Longrightarrow \\ \boldsymbol{D_x E(\cdot) = -(\cdot, A^\dagger y - A^\dagger A x) - (A^\dagger y - A^\dagger A x, \cdot)} \end{gathered} \tag{5.13}$$

Hence $D_x E(\cdot) = 0$ and the error is minimized if

$$\boldsymbol{A^\dagger A x = A^\dagger y} \tag{5.14}$$

where $\boldsymbol{A^\dagger}$ is the adjoint operator of **A**. Now $\boldsymbol{A^\dagger A}$ is square but for an undetermined system it still has a determinant of zero, equivalently there are solutions to:

$$\boldsymbol{A^{\dagger}Az = 0} \tag{5.15}$$

To resolve the uniqueness, the solution of smallest norm can be found by using the eigenvectors of $\boldsymbol{A^{\dagger}A}$ to invert the equation (5.14) excluding the eigenvectors with zero eigenvalues. In the case $N = 3$, there will be only be one null vector. This eigenvector describes the symmetry of the imposed constraint. The eigenvectors and eigenvalues of $\boldsymbol{A^{\dagger}A}$ are:

$$\begin{aligned} u_0 &= \tfrac{1}{\sqrt{3}}\begin{bmatrix}1\\1\\1\end{bmatrix} \quad \lambda_0 = 0 \\ u_1 &= \tfrac{1}{\sqrt{6}}\begin{bmatrix}-1\\-1\\2\end{bmatrix} \quad \lambda_1 = \tfrac{3}{2} \\ u_2 &= \tfrac{1}{\sqrt{2}}\begin{bmatrix}1\\-1\\0\end{bmatrix} \quad \lambda_2 = \tfrac{3}{2} \end{aligned} \tag{5.16}$$

Now, applying the eigenvectors excluding the one with zero eigenvalue, it can be found:

$$\boldsymbol{A^{\dagger}y \cdot u_1} = -\tfrac{1}{\sqrt{6}}\tfrac{3}{2}\left[v_I + \sqrt{3}v_Q\right] \tag{5.17}$$

$$\boldsymbol{A^{\dagger}y \cdot u_2} = \tfrac{1}{\sqrt{2}}\tfrac{3}{2}\left[v_I - \tfrac{1}{\sqrt{3}}v_Q\right] \tag{5.18}$$

which implies:

$$\begin{bmatrix}v_0\\v_1\\v_2\end{bmatrix} = \tfrac{1}{6}\begin{bmatrix}4v_I + 0v_Q\\-2v_I + 2\sqrt{3}v_Q\\-2v_I - 2\sqrt{3}v_Q\end{bmatrix} \tag{5.19}$$

Considering modulation by a pure tone: $v_I = v_m\cos(\omega t)$ & $v_Q = v_m\sin(\omega t)$ which leads to:

$$\begin{aligned} v_0 &= \tfrac{2}{3}v_m\cos(\omega t) && \Longrightarrow && v_0 = \tfrac{2}{3}v_m\cos(\omega t + \phi_0) && \phi_0 = 0 \\ v_1 &= \tfrac{2}{3}v_m[cos(\phi_1)\cos(\omega t) + \sin(\phi_1)\sin(\omega t)] && \Longrightarrow && v_1 = \tfrac{2}{3}v_m\cos(\omega t + \phi_1) && \phi_1 = 2\pi/3 \\ v_2 &= \tfrac{2}{3}v_m\,[cos(\phi_2)\cos\omega t + \sin(\phi_2)\sin(\omega t)] && \Longrightarrow && v_2 = \tfrac{2}{3}v_m\cos(\omega t + \phi_2) && \phi_2 = 4\pi/3 \end{aligned} \tag{5.20}$$

and the correct progressive RF phase shift is recovered. Utilizing equation (5.20) into equation (5.10) leads to-

$$T_{3\,PM} = i\tfrac{1}{2}\tfrac{\pi}{v_\pi}(v_I + iv_Q) \tag{5.21}$$

This demonstrates that to first order the circuit performs general IQ modulation in the desirable Cartesian representation. In general, the I and Q channels should be combined as the linear combination:

$$v_p = \cos(\phi_p)v_I + sin(\phi_p)v_Q \tag{5.21}$$

where $p$ in the index of the phase modulator and $\phi_p$ is its associated progressive phase for a $N$ phase modulator GMZI.

$$\phi_p = p\frac{2\pi}{N} \tag{5.22}$$

### 5.3.3 Distortion analysis

From the above analysis, the transmission of a GMZI of dimension $N$ configured for IQ modulation is:

$$T(\rho,\xi) = \frac{1}{N}\sum_{p=0}^{N-1} exp\{i[p(2\pi/N) + \ \rho cos(\xi + p\,2\pi/N)]\} \tag{5.23}$$

where $\rho = m$ and $\xi = \Omega t$ in the forgoing analysis. A key property is that in a neighborhood of the origin of the complex plane the transmission can follow a continuous path with arbitrary encirclement of the origin while the in-phase and quadrature components of the applied modulation remain bounded:

$$\begin{gathered} T(\rho,\xi) = \frac{1}{N}\sum_{p=0}^{N-1} exp\{i[p(2\pi/N) + \ cos(p\,2\pi/N)x \ + sin(\,p\,2\pi/N)y]\} \\ x = \rho cos(\xi) \quad ; \quad y = -\rho sin(\xi) \end{gathered} \tag{5.24}$$

On account of the $2\pi$ periodicity of the functions in equations (5.23), the substitution $p \longrightarrow p + q$ only reorders the terms within the summation. Consequently:

$$T(\rho, q\ 2\pi/N) = \exp(-iq\ 2\pi/N)T(\rho,0) \tag{5.25}$$

where

$$T(\rho,0) = \ \frac{1}{N}\sum_{p=0}^{N-1} exp\{i[p(2\pi/N) + \rho\ cos(p\,2\pi/N)]\} \tag{5.26}$$

The transmission $T(\rho,\xi)$ is therefore a form of interpolation between the points represented by $\{T(\rho, q2\pi/N)|q = 0, \ldots, N-1\}$ that make up a $N$-polygon domain containing the neighborhood of the origin. Figure 5.4 depicts the path the transmission can follow for different dimension N of of GMZI. $N$ = 3 is the minimum dimension at which the interpolation is suitable for the purpose of IQ modulation but only in a rather small disk with well-behaved and thereby correctable transmission, which is inscribed within an equilateral triangle contained within the unit square centred on the origin. It can be observed from Figure 5.4 that the domain enlarges with further increase of dimension. Dimension $N$ = 4 corresponds to the orthodox configuration that by default

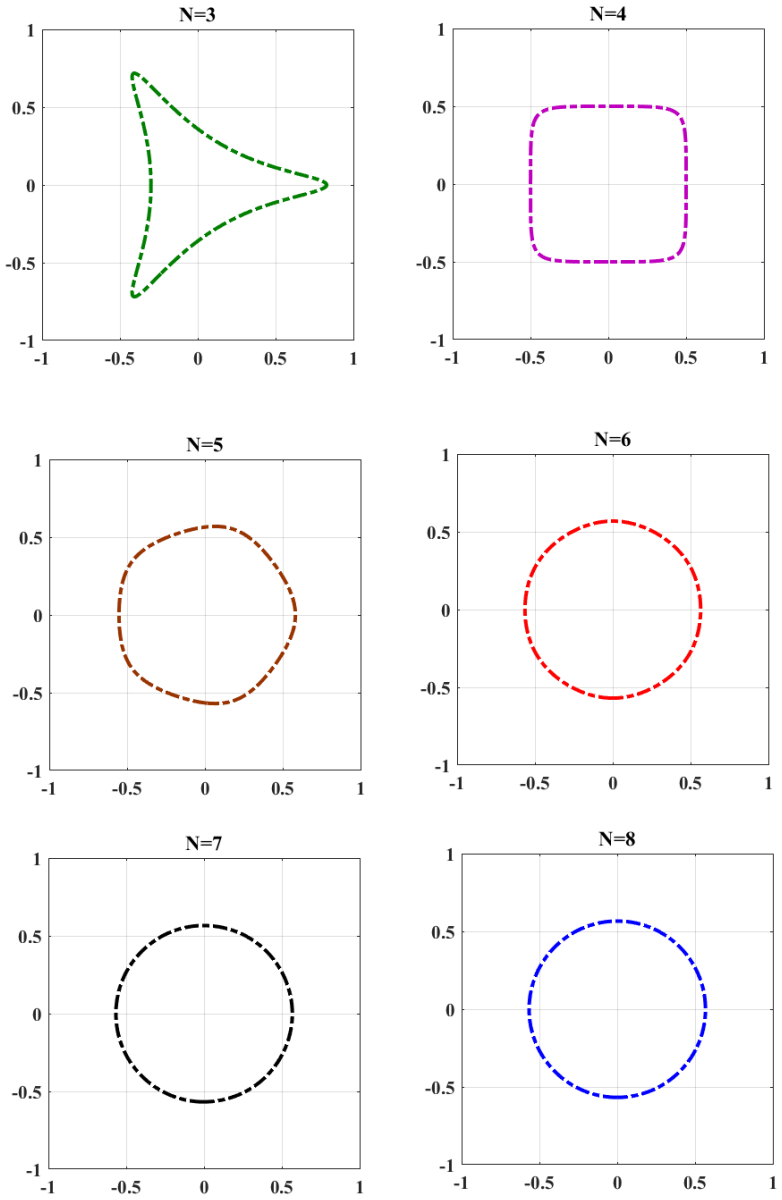


Figure 5.4 Transmission function of GMZI structure with different dimension N following a continuous path containing N-polygon domain

is considered practical. The diameter of the circle that can be inscribed within the $N = 3$ triangle is about half the diameter of the circle that may be inscribed within the $N = 4$ square. Consequently the insertion loss that must be tolerated when using the $N = 3$ rather than $N = 4$ IQ modulator as a continuous phase modulator is about 6dB greater. Circuits with lower $N$ suppress fewer harmonics generated by the nonlinearity. It is therefore no surprise that the well-behaved region decreases in size with decreased dimension increasing the insertion loss that must be tolerated for good performance. It can be suggested that increasing will result in a well-behaved region that expands as a regular polygonal approximation to a disk and hence to decreased insertion loss. From Figure 5.4, it can be observed that the circuit operation is close to ideal by $N = 6$.

## 5.4 Simulations and results for 3 PM-GMZI architecture

When a pure tone modulation is considered as in equation (5.20), the 3 phase modulator (PM) GMZI architecture provides single sideband (SSB) modulation. Equation (5.4) can be expressed for a pure tone modulation as:

$$T_{3\,PM} \approx J_1(m)\,exp(i\omega_{RF}t) + J_2(m)\,exp(-i2\omega_{RF}t)exp(i\pi/2) + \cdots \quad (5.27)$$

The operation of the 3 PM-GMZI architecture as a SSB modulator is investigated at first. Virtual Photonics Inc. (VPI) software package is used for validating the proposed architecture. A continuous wave distributed feedback (DFB) laser at a wavelength of 1550 nm with average power of 10 mW is used as the optical input. Three PMs are set in parallel with half wave voltage of each as 1V. A 10 GHz sinusoidal RF drive signal is applied to each of them. Opposite polarity (q=1 in equation (5.4)) between optical and RF phase shifts results in upper sideband (USB) operation as in equation 5.27 whereas, same polarity leads lower sideband operation (q=-1 in equation (5.4)). Progressive optical and RF phase shifts of $p2\pi/3$ $(p = 0, 1, 2)$ with opposite polarity respectively are applied to obtain USB operation.

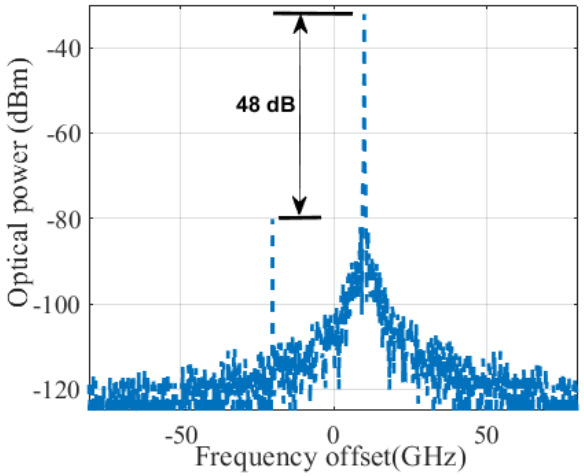




Figure 5.5 Optical spectrum of the proposed architecture when acting as a SSB modulator

Figure 5.5 shows the optical spectrum at the output of the configuration where the optical carrier and all the sidebands except the 1st harmonic at USB and 2nd harmonic at LSB are effectively suppressed. A spurious harmonic suppression ratio (SHSR) of over 48 dB is observed with an RF input of only 5 mV amplitude without any DC offset.

The linearity of the system described through the relation between the USB harmonic at +10 GHz and the LSB harmonic at −20 GHz is illustrated in Figure 5.6. SHSR linearly decreases with the increment of RF input power. Other unwanted harmonics e.g. at +40 GHz emerges at the output for RF input power with greater than -10 dBm. Satisfactory performance with RF signals having

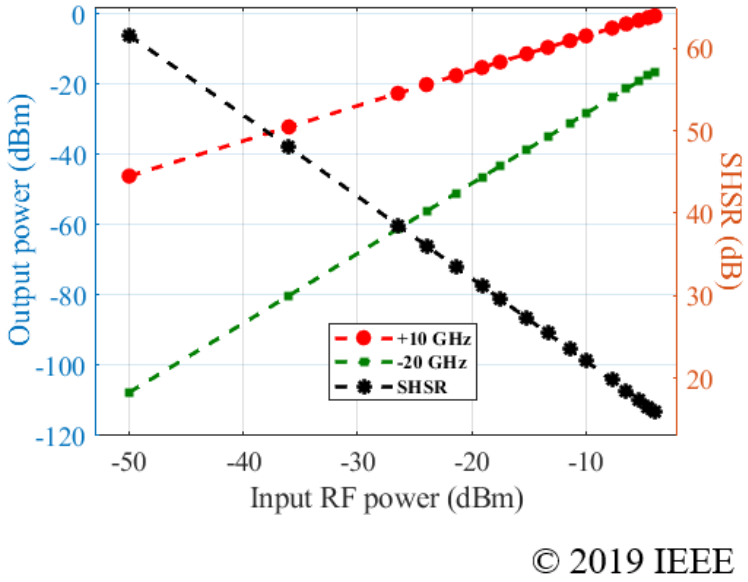


Figure 5.6 Output optical power and SHSR of the two major USB and LSB harmonics in term of RF input power

low average power can be realized with the modulator here proposed depending upon the receiver sensitivity and noise.

Drifts from the ideal condition are also investigated. Imbalance in RF drive powers to $PM_0$ and $PM_1$ is considered in Figure 5.7(a). The degradation in the performance appears from the unsuppressed 1st order harmonic at LSB whereas the optical power at -20 GHz harmonic remains almost consistent. Carrier also gains significant power above the noise level. It can be observed from Figure 5.7(a) that operation with SHSR greater than 20 dB can be achieved with a 40%

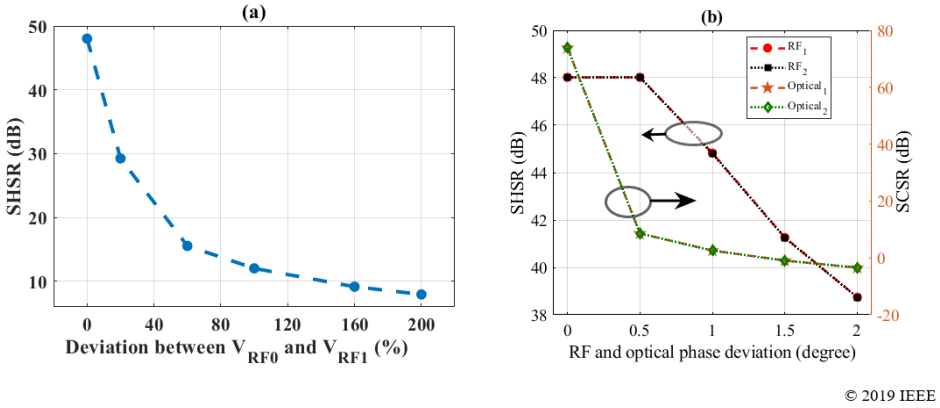


Figure 5.7 (a) SHSR variation due to the difference of RF drive amplitude between PM0 and PM1, (b) the effects of the drift in optical and RF phase on SHSR and SCSR. Identical results are obtained when the phase deviations are mirrored

imbalance in the abovementioned RF drives. The suppression of -10 GHz is also degraded when the RF phases are subjected to variation. Drift of more than ±0.5º in RF phase angle results this harmonic to be the major cause behind the decrement of SHSR, as shown in Figure 5.7(b). The

effect of optical phase drift is more severe. From equation (5.10), it can be taken that the carrier suppression by design is dependent mostly on the precise choice of optical phase difference between the arms of the architecture. From fig 5.7(b), a sharp response against the optical phase drift in terms of spurious carrier suppression ratio can be observed.

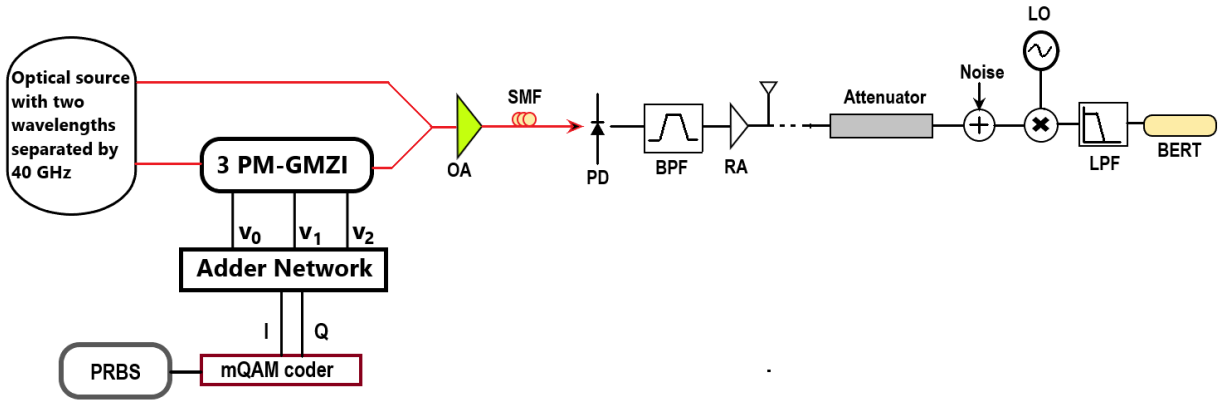


Figure 5.8 Application of the 3 PM-GMZI architecture in a radio-over-fiber downlink carrying 10 Gb/s QPSK signal. Adder network is used to produce the required drive signal as a linear combination of the I and Q signal. LO: Local oscillator, OA: Optical amplifier, PD: Photodetector, SMF: Single mode fiber, BPF: Band pass filter, RA: RF amplifier, LPF: Low pass filter, BERT: Bit error rate tester

A downlink system with the 3 PM-GMZI IQ modulator is numerically simulated. As shown in Figure 5.8, two wavelengths spatially separated with a frequency difference of 40 GHz is obtained from the optical source. Two different optical input systems are considered. The first one involves two lasers with their emission frequencies (193.1 THz and 193.14 THz) separated by 40 GHz. The second system uses the optical frequency shifter discussed in chapter 4. Two up- and down-converted $1^{st}$ order harmonics (193.12 THz and 193.08 THz) with frequency difference of 40 GHz are spatially separated and collected from two output ports. A 10 Gbit/s QPSK signal is generated from pseudo random binary sequences (PRBS) of period $2^{15}$-1. An adder network is used to provide the linear combination of the I and Q signal according to equation (5.21). This baseband signal modulates the lower frequency component. The output of the modulator is then combined with the un-modulated optical carrier using a 2×1 MMI or Y-combiner. The combined signal is then transported from the transmitter central office (CO) to the remote base station (BS) through a span of single mode optical fiber. A carrier of 40 GHz is generated at the BS by the heterodyne beating of the two components of the combined signal into a photodetector with a sufficient frequency bandwidth. Hence the information signal (PRBS in this case) is imprinted on the 40 GHz carrier. The modulated carrier is then amplified and filtered through a band-pass filter having center frequency at 40 GHz with a bandwidth equal to the 1.5 times the bit rate. The corresponding signal is then transmitted by antenna to provide the down-link of a wireless access system. In this simulation, the wireless link is emulated in one uplink approach (RF uplink) by using an attenuator with a given amount of loss and a Gaussian noise source is used to set the noise floor referred to the input of the receiver. In the simulation, the optical fiber span and corresponding optical amplifier preceding the SMF are not used.

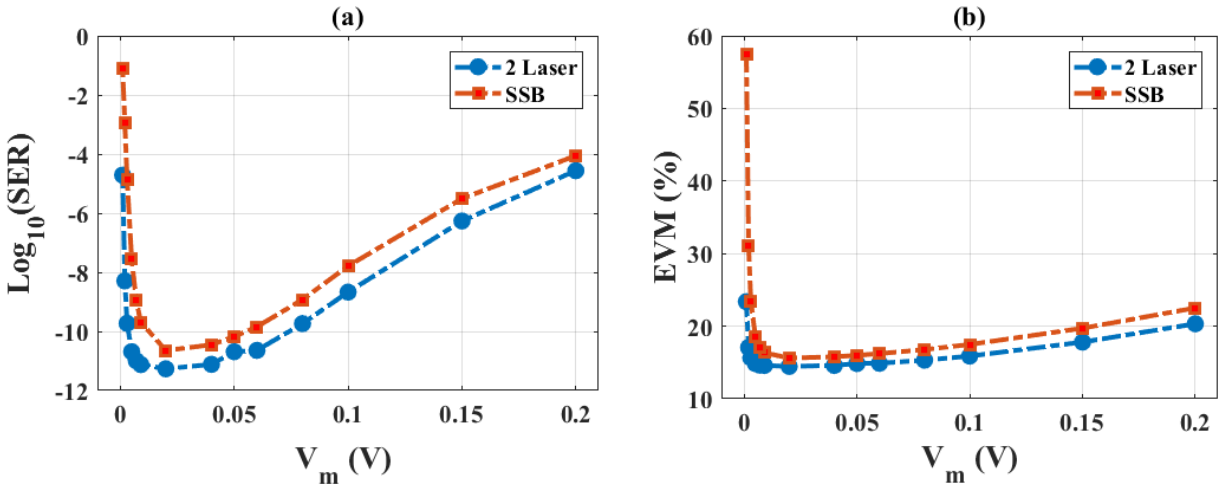


Figure 5.9 Dependence of (a) symbol error rate and (b) EVM on the weighted drive signal for two optical input system

Figure 5.9 shows the dependence of the 3 PM-GMZI IQ modulator's performance on the weighted drive signal for a signal to noise ratio (SNR) of 15 dB. It can be observed from equation (5.20) and Figure 5.6 that the linear combination of I and Q signals are needed to drive the modulators and $v_m$ is a factor that controls the magnitude of drive to the phase modulators. For a narrow range of $v_m$, the system can obtain symbol error rate (SER) > $10^{-8}$ which can be predicted from the distortion analysis. For an optical input system with two separate laser source, a SER of ~ $5.45\times10^{-12}$ (EVM ~ 14.5%)is observed for $v_m$=0.02 V. For the same specifications, the SSB modulation based frequency shifter obtains a SER of ~ $2.27\times10^{-11}$ (EVM ~ 15.6%).

Figure 5.10 shows the dependence of SER and EVM of the 3 PM-GMZI structure on signal to noise ratio (SNR). With the increment of SNR, improvement of the system's performance is observed. For an SNR of 18 dB, system with two separate laser inputs can achieve an SER of ~ $4.78\times10^{-20}$ (EVM ~ 10.7%) whereas, the system with SSB modulator as the optical source can achieve SER of ~ $1.88\times10^{-18}$ (EVM ~ 12.2%).

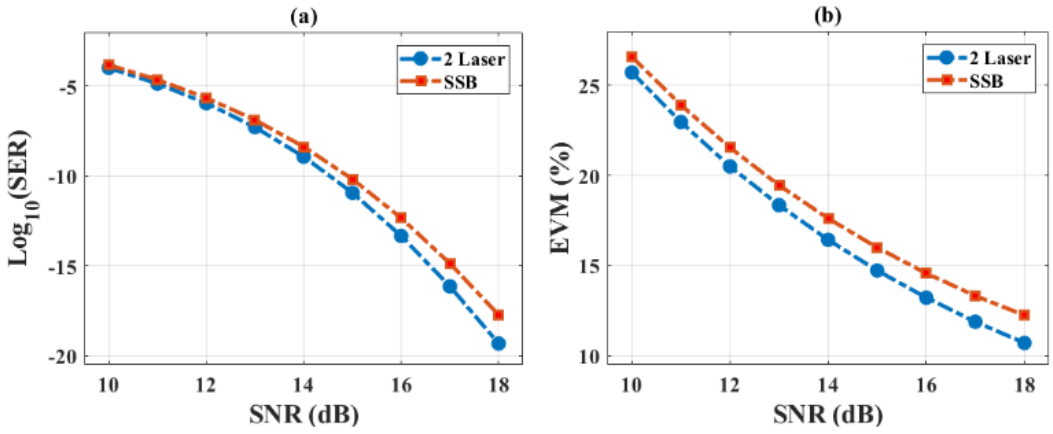


Figure 5.10 Variation of (a) SER and (b) EVM due to SNR

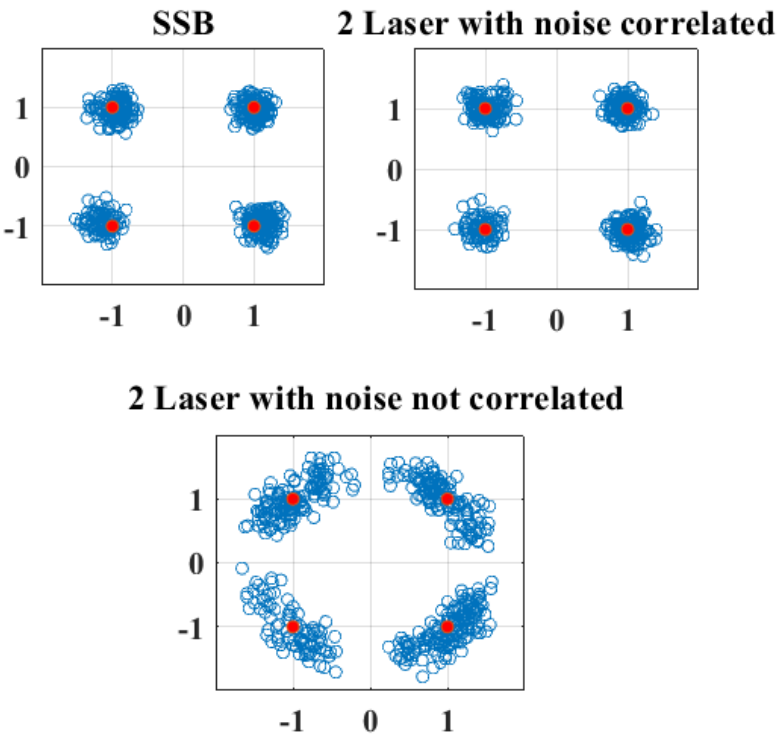


.

Figure 5.11 Constellation diagram of the system with 3 PM-GMZI IQ modulator having two different optical input system

From Figure 5.9 and 5.10, it can be observed that the 3 PM-GMZI IQ modulation system two separate laser input performs slightly better than the system with the SSB modulation based frequency shifter proposed in chapter 4. In those cases, the two lasers are taken as noise correlated. Figure 5.11 shows that when the condition of noise correlation between the lasers in system incorporating the two separate laser inputs is omitted, deviation in the constellation diagram occurred which relates to performance degradation. For the SSB modulator based frequency shifter, single laser is used and the two spatially separated USB and LSB harmonics from the two output ports are phase correlated.

## 5.5 Summary

In summary, a general analysis of N-dimensional parallel phase modulator based GMZI structure is presented and its capability of complex modulation is discussed. In addition to the conventional IQ modulator consisting of even (N=4) number of phase modulator, the analysis also predicts the realization of odd (N=3) number phase modulator based vector modulation approach. The analysis suggests that using a linear combination of in-phase and quadrature signals is the correct way of implementing the RF phase shifts [204-205] and enables the use of the various architectures to be extended to analytic signals. Numerical analysis shows that well-behaved and thereby correctable functionality can be achieved by N=3 PM-GMZI structure for a region which is smaller than higher dimensional structure, which is verified by simulation. A RoF system simulation incorporating 3 PM-GMZI IQ modulator and external modulation or SSB modulation based optical input suggests

better performance when correlation of laser phase noise is concerned. A comparison between the presented performance and that obtained in chapter 2 for a conventional IQ modulator depicts the superiority of N=4 over N=3 dimensional IQ schemes. It can be conjectured that increasing $N$ will result in a well-behaved region that expands as a regular polygonal approximation to a disk and hence to decreased insertion loss albeit that is unlikely to merit the complexity and expense.

# Chapter 6. Conclusions

## 6.1 Summary & Conclusions

The next generation access network promises to provide ubiquitous connectivity alongside high-speed, wideband, low cost and longer reach operation. It is crucial to develop millimetre-wave (mm-wave) (30-300GHz) fiber supported transport networks. Although the cost effectiveness is still an open question, simplistic base station architecture with simplified antenna units and high optical component reuse is necessary for enabling a compatible mobile network backhaul and pico-cellular wireless personal area network (WPAN). The application of mm-wave is not limited to wireless access networks only. Antenna remoting, phased-array antennas, optical sensors, radars and tera-hertz applications can also benefit from efficient generation and transmission of mm-waves.

This thesis concentrates on external modulation based radio frequency multiplication and translation which offers efficiency, stability and spectral purity. Chapter 2 discusses a generalized graphical method based on decomposing a photonic circuit to its parallel counterpart which results in a collection of optical path, tracing from input to output with transmission function depending on the optical component within it. This method is utilized to quantitatively analyze a photonic frequency multiplication circuit consisting of four Mach-Zehnder modulator (MZM) in cascade. A multiplication factor of eight has been achieved. In addition to its simple architecture, the circuit performs efficient suppression of carrier and unwanted harmonics by design for a reasonable range of RF drive input power which offers additional flexibility due to the absence of an optical or electrical filter. A comparison with three other functionally equivalent frequency octupling circuit shows that the proposed circuit possesses superior RF power efficiency and can achieve low RF input operation which makes it more suitable for low-power integrated system. The absence of any other element other than MZM can provides a low access loss option when integration on material platforms such as $LiNbO_3$, Si, or III-V is considered. A system simulation shows its possible RoF application when the $4^{th}$ order optical sidebands are separated by a frequency demultiplexer.

In chapter 3, two architectures employing polarization modulators to obtain photonic frequency multiplication function have been proposed. Both circuits are designed to achieve a multiplication factor of eight. The first proposed architecture can provide an operation for a wide range of modulation index and without any adoption of optical or electrical filter which offers flexibility and tunability. The second circuit offers a low RF drive operation. In each circuit, an intensity modulator is realized by cascading polarization modulator and polarizer. By setting the polarizer angle and polarization state of the input light to each polarization modulator, the biasing condition of the intensity modulator can be determined. The employment of a polarization modulator instead of a Mach-Zehnder modulator, which is the orthodox choice for an intensity modulator, has been proven to provide DC bias free operation. Hence, bias drift related problems can be avoided. In addition to that, high extinction ratio and robust operation against path-length error and environmental perturbations facilitates implementation with discrete components.

In chapter 4, a multifunctional circuit fabricated on SOI platform has been discussed. The circuit can offer sub-carrier generation, frequency octupling function, IQ modulation and frequency

translation, where activation of any of these functions only needs distinct RF drive and bias conditions from outside. An MZI structure utilizing MMIs as its input and output splitters is adopted. The intrinsic phase relationship among the input and output ports is employed to bias the MZI to its null point by design. An experiment has been conducted to investigate this circuit's frequency shifting capability. In principle, the circuit has the framework of two parallel IQ modulator where all the optical phases needed for biasing the MZI structures are provided by MMIs, which results in a DC free design. Another important feature is that the circuit can deliver two spatially separated up- and down-converted optical harmonics from two separate ports. This enables the circuit to generate two spatially separated carrier from a single laser source which can be utilized in remote heterodyning for wireless access network using a digital coherent Radio-over-Fiber (RoF) system. A carrier suppression ratio of ~20 dB and spurious sideband suppression ratio of ~12 dB have been achieved. Individual MZM characteristics have been investigated to determine the reasons behind the deviation from the ideal outcome. It is conjectured that imbalance in the MMIs is the principle cause. Only DC bias tuning is implemented in the experiment. The absence of efficient on-chip coupling-to-fiber mechanism results in high insertion loss.

Finally, a generalized theory of GMZI structure based IQ modulation has been presented in chapter 5. The theory predicts that a 3 phase modulator MZI structure can yield the IQ modulation function. A linear combination of the in phase and quadrature signal is needed to drive the phase modulators which complicates the process when compared to the conventional four phase modulator based IQ modulation scheme. A system simulation has been presented to validate the theory. It has been observed that when two separate laser sources are used for heterodyning system, phase correlation between them is crucial. A simulated version of the fabricated circuit discussed in chapter 4 has also been used with the 3 phase modulator based vector modulation system.

## 6.2 Discussion & Suggestions for Further Work

The thesis concentrates on electro-optic photonic integrated circuits which can offers functionalities such radio frequency multiplication, translation and IQ modulation. The simulation results and experimental data are encouraging. Realization of these circuits in their integrated formats while considering practical issues with design and material platform is the next step. Some suggestions for future work are offered below.

1. The immediate next step is the investigation of other functionalities of the chip discussed in chapter 4. The circuit is capable of sub-carrier generation, IQ modulation, frequency 8-tupling and frequency translation. The features involving translated carrier generation at the output from a single source and spatial separation between them enable the transmission of phase correlated carriers without adopting complicated system to maintain coherency and to frequency demultiplex. Although the Mach-Zehnder modulators have a bandwidth of 10 GHz, experiments were limited by the arbitrary waveform generator to 10 MHz. A high frequency experiment should be executed to determine its feasibility in RoF communication. The sub-carrier generation is an interesting option as it enables frequency 6-tupling with two principle optical harmonics from two different output ports [135]. A V-band 60 GHz signal can be generated from a RF drive of 10 GHz in a digital coherent RoF downlink system.

2. The fabricated circuit discussed in chapter 4 has shown deviations from an ideal outcome. Carrier and other unwanted harmonics, which should be suppressed by design, emerge and deteriorate the spectral purity. It has been conjectured that one of the principle reasons is the imbalance in MMIs which results in a finite extinction ratio of the MZMs. In addition, high coupling loss has also been observed due to the absence of a proper on-chip mechanism for matching between the fiber mode and high-contrast access waveguide mode. These can be avoided by introducing bias tuning mechanism employing tunable phase shifter on the arms of MZMs, variable coupler and a grating coupler at the access guide. Due to the presence of MMI which is controlling the biasing condition of the MZM with its intrinsic phase relation between its ports, the imbalance can be handled with a narrow-range tunable phase shifter. Besides, integrated variable coupler and variable attenuator, broadband sub-wavelength engineered MMI and Miller's self-adjustment approach can be adopted to compensate for imperfect extinction ratio which could be adopted to minimize amplitude and phase imbalance [195-197]. In addition to that, the silicon layer thickness on SOI platform is typically chosen to be 220 nm; a de facto microelectronics industry standard. However, it is not clear that this thickness is the best choice for photonics [206]. Other choices which offer linear electro-optic modulator can be considered for future fabrication alongside the modification needed in the present design to overcome the issues related to imbalance and loss.
3. The simulation results of the frequency multiplication circuit in chapter 2 have shown a prospective opportunity to be a viable solution for millimeter-wave generation and transmission. The straightforward structure without additional splitter/coupler or phase shifter will simplify the design for integration and minimizes the additional loss and imbalances. The Mach-Zehnder modulators incorporated in the architecture are biased at their minimum transmission point, which is same as the MZMs used in the PIC discussed in chapter 4. Adoption of MMI as the splitter/combiner of the MZM in the proposed frequency octupling system simplifies the DC bias drift related problem. Besides, the interesting observation of this architecture having pristine RF component while maintaining same finite extinction ratio for each MZM should be investigated further. The first priority for a practical implementation is to choose a suitable integration technology which can offer a stable and future-proof solution. 40 GHz $LiNbO_3$ modulator has already been available commercially. Monolithic $LiNbO_3$ with a half-wave electro-optic modulation efficiency of 1.8 V·cm while operating at data rates up to 40 Gbps has been demonstrated [207]. More than 100 GHz operation has also been achieved by $LiNbO_3$ modulator on silicon [139]. InAlGaAs-based electro-optic modulators with low drive voltage ($v_\pi = 0.77\ V$) and an exceeding bandwidth of 67 GHz has also been demonstrated [105]. 112 Gb/s 16QAM signal transmission with modulation efficiency of 0.53 V-mm with electro-optic modulator on silicon-organic hybrid (SOH) has been achieved [191]. Recent developments of high-speed silicon-on-insulator (SOI) electro-optic modulator has availed the opportunity to exploit the mature CMOS manufacturing infrastructure for monolithic integration of electronic and photonic functionalities. Signal transmission in OOK format at 90 Gb/s has been demonstrated utilizing SOI modulator [182]. Recently an all-silicon IQ modulator with 100 GBaud 32QAM transmission has also been demonstrated [208]. The proposed frequency octupling architecture can take advantages of these platforms for a practical realization.

4. Although the IQ modulation with 3 phase modulator architecture in chapter 5 becomes complicated due to the linear combination of in phase and quadrature signal for driving the phase modulator, the condition becomes simpler when only SSB modulation/frequency shifting with a pure tone is considered. The proposed circuit can provide a low RF drive option for a frequency translation. A practical implementation of this can realize an integrated frequency shifter which has one phase modulator less than the conventional one which might result in a compact photonic integrated circuit.
5. It has been observed in this thesis that the RF drive phase plays an important role in attaining a better performance. Both Mach-Zehnder modulator and polarization modulator based architectures have shown degradation in performance for RF phase imbalance. In addition to the imperfect operation of RF drive sources, the length of the waveguides connecting the drive signal to the phase modulators is found to be another critical design point. It is imperative to sort out proper methods to generate and incorporate required phase relationship of the RF drive signal in the architecture. In addition to that, long-term stability issues particularly dc bias drift should be addressed.

# Appendix I. List of Photonic Frequency Multiplication Techniques for Millimeter-wave Generation

A detailed list that summarizes some of the works related to mm-wave generation with frequency multiplication functionality is presented below:

Table I.1: Summary of some photonic frequency multiplication techniques with, unless otherwise specified, experimental results

| Short description | Multiplication factor | Performance metrics |
|---|---|---|
| Mach-Zehnder modulator (MZM) biased to suppress the carrier and even order harmonics [34] | 2 (36 GHz from 18 GHz) | Signal to Noise ratio (SNR) > 35 dB |
| MZM biased to suppress the odd order optical harmonics is followed by a fixed-wavelength optical notch filter to suppress the carrier [35] | 4 (32-50 GHz from 8-12.5 GHz) | Optical sideband suppression ratio (OSSR) > 25 dB |
| Double-sideband phase modulation without suppression of carrier is achieved by a phase modulator. Band-pass filter is used to suppress the higher order harmonics. Maintaining $\pi$ phase difference between the 1$^{st}$ order optical harmonics by dispersion compensation technique, minimizing drift of laser wavelength and employment of band-limited power amplifier after the heterodyning process could minimize the carrier's effect [36] | 2 (60 GHz from 30 GHz) | OSSR > 40 dB |
| Dual parallel polarization modulator (DP-PolM) with adjustment of the polarization controllers on its two arms is used [37]. | 2 (20 GHz from 10 GHz) | Carrier suppression ratio (CSR) ~ 29.5 dB |
| Dual parallel MZM (DP-MZM) with the outer Mach-Zehnder interferometer (MZI) is biased at MITP. The sub MZMs are biased at maximum transmission point (MATP). The sub MZMs are driven by relative $\pi/2$ phase shifted RF input. No optical filtering is needed [38]. | 4 (40-72 GHz from 10-18 GHz) | Electrical side harmonic suppression ratio (ESHSR) > 38 dB (40 GHz)<br>Optical sideband suppression ratio (OSSR) > 36 dB (72 GHz) |
| DP-MZM with the outer MZI is biased at MATP. The sub MZMs are biased at minimum transmission point (MITP) [39]. | 4 (36 GHz from 9 GHz) | ESHSR > 30 dB<br>OSSR > 35.4 dB |
| Polarization modulator (PolM) on a Sagnac loop, four polarization controller, polarizer and polarization beam splitter are used [40]. | 4 (2.04-1000 GHz from 0.51-25 GHz) | OSSR ~ 32 dB (40 GHz)<br>CSR ~ 42 dB (40 GHz)<br>ESHSR ~ 17.8 dB (40 GHz) |
| Differentially driven DD-MZM is followed by a phase modulator with same RF drive frequency. Careful selection of RF drive amplitude and phase to the phase modulator and bias of the MZM lead to improving sideband extinction and variable functionality: Double sideband-suppressed carrier (DSB-SC) and Optical single sideband (OSSB) [41] | 3 (30 GHz from 10 GHz ) | OSSR > 45 dB<br>Phase noise -81.25 dBc/Hz at 10 kHz offset |
| Two cascaded differentially driven DD-MZMs biased at MATP and MITP respectively. High order | 6 (60 GHz from 10 GHz) | OSSR ~ 36 dB |

| | | |
|---|---|---|
| sidebands are suppressed by an optical band-pass filter (simulated) [42]. | | |
| MZM biased at MITP followed by 400m highly nonlinear fiber (HNLF) utilizing four wave mixing (FWM) to generate 3rd order optical harmonics. Adoption of fiber Bragg gratings is needed to filter out unwanted 1st order optical harmonics [43] | 6 (40 GHz from 6.667 GHz) | ESHSR >25 dB<br>SNR ~50 dB<br>Linewidth < 3 Hz |
| Cascaded intensity modulator (IM) and phase modulator (PM) driven by same RF frequency with a relative $\pi/2$ phase shift. Adjustment of RF drive power and introduction of tunable dispersion compensator are required to maximize the optical sidebands responsible for frequency 6-tupling [44] | 6 (36 GHz from 6 GHz) | Linewidth <20 Hz |
| Dual parallel PolM (DP-PolM) consisting of PolM and polarization controller on each of its two arms is used, followed by a polarizer. By properly controlling the direction of polarization controllers and polarizer and the phase difference of the drive signal, frequency multiplication is achieved. Strict condition on the modulation index is required to suppress unwanted sidebands (simulated) [45]. | 6 (24 GHz from 4 GHz) | OSSR > 31 dB<br>ESHSR > 25 dB |
| Two cascaded DP-MZM with all sub-MZMs are differentially driven and biased at MATP. The outer MZIs of the two DP-MZMs are biased at MITP. Carrier and odd order unwanted harmonics suppression can be achieved by design [46]. | 8 (60-80 GHz from 7.5-10 GHz) | SNR > 40 dB (60 GHz)<br>Phase noise -73 dBc/Hz at 10 kHz offset (60 GHz)<br>OSSR > 30 dB (80 GHz) |
| Dual parallel PolM (DP-PolM) consisting of PolM each of its two arms is used, followed by a polarizer. By properly controlling the phase difference of the drive signal and maintaining modulation index to a fixed value, frequency multiplication is achieved. Different frequency multiplication factor can be achieved by different polarizer settings [47]. | 4, 8 (16 GHz and 32 GHz from 4 GHz) | OSSR~ 56 dB (8-tupling)<br>ESHSR~ 49 dB (8-tupling)<br>OSSR~ 41 dB (4-tupling)<br>ESHSR~ 35 dB (4-tupling) |
| A polarization division multiplexing-dual arm MZM (PDM-DMZM) or PDM-DPMZM followed by an FBG filter to suppress carrier provides tunable multiplication factor under different DC biases and RF drive phase conditions [48]. | i) 2 (20 GHz from 10 Ghz)<br>ii) 4 (24 GHz from 6 GHz)<br>iii) 8 (28 GHz from 3.5 GHz) | OSSR > 15 dB (2-tupling)<br>OSSR > 15 dB (4-tupling)<br>OSSR > 10 dB (8-tupling) |
| Intensity modulator followed by DP-MZM with specific DC bias to the lower sub-MZM of the DP-MZM to ensure unwanted harmonics and carrier suppression. The outer MZI of the DP-MZM is MITP biased and the upper sub-MZM and IM are biased at MATP [49]. | 8 (32,40 GHz from 4,5 GHz) | OSSR ~ 18 dB<br>ESHSR ~ 15 dB<br>Phase noise ~ -90 dBc/Hz at 10 kHz offset |
| MATP-biased MZM is followed by a DP-MZM with its sub-MZMs are biased at MATP. The outer MZI of the DP-MZM is biased at MITP [50]. | 8 (80 GHz from 10 GHz) | OSSR ~ 34 dB<br>Phase noise ~ -88 dBc/Hz at 10 kHz offset |

| | | |
|---|---|---|
| A DP-MZM is placed in a Sagnac loop with its sub-MZMs and outer MZI are biased at MATP. By controlling the polarization controller to satisfy a strict condition, carrier is suppressed at the polarizer [51]. | 8 ( 24 GHz from 3 GHz) | OSSR ~ 18 dB<br>ESHSR ~ 16 dB |
| Cascade of two PolMs, each followed by polarization controller and polarizer. There is also another polarization controller before each PolM. Specific combinations of polarization state and polarizer angle, RF voltage and phase shift provide tunable multiplication factor [52]. | i) 4 (16 GHz from 4 GHz)<br>ii) 6<br>iii) 8 | i) OSSR ~ 19 dB<br>ESHSR ~ 21.35 dB<br>Phase noise ~ -95.95 dBc/Hz at 1 kHz<br>offset<br>ii) OSSR ~ 17.17dB<br>iii) OSSR ~ 15.57 dB |
| Two MATP-biased MZM are connected in series by a tunable optical phase shifter. Specific modulation index or optical notch filter is needed to be applied to achieve carrier suppression [53]. | 8 (30.4, 28 GHz from 3.8, 3.5 GHz respectively) | ESHSR ~ 10.5 dB (30.4 GHz)<br>ESHSR ~ 22 dB (28 GHz)<br>Phase noise~ 96.5 dBc/Hz at 1 kHz offset |
| Frequency multiplication is implemented by cascading a Sagnac loop containing an intensity modulator and polarization controller, polarizer and DP-MZM in series. Specific conditions on modulation indices, polarizer angle and phase angle in the optical signals in the Sagnac loop can be maintained by DC and polarization controller tuning mechanism to suppress carrier and unwanted sidebands [54] | 8 (32 GHz from 4 GHz) | OSSR ~ 20 dB<br>ESHSR ~ 17 dB |
| DP-QPSK followed by a polarization controller and polarizer is used [55]. | 8 (24 GHz from 3 GHz) | ESHSR ~ 12.6 dB |
| Nested MZM consisting of two sub-MZMs, each biased at MATP. Very narrow ranges of modulation indices provide carrier suppression by design (simulated) [56]. | 8 (40 GHz from 5 GHz) | SNR ~ 44 dB for modulation index = 2.405 |
| Outer MZI biased at MITP with each of its two arms containing a pair of MZMs in series, each biased at its MATP (simulated) [57] | 8 (60 GHz from 7.5 GHz) | OSSR ~ 70 dB<br>ESHSR > 70 dB |
| Four MZMs are in parallel, each one is biased at MATP (simulated) [58] | 8, 24 (60 GHz and 180 GHz from 7.5 GHz) | OSSR ~ 69 dB<br>ESHSR ~ 65 dB |
| Four cascaded PolMs with each PolM is followed by polarizer are used (simulated) [59] | 8 (80 GHz from 10 GHz) | OSSR ~ 66 dB<br>ESHSR ~ 60 dB |
| Cascaded FWM in a 900 m HNLF is used to amplify the harmonics generated by the MZM and generate new harmonics around the pump carrier. Additionally, the nonlinear medium is reused to actively filter a pair of desired sidebands with narrow selectivity through polarization pulling by Stimulated Brillouin Scattering (SBS) and a polarizer [60]. | i) 12 (66.71 GHz from 5.559 GHz)<br>ii) 24 (66.95 GHz from 2.78 GHz)<br>iii) 25 (69.63 GHz from 2.75 GHz) | i) ESHSR > 24 dB<br>Phase noise ~ -73.2dBc/Hz at 10 kHz offset<br>ii) ESHSR > 25.3 dB<br>iii) ESHSR > 21.1 dB |

| | | |
|---|---|---|
| Optical frequency quadrupling system consisting of DP-MZM followed by SOA to introduce FWM nonlinear effect. Two optical interleavers are used to suppress carrier and unwanted sidebands [61]. | 12 (60, 120, 210 GHz from 5, 10 and 17.5 GHz) | OSSR ~25 dB (60 GHz)<br>Phase noise ~ -57 dBc/Hz at 10 Hz offset for 60 GHz signal<br>OSSR ~ 30dB (120 GHz)<br>OSSR ~ 20dB (210 GHz) |
| Two stage (frequency quadrupling followed by frequency doubling) architecture employing MATP-biased MZM at 1st stage and MITP-biased MZM at 2nd stage is used. The quadrupled microwave harmonic from the 1st stage is the RF drive for the 2nd stage's MZM. Optical bandpass and band-elimination filters are needed for carrier and unwanted harmonics suppression [62]. | 8 (100 GHz from 12.5 GHz) | Carrier suppression ratio (CSR) > 60 dB<br>Optical sideband suppression ratio (OSSR) > 30 dB<br>SNR > 70 dB<br>Phase noise degraded by ~19.2 dB at 100 kHz offset |
| Two cascaded DP-MZM with all sub-MZMs and outer MZI structures are biased at their maximum point. Specific modulation index values must be maintained to suppress carrier and unwanted sidebands (Simulated) [63] | 16 (160 GHz from 10 GHz) | OSSR ~21.5 dB<br>ESHSR ~ 38 dB |
| Two identical DP-MZMs are cascaded with all sub-MZMs are biased at null point. The RF drive is phase shifted by 15º between the two DP-MZMs. Strict conditioning on the magnitude of modulation index is needed to suppress the unwanted harmonics (Simulated) [64]. | 24 (72 GHz from 3 GHz) | OSSR > 33 dB<br>ESHSR > 26 dB |
| DP-MZM and injected DFB slave laser are used to generate ±2nd order sidebands, lock the slave laser by one injected sideband and utilize the FWM nonlinearity to generate other sidebands. Notch filtering and tuning of the master laser are needed for carrier/unwanted harmonics suppression and tunable multiplication [65]. | i) 8 (16 GHz from 2 GHz)<br>ii) 12 (18 GHz from 1.5 GHz)<br>iii) 14 (17.5 GHz from 1.25 GHz) | i) SNR > 15 dB<br>ii) SNR > 15 dB<br>iii) SNR > 15 dB |
| Single arm MZM with adjustment of DC and RF drive amplitudes are needed for carrier and unwanted sideband suppression [66]. | 8 (72 GHz from 9 GHz) | OSSR > 18 dB<br>CSR > 37 dB |
| A uniform fiber Bragg grating based acousto-optic tunable filter (UFBG-AOTF) is applied to select the desired optical sidebands from the output of a differentially driven DD-MZM biased at quadrature point. Adjustment of frequency of the applied acoustic wave on the UFBG leads tunable multiplication factor. Optical band-stop filter is needed to suppress carrier [67]. | i) 2 (20 GHz from 10 GHz)<br>ii) 4 (40 GHz from 10 GHz)<br>iii) 6, 8, 10 (simulated) | i) ESHSR > 15 dB<br>ii) ESHSR > 20 dB |
| Using a directly modulated laser to injection locking the high-order sideband of modulated light with another directly modulated slave laser, frequency multiplication is detected at the slave laser's radio frequency port. Temperature adjustment of the lasers is required for tuning the multiplication factor. No photodetector is necessary [68] | i) 10<br>ii) 12<br>(1 GHz to 10 and 12 GHz respectively) | i) ESHSR > 25 dB<br>Phase noise -82 dBc/Hz at 10 kHz offset<br>ii) ESHSR > 25 dB<br>Phase noise -80.2 dBc/Hz at 10 kHz offset |

| | | |
|---|---|---|
| The modulated light out of the MITP-biased MZM is equally split. One part is undergone a π phase shift; another part is modulated again by the same RF drive at a MATP-biased MZM and combined at polarization combiner after passing through polarization controller. The combined signal is then passed through the linear polarizer. For fixed modulation index to suppress unwanted harmonics and carrier, the tuning at polarizer can be used for controlling OSSR and multiplication factor (Simulated) [69] | 2, 6 (20 GHz and 60 GHz from 10 GHz) | OSSR ~ 50 dB<br>SNR > 35 dB |

# Appendix II. MATLAB Script to Formulate the Argand Diagram

In chapter 2, an Argand diagram is used to characterize the ideal RF specifications by depicting the optical paths graphically which can be utilized to establish the total transmission function of frequency 8-tupling circuit. It is also established that any arbitrary RF drive drift from its ideal value can be represented by the new traces of each optical path. A script written in MATLAB can be utilized to automate the derivation of the Argand diagram of the proposed frequency octupling circuit which can be used to formulate the transmission function. Simple modification of any RF drive specifications in the script is needed to evaluate the effect of deviation in corresponding ideal RF drive conditions quantitatively. This can be utilized to be a simple alternative to cumbersome analytical approach to address such deviation. In this script, two cases are considered: the ideal case where specific RF drive conditions are maintained and a non-ideal case discussed in chapter 2 where RF drive amplitudes and phases are deviated from the ideal condition. The script can generate the Argand diagram where each optical path is depicted by a radius vector whose properties can be utilized to derive the transmission function of the architecture.

```
clear all;
close all;
clc;

phi_matrix=[1 1 1 1; 1 1 1 -1; 1 1 -1 1; 1 1 -1 -1; 1 -1 1 1; 1 -1 1 -1;...
    1 -1 -1 1; 1 -1 -1 -1; -1 1 1 1; -1 1 1 -1; -1 1 -1 1; -1 1 -1 -1;...
    -1 -1 1 1; -1 -1 1 -1; -1 -1 -1 1; -1 -1 -1 -1];
% phi_matrix is used to address the π phase difference between the upper
% and lower arm of a differentially driven MZM. Any deviation in this
% condition can be introduced in this matrix

d2r = @(y) (y*pi/180);
r2d = @(z) (z*180/pi);

Vpi=5;      % typical half-wave voltage of LiNbO3 MZM
Vrf1=3.1;   % Ideal case where all RF drive amplitudes are same
Vrf2=3.1;
Vrf3=3.1;
Vrf4=3.1;

amp1=pi*Vrf1/Vpi;
amp2=pi*Vrf2/Vpi;
amp3=pi*Vrf3/Vpi;
amp4=pi*Vrf4/Vpi;

MZM_1=amp1*exp(j*d2r(0));     % radius vector representing each phase
MZM_2=amp2*exp(j*d2r(45));    % modulator of the corresponding MZM
MZM_3=amp3*exp(j*d2r(90));
MZM_4=amp4*exp(j*d2r(135));

Vpi=5;
Vrf1_1=2.725;   % Non ideal case where RF drive amplitudes are different
Vrf2_2=3.1;
Vrf3_3=3.8;
Vrf4_4=3.1;

amp1_1=pi*Vrf1/Vpi;
amp2_2=pi*Vrf2/Vpi;
amp3_3=pi*Vrf3/Vpi;
amp4_4=pi*Vrf4/Vpi;

rf1=0;        % Non ideal case where RF drive phases are different
rf2=48;
rf3=89.2;
rf4=135;

MZM_1_1=amp1_1*exp(j*d2r(rf1));
MZM_2_2=amp2_2*exp(j*d2r(rf2));
MZM_3_3=amp3_3*exp(j*d2r(rf3));
MZM_4_4=amp4_4*exp(j*d2r(rf4));
```

```
% in the following section, radius vectors representing phase modulators
% are used to define 16 optical paths corresponding the proposed cascaded
% frequency 8-tupling architecture. Their numerical values can be utilized
% directly to calculate the transmission function.
for i=1:1:16

f_1(i,1)=phi_matrix(i,1)*MZM_1+phi_matrix(i,2)*MZM_2+phi_matrix(i,3)*MZM_3+ph
i_matrix(i,4)*MZM_4;

f_2(i,1)=phi_matrix(i,1)*MZM_1_1+phi_matrix(i,2)*MZM_2_2+phi_matrix(i,3)*MZM_
3_3+phi_matrix(i,4)*MZM_4_4;
end

f=[abs(f_1) r2d(angle(f_1)) abs(f_2) r2d(angle(f_2))]
labels=cellstr(num2str([1:16]'));

% The following section plots the Argand diagrams of the ideal and
% non-ideal case
for j=1:1:16

x1=f(j,1)*cosd(f(j,2));
y1=f(j,1)*sind(f(j,2));
x2=f(j,3)*cosd(f(j,4));
y2=f(j,3)*sind(f(j,4));

plot([0,x1],[0,y1],'r');
text(x1,y1,labels(j,1));
axis ([-5 5 -5 5]);
daspect([1 1 1])
hold on;
plot(x1,y1,'r*')
hold on;

plot([0,x2],[0,y2],'k--');
text(x2,y2,labels(j,1));
hold on;
plot(x2,y2,'k*')
hold on;

end
```

**Bibliography**


1. Seeds, Alwyn J., and Keith J. Williams. "Microwave photonics." *Journal of Lightwave Technology* 24, no. 12 (2006): 4628-4641.
2. Wake, David. "Trends and prospects for radio over fibre picocells." In *Proc. MWP*, vol. 2, pp. 21-24. 2002.
3. Hall, Trevor J., Ramón Maldonado-Basilio, Sawsan Abdul-Majid, Joe Seregelyi, Ran Li, Irene Antolín-Pérez, Hamdam Nikkhah et al. "Radio-over-Fibre access for sustainable Digital Cities." *annals of telecommunications-annales des télécommunications* 68, no. 1-2 (2013): 3-21.
4. ITU, "World Telecommunication Development Report: 1999, mobile cellular" https://www.itu.int/ITU-D/ict/publications/wtdr_99/material/wtdr99s.pdf (last accessed March 4, 2020)
5. https://www.itu.int/en/ITU-D/Statistics/Pages/stat/default.aspx (last accessed March 4, 2020)
6. ITU, "Measuring Digital Development- Facts and figures 2019" https://www.itu.int/en/ITU-D/Statistics/Documents/facts/FactsFigures2019.pdf (last accessed March 4, 2020)
7. https://www.speedtest.net/reports/canada/#mobile (last accessed March 4, 2020)
8. https://en.wikipedia.org/wiki/GSM (last accessed March 4, 2020)
9. https://en.wikipedia.org/wiki/UMTS (last accessed March 4, 2020)
10. Deng, Der-Jiunn, Kwang-Cheng Chen, and Rung-Shiang Cheng. "IEEE 802.11 ax: Next generation wireless local area networks." In *10Th international conference on heterogeneous networking for quality, reliability, security and robustness*, pp. 77-82. IEEE, 2014.
11. https://en.wikipedia.org/wiki/LTE_(telecommunication) (last accessed March 4, 2020)
12. Kim, Choul-Young, Dong-Woo Kang, and Gabriel M. Rebeiz. "A 44–46-GHz 16-element SiGe BiCMOS high-linearity transmit/receive phased array." *IEEE transactions on microwave theory and techniques* 60, no. 3 (2012): 730-742.
13. Jayamon, Jefy, Ozan Gurbuz, Bassel Hanafi, Amir Agah, James Buckwalter, Gabriel Rebeiz, and Peter Asbeck. "Spatially power-combined W-band power amplifier using stacked CMOS." In *2014 IEEE Radio Frequency Integrated Circuits Symposium*, pp. 151-154. IEEE, 2014.
14. Babakhani, Aydin, Xiang Guan, Abbas Komijani, Arun Natarajan, and Ali Hajimiri. "A 77-GHz phased-array transceiver with on-chip antennas in silicon: Receiver and antennas." *IEEE Journal of Solid-State Circuits* 41, no. 12 (2006): 2795-2806.
15. Natarajan, Arun, Scott K. Reynolds, Ming-Da Tsai, Sean T. Nicolson, Jing-Hong Conan Zhan, Dong Gun Kam, Duixian Liu, Yen-Lin Oscar Huang, Alberto Valdes-Garcia, and Brian A. Floyd. "A fully-integrated 16-element phased-array receiver in SiGe BiCMOS for 60-GHz communications." *IEEE Journal of Solid-State Circuits* 46, no. 5 (2011): 1059-1075.

16. Lee, Woosung, Jaeheung Kim, Choon Sik Cho, and Young Joong Yoon. "Beamforming lens antenna on a high resistivity silicon wafer for 60 GHz WPAN." *IEEE Transactions on Antennas and Propagation* 58, no. 3 (2009): 706-713.
17. Kabonzo, Fabrice Mfuamba, and Muhammad Umar Dilshad. "Impact of radio over fiber technology for integrated 5G front and back-haul applications." In *2017 IEEE 2nd Advanced Information Technology, Electronic and Automation Control Conference (IAEAC)*, pp. 1077-1081. IEEE, 2017.
18. Federici, John, and Lothar Moeller. "Review of terahertz and subterahertz wireless communications." *Journal of Applied Physics* 107, no. 11 (2010): 6.
19. Wells, Jonathan. "Faster than fiber: The future of multi-G/s wireless." *IEEE microwave magazine* 10, no. 3 (2009): 104-112.
20. Baack, C., G. Elze, G. Großkopf, F. Kraus, W. Krick, and L. Küller. "Analogue optical transmission of 26 TV channels." *Electronics Letters* 15, no. 10 (1979): 300-301.
21. Gundner, H. M., R. Stannard, and U. Scholz. "Optical fiber CATV distribution system for 12 TV and 12 FM stereo radio channels." In *Proc. ECOC83*, pp. 559-563. 1983.
22. Way, Winston I. "Subcarrier multiplexed lightwave system design considerations for subscriber loop applications." *Journal of Lightwave Technology* 7, no. 11 (1989): 1806-1818.
23. Alavi, S. E., M. R. K. Soltanian, I. S. Amiri, M. Khalily, A. S. M. Supa'At, and Harith Ahmad. "Towards 5G: A photonic based millimeter wave signal generation for applying in 5G access fronthaul." *Scientific reports* 6, no. 1 (2016): 1-11.
24. Chen, Xiang, and Jianping Yao. "A high spectral efficiency coherent rof system based on OSSB modulation with low-cost free-running laser sources for UDWDM-PONs." *Journal of Lightwave Technology* 34, no. 11 (2016): 2789-2795.
25. Hirooka, Toshihiko, Masato Yoshida, Keisuke Kasai, and Masataka Nakazawa. "Optical and wireless-integrated next-generation access network based on coherent technologies." In *Broadband Access Communication Technologies X*, vol. 9772, p. 977203. International Society for Optics and Photonics, 2016.
26. Kawanishi, Satoki, Atsushi Takada, and Masatoshi Saruwatari. "Wideband frequency-response measurement of optical receivers using optical heterodyne detection." *Journal of lightwave technology* 7, no. 1 (1989): 92-98.
27. Phelan, P., Gerald Farrell, and Joe Hegarty. "All-optical synchronization and multiplication of the frequency of mode-locked signals." *IEEE photonics technology letters* 4, no. 12 (1992): 1332-1335.
28. Rideout, Howard R., Joe S. Seregelyi, and Jianping Yao. "A true time delay beamforming system incorporating a wavelength tunable optical phase-lock loop." *Journal of lightwave technology* 25, no. 7 (2007): 1761-1770.
29. Ramos, R. T., and A. J. Seeds. "Fast heterodyne optical phase-lock loop using double quantum well laser diodes." *Electronics letters* 28, no. 1 (1992): 82-83.

30. Gliese, U., Torben Nørskov Nielsen, Marlene Bruun, E. Lintz Christensen, K. E. Stubkjaer, S. Lindgren, and B. Broberg. "A wideband heterodyne optical phase-locked loop for generation of 3-18 GHz microwave carriers." *IEEE Photonics Technology Letters* 4, no. 8 (1992): 936-938.
31. Laperle, Charles, Mikelis Svilans, Maxime Poirier, and Michel Tetu. "Frequency multiplication of microwave signals by sideband optical injection locking using a monolithic dual-wavelength DFB laser device." *IEEE Transactions on Microwave Theory and Techniques* 47, no. 7 (1999): 1219-1224.
32. Wake, David, Claudio R. Lima, and Phillip A. Davies. "Optical generation of millimeter-wave signals for fiber-radio systems using a dual-mode DFB semiconductor laser." *IEEE Transactions on microwave Theory and Techniques* 43, no. 9 (1995): 2270-2276.
33. Pozzi, Francesca, M. Richard, and Marc Sorel. "Dual-wavelength InAlGaAs–InP laterally coupled distributed feedback laser." *IEEE photonics technology letters* 18, no. 24 (2006): 2563-2565.
34. O'reilly, J. J., P. M. Lane, Rolf Heidemann, and Rolf Hofstetter. "Optical generation of very narrow linewidth millimetre wave signals." *Electronics Letters* 28, no. 25 (1992): 2309-2311.
35. Qi, Guohua, Jianping Yao, Joe Seregelyi, Stephane Paquet, and Claude Belisle. "Generation and distribution of a wide-band continuously tunable millimeter-wave signal with an optical external modulation technique." *IEEE Transactions on microwave theory and techniques* 53, no. 10 (2005): 3090-3097.
36. Chien, Hung-Chang, Yu-Ting Hsueh, Arshad Chowdhury, Jianjun Yu, and Gee-Kung Chang. "On frequency-doubled optical millimeter-wave generation technique without carrier suppression for in-building wireless over fiber applications." *IEEE Photonics Technology Letters* 22, no. 3 (2010): 182-184.
37. Liu, Shifeng, Dan Zhu, Zhengwu Wei, and Shilong Pan. "Photonic generation of widely tunable phase-coded microwave signals based on a dual-parallel polarization modulator." *Optics letters* 39, no. 13 (2014): 3958-3961.
38. Lin, Chun-Ting, Po-Tsung Shih, Jason Chen, Wen-Qiang Xue, Peng-Chun Peng, and Sien Chi. "Optical millimeter-wave signal generation using frequency quadrupling technique and no optical filtering." *IEEE Photonics Technology Letters* 20, no. 12 (2008): 1027-1029.
39. Yu, Song, Wanyi Gu, Aiying Yang, Tao Jiang, and Chonggang Wang. "A frequency quadrupling optical mm-wave generation for hybrid fiber-wireless systems." *IEEE Journal on selected areas in Communications* 31, no. 12 (2013): 797-803.
40. Liu, Weilin, Muguang Wang, and Jianping Yao. "Tunable microwave and sub-terahertz generation based on frequency quadrupling using a single polarization modulator." *Journal of lightwave technology* 31, no. 10 (2013): 1636-1644.

41. Thakur, Manoj P., Maria CR Medeiros, Paula Laurêncio, and John E. Mitchell. "Optical frequency tripling with improved suppression and sideband selection." *Optics express* 19, no. 26 (2011): B459-B470.
42. Mohamed, Mohmoud, Xiupu Zhang, Bouchaib Hraimel, and Ke Wu. "Frequency sixupler for millimeter-wave over fiber systems." *Optics Express* 16, no. 14 (2008): 10141-10151.
43. Wiberg, Andreas, Pere Pérez-Millán, Miguel V. Andrés, and Per Olof Hedekvist. "Microwave-photonic frequency multiplication utilizing optical four-wave mixing and fiber Bragg gratings." *Journal of lightwave technology* 24, no. 1 (2006): 329.
44. Zhang, Jian, Hongwei Chen, Minghua Chen, Tianliang Wang, and Shizhong Xie. "Photonic generation of a millimeter-wave signal based on sextuple-frequency multiplication." *Optics letters* 32, no. 9 (2007): 1020-1022.
45. Zhu, Zihang, Shanghong Zhao, Xuan Li, Kun Qu, and Tao Lin. "Photonic generation of frequency-sextupled microwave signal based on dual-polarization modulation without an optical filter." *Optics & Laser Technology* 87 (2017): 1-6.
46. Lin, Chun-Ting, Po-Tsung Shih, Wen-Jr Jiang, Jason Jyehong Chen, Peng-Chun Peng, and Sien Chi. "A continuously tunable and filterless optical millimeter-wave generation via frequency octupling." *Optics express* 17, no. 22 (2009): 19749-19756.
47. Zhu, Zihang, Shanghong Zhao, Xuan Li, Kun Qu, and Tao Lin. "Photonic generation of frequency-octupled and frequency-quadrupled microwave signals using a dual-parallel polarization modulator." *Optical and Quantum Electronics* 48, no. 8 (2016): 398.
48. Zhang, Yamei, Fangzheng Zhang, and Shilong Pan. "Generation of frequency-multiplied and phase-coded signal using an optical polarization division multiplexing modulator." *IEEE Transactions on Microwave Theory and Techniques* 65, no. 2 (2016): 651-660.
49. Zhang, Wu, Aijun Wen, Yongsheng Gao, Hanxiao Zheng, Wei Chen, and Hongye He. "A simplified filterless photonic frequency octupling scheme based on cascaded modulators." *Journal of Modern Optics* 64, no. 8 (2017): 861-865.
50. Qin, Yi, Junqiang Sun, Mingdi Du, and Jianfei Liao. "Simplified optical millimeter-wave generation configuration based on frequency octupling." *Optics Communications* 315 (2014): 280-285.
51. Gao, Yongsheng, Aijun Wen, Ningning Li, Xiaohui Wu, and Huixing Zhang. "Microwave generation with photonic frequency octupling using a DPMZM in a Sagnac loop." *Journal of Modern Optics* 62, no. 16 (2015): 1291-1296.
52. Zhu, Zihang, Shanghong Zhao, Qinggui Tan, Dong Liang, Xuan Li, and Kun Qu. "Photonically assisted microwave signal generation based on two cascaded polarization modulators with a tunable multiplication factor." *IEEE Transactions on Microwave Theory and Techniques* 64, no. 11 (2016): 3748-3756.

53. Li, Wangzhe, and Jianping Yao. "Microwave generation based on optical domain microwave frequency octupling." *IEEE photonics technology letters* 22, no. 1 (2009): 24-26.
54. Zhang, Wu, Aijun Wen, Yongsheng Gao, Shuo Shang, Hanxiao Zheng, and Hongye He. "Filterless frequency-octupling mm-wave generation by cascading Sagnac loop and DPMZM." *Optics & Laser Technology* 97 (2017): 229-233.
55. Gao, Yongsheng, Aijun Wen, Wei Jiang, Dong Liang, Wenya Liu, and Shuiying Xiang. "Photonic microwave generation with frequency octupling based on a DP-QPSK modulator." *IEEE Photonics Technology Letters* 27, no. 21 (2015): 2260-2263.
56. Ma, Jianxin, Xiangjun Xin, J. Yu, Chongxiu Yu, Kuiru Wang, Huiying Huang, and Lan Rao. "Optical millimeter wave generated by octupling the frequency of the local oscillator." *Journal of Optical Networking* 7, no. 10 (2008): 837-845.
57. Hasan, Mehedi, and Trevor J. Hall. "A photonic frequency octo-tupler with reduced RF drive power and extended spurious sideband suppression." *Optics & Laser Technology* 81 (2016): 115-121.
58. Hasan, Mehedi, Rabiaa Guemri, Ramón Maldonado-Basilio, Frédéric Lucarz, and Trevor Hall. "Theoretical analysis and modeling of a photonic integrated circuit for frequency 8-tupled and 24-tupled millimeter wave signal generation." *Optics letters* 39, no. 24 (2014): 6950-6953.
59. Hasan, Gazi Mahamud, Mehedi Hasan, Hongpeng Shang, DeGui Sun, Karin Hinzer, Peng Liu, and Trevor Hall. "Energy efficient photonic millimeter-wave generation using cascaded polarization modulators." *Optical and Quantum Electronics* 51, no. 7 (2019): 217.
60. Vidal, B. "Photonic millimeter-wave frequency multiplication based on cascaded four-wave mixing and polarization pulling." *Optics letters* 37, no. 24 (2012): 5055-5057.
61. Shih, Po-Tsung, Jason Chen, Chun-Ting Lin, Wen-Jr Jiang, Han-Sheng Huang, Peng-Chun Peng, and Sien Chi. "Optical millimeter-wave signal generation via frequency 12-tupling." *Journal of Lightwave Technology* 28, no. 1 (2009): 71-78.
62. Kanno, Atsushi, and Tetsuya Kawanishi. "Millimeter-wave signal generation using cascaded optical frequency multiplication technique." In *2014 44th European Microwave Conference*, pp. 1028-1031. IEEE, 2014.
63. Zhu, Zihang, Shanghong Zhao, Xingchun Chu, and Yi Dong. "Optical generation of millimeter-wave signals via frequency 16-tupling without an optical filter." *Optics Communications* 354 (2015): 40-47.
64. Chen, Xiaogang, Lu Xia, and Dexiu Huang. "A filterless 24-tupling optical millimeter-wave generation and RoF distribution." *Optik* 147 (2017): 22-26.
65. Zhu, Huatao, Rong Wang, Peng Xiang, Tao Pu, Tao Fang, Jilin Zheng, and Yuandong Li. "A novel approach to photonic generate microwave signals based on optical injection locking and four-wave mixing." *Optics Communications* 400 (2017): 101-105.

66. Zhang, Huizhong, Ze Dong, Xinxing Wu, and Kaiming Zhang. "Generation of frequency-eightfold millimeter-wave with optical carrier suppression by using one single-drive modulator." In *2017 International Symposium on Intelligent Signal Processing and Communication Systems (ISPACS)*, pp. 353-356. IEEE, 2017.
67. Wang, Yiqun, Li Pei, Jing Li, and Yueqin Li. "Millimeter-wave signal generation with tunable frequency multiplication factor by employing UFBG-based acousto-optic tunable filter." *IEEE Photonics Journal* 9, no. 1 (2017): 1-10.
68. Wang, Shuaishuai, Ju Wang, Tianyu Li, Chuang Ma, Tianyuan Xie, Yang Yu, and Jinlong Yu. "A Tunable Microwave Frequency Multiplication System Based on Injection Locking without Photodetector." In *2018 Conference on Lasers and Electro-Optics Pacific Rim (CLEO-PR)*, pp. 1-2. IEEE, 2018.
69. Chen, Hongyao, Tigang Ning, Jing Li, Li Pei, Jin Yuan, Jingjing Zheng, and Ling Liu. "Optical millimeter-wave generation with tunable multiplication factors and reduced power fluctuation by using cascaded modulators." *Optics & Laser Technology* 103 (2018): 206-211.
70. Dorrington, Adrian A., and Rainer Kuennemeyer. "Single sideband techniques for laser Doppler velocimeter frequency offset." *Optical Engineering* 42, no. 11 (2003): 3239-3247.
71. Li, Yanlu, Stijn Meersman, and Roel Baets. "Optical frequency shifter on SOI using thermo-optic serrodyne modulation." In *7th IEEE International Conference on Group IV Photonics*, pp. 75-77. IEEE, 2010.
72. Li, Jianping, and Zhaohui Li. "Frequency-locked multicarrier generator based on a complementary frequency shifter with double recirculating frequency-shifting loops." *Optics letters* 38, no. 3 (2013): 359-361.
73. Li, Jianping, Xuebing Zhang, Zhaohui Li, Xiaoguang Zhang, Guifang Li, and Chao Lu. "Theoretical studies on the polarization-modulator-based single-side-band modulator used for generation of optical multicarrier." *Optics express* 22, no. 12 (2014): 14087-14095.
74. Kowalski, F. V., P. D. Hale, and S. J. Shattil. "Broadband continuous-wave laser." *Optics letters* 13, no. 8 (1988): 622-624.
75. Frankel, Michael Y., R. D. Esman, and M. G. Parent. "Array transmitter/receiver controlled by a true time-delay fiber-optic beamformer." *IEEE Photonics Technology Letters* 7, no. 10 (1995): 1216-1218.
76. Cygan, Agata, Daniel Lisak, Piotr Morzyński, Marcin Bober, Michał Zawada, Eugeniusz Pazderski, and Roman Ciuryło. "Cavity mode-width spectroscopy with widely tunable ultra narrow laser." *Optics express* 21, no. 24 (2013): 29744-29754.
77. Tanabe, Takasumi, M. Notomi, and E. Kuramochi. "Measurement of ultra-high-Q photonic crystal nanocavity using single-sideband frequency modulator." *Electronics letters* 43, no. 3 (2007): 187-188.

78. Shagam, Richard N., and James C. Wyant. "Optical frequency shifter for heterodyne interferometers using multiple rotating polarization retarders." *Applied optics* 17, no. 19 (1978): 3034-3035.
79. Nosu, K., S. C. Rashleigh, H. F. Taylor, and J. F. Weller. "Acousto-optic frequency shifter for single-mode fibres." *Electronics Letters* 19, no. 20 (1983): 816-818.
80. Cummins, H. Z., and N. Knable. "Single sideband modulation of coherent light by Bragg reflection from acoustical waves." *Proceedings of the IEEE* 51, no. 9 (1963): 1246-1246.
81. Izutsu, Masayuki, Shinsuke Shikama, and Tadasi Sueta. "Integrated optical SSB modulator/frequency shifter." *IEEE Journal of Quantum Electronics* 17, no. 11 (1981): 2225-2227.
82. Hui, Rongqing, Benyuan Zhu, Renxiang Huang, Christopher T. Allen, Kenneth R. Demarest, and Douglas Richards. "Subcarrier multiplexing for high-speed optical transmission." *Journal of lightwave technology* 20, no. 3 (2002): 417.
83. Frankel, Michael Y., and Ronald D. Esman. "Optical single-sideband suppressed-carrier modulator for wide-band signal processing." *Journal of lightwave technology* 16, no. 5 (1998): 859.
84. Xiao, Shijun, and Andrew M. Weiner. "Optical carrier-suppressed single sideband (O-CS-SSB) modulation using a hyperfine blocking filter based on a virtually imaged phased-array (VIPA)." *IEEE photonics technology letters* 17, no. 7 (2005): 1522-1524.
85. Zibar, Darko, Rakesh Sambaraju, Antonio Caballero Jambrina, Ruben Alemany, Javier Herrera, and Idelfonso Tafur Monroy. "16 Gb/s QPSK Wireless-over-Fibre link in 75–110GHz band employing optical heterodyne generation and coherent detection." In *36th European Conference and Exhibition on Optical Communication*, pp. 1-3. IEEE, 2010.
86. Shimotsu, S., S. Oikawa, T. Saitou, N. Mitsugi, K. Kubodera, T. Kawanishi, and M. Izutsu. "Single side-band modulation performance of a LiNbO 3 integrated modulator consisting of four-phase modulator waveguides." *IEEE Photonics Technology Letters* 13, no. 4 (2001): 364-366.
87. Yamaguchi, Yuya, Atsushi Kanno, Tetsuya Kawanishi, Masayuki Izutsu, and Hirochika Nakajima. "Pure single-sideband modulation using high extinction-ratio parallel Mach-Zehnder modulator with third-order harmonics superposition technique." In *2015 Conference on Lasers and Electro-Optics (CLEO)*, pp. 1-2. IEEE, 2015.
88. Yu, Jianjun, Zhensheng Jia, Lilin Yi, Yikai Su, Gee-Kung Chang, and Ting Wang. "Optical millimeter-wave generation or up-conversion using external modulators." *IEEE Photonics technology letters* 18, no. 1 (2005): 265-267.
89. Chow, C. W., C. H. Wang, C. H. Yeh, and S. Chi. "Analysis of the carrier-suppressed single-sideband modulators used to mitigate Rayleigh backscattering in carrier-distributed PON." *Optics express* 19, no. 11 (2011): 10973-10978.
90. Lauermann, Matthias, Claudius Weimann, A. Knopf, Wolfgang Heni, Robert Palmer, Sebastian Koeber, Delwin L. Elder et al. "Integrated optical frequency shifter in silicon-organic hybrid (SOH) technology." *Optics express* 24, no. 11 (2016): 11694-11707.

91. Kodigala, A., M. Gehl, C. T. DeRose, D. Hood, A. T. Pomerene, C. Dallo, D. Trotter et al. "Silicon Photonic Single-Sideband Generation with Dual-Parallel Mach-Zehnder Modulators." In *2019 Conference on Lasers and Electro-Optics (CLEO)*, pp. 1-2. IEEE, 2019.
92. Heismann, F., and R. Ulrich. "Integrated-optical frequency translator with stripe waveguide." *Applied physics letters* 45, no. 5 (1984): 490-492.
93. Johnson, Leonard M., and Ch H. Cox. "Serrodyne optical frequency translation with high sideband suppression." *Journal of lightwave technology* 6, no. 1 (1988): 109-112.
94. Li, Yanlu, Stijn Meersman, and Roel Baets. "Optical frequency shifter on SOI using thermo-optic serrodyne modulation." In *7th IEEE International Conference on Group IV Photonics*, pp. 75-77. IEEE, 2010.
95. Barretto, Elaine CS, and Jørn M. Hvam. "Photonic integrated single-sideband modulator/frequency shifter based on surface acoustic waves." In *Silicon photonics and photonic integrated circuits II*, vol. 7719, p. 771920. International Society for Optics and Photonics, 2010.
96. Fan, Guofang, Yuan Li, Chunguang Hu, Lihua Lei, Dong Zhao, Hongyu Li, and Zhen Zhen. "A novel concept of acousto-optic ring frequency shifters on silicon-on-insulator technology." *Optics & Laser Technology* 63 (2014): 62-65.
97. Shen, Yichun, Xianmin Zhang, and Kangsheng Chen. "Optical single sideband modulation of 11-GHz RoF system using stimulated Brillouin scattering." *IEEE photonics technology letters* 17, no. 6 (2005): 1277-1279.
98. Sharma, Gourav Prateek, Stefan Preußler, and Thomas Schneider. "Precise optical frequency shifting using stimulated Brillouin scattering in optical Fibers." *IEEE Photonics Technology Letters* 29, no. 17 (2017): 1467-1470.
99. Georges, J. B., J. Park, O. Solgaard, P. Pepeljugoski, M. Sayed, and K. Y. Lau. "Transmission of 300 Mbit/s BPSK at 39 GHz using feedforward optical modulation." *Electronics Letters* 30, no. 2 (1994): 160-161.
100. Braun, R-P., G. Grosskopf, D. Rohde, and F. Schmidt. "Low-phase-noise millimeter-wave generation at 64 GHz and data transmission using optical sideband injection locking." *IEEE Photonics Technology Letters* 10, no. 5 (1998): 728-730.
101. Onodera, N., A. J. Lowery, L. Zhai, Z. Ahmed, and R. S. Tucker. "Frequency multiplication in actively mode-locked semiconductor lasers." *Applied physics letters* 62, no. 12 (1993): 1329-1331.
102. Vallejo, Luis, Beatriz Ortega, Jan Bohata, Stanislav Zvanovec, and Vicenç Almenar. "Experimental Photonic 40–90 GHz Millimetre-Wave Signal Generation and 10 Gb/s 32-QAM Signal Transmission over Hybrid Fiber/FSO 5G Networks." In *2019 21st International Conference on Transparent Optical Networks (ICTON)*, pp. 1-4. IEEE, 2019.
103. Maldonado-Basilio, Ramón, Mehedi Hasan, Rabiaa Guemri, Frédéric Lucarz, and Trevor J. Hall. "Generalized Mach–Zehnder interferometer architectures for radio frequency

translation and multiplication: suppression of unwanted harmonics by design." *Optics Communications* 354 (2015): 122-127.

104. Baskaran, M., and R. Prabakaran. "Optical millimeter wave signal generation with frequency 16-tupling using cascaded MZMs and no optical filtering for radio over fiber system." *Journal of the European Optical Society-Rapid Publications* 14, no. 1 (2018): 13.
105. Dogru, Selim, and Nadir Dagli. "0.77-V drive voltage electro-optic modulator with bandwidth exceeding 67 GHz." *Optics letters* 39, no. 20 (2014): 6074-6077.
106. Zhu, S., Li, M., Wang, X., Zhu, N.H. and Li, W., 2019. 1× N hybrid radio frequency photonic splitter based on a dual-polarization dual-parallel Mach Zehnder modulator. *Optics Communications*, *431*, pp.10-13.
107. Porzi, Claudio, Giovanni Serafino, Marc Sans, Fabio Falconi, Vito Sorianello, Sergio Pinna, John E. Mitchell, Marco Romagnoli, Antonella Bogoni, and Paolo Ghelfi. "Photonic integrated microwave phase shifter up to the mm-wave band with fast response time in silicon-on-insulator technology." *Journal of Lightwave Technology* 36, no. 19 (2018): 4494-4500.
108. Kiuchi, Hitoshi, Tetsuya Kawanishi, Masumi Yamada, Takahide Sakamoto, Masahiro Tsuchiya, Jun Amagai, and Masayuki Izutsu. "High extinction ratio Mach–Zehnder modulator applied to a highly stable optical signal generator." *IEEE Transactions on Microwave Theory and Techniques* 55, no. 9 (2007): 1964-1972.
109. Hasan, Mehedi, Ramón Maldonado-Basilio, and Trevor J. Hall. "Dual-function photonic integrated circuit for frequency octo-tupling or single-side-band modulation." *Optics letters* 40, no. 11 (2015): 2501-2504.
110. Carolan, Jacques, Christopher Harrold, Chris Sparrow, Enrique Martín-López, Nicholas J. Russell, Joshua W. Silverstone, Peter J. Shadbolt et al. "Universal linear optics." *Science* 349, no. 6249 (2015): 711-716.
111. Miller, David AB. "Perfect optics with imperfect components." *Optica* 2, no. 8 (2015): 747-750.
112. Rabiei, Payam, Jichi Ma, Saeed Khan, Jeff Chiles, and Sasan Fathpour. "Heterogeneous lithium niobate photonics on silicon substrates." *Optics express* 21, no. 21 (2013): 25573-25581.
113. Dong, Po, Xiang Liu, S. Chandrasekhar, Lawrence L. Buhl, Ricardo Aroca, and Young-Kai Chen. "Monolithic silicon photonic integrated circuits for compact $100^{+}$ Gb/s coherent optical receivers and transmitters." *IEEE Journal of Selected Topics in Quantum Electronics* 20, no. 4 (2014): 150-157.
114. Pernice, Wolfram HP, Chi Xiong, Fred J. Walker, and Hong X. Tang. "Design of a silicon integrated electro-optic modulator using ferroelectric BaTiO 3 films." *IEEE Photonics Technology Letters* 26, no. 13 (2014): 1344-1347.
115. Hasan, Gazi Mahamud, Mehedi Hasan, Karin Hinzer, and Trevor Hall. "Optical frequency multiplication technique using cascaded modulator to achieve RF power

advantage." In *2019 International Conference on Numerical Simulation of Optoelectronic Devices (NUSOD)*, pp. 125-126. IEEE, 2019.

116. Jung, Thomas, Ji-Lin Shen, Dennis TK Tong, Sanjeev Murthy, Ming C. Wu, T. Tanbun-Ek, Wenshen Wang et al. "CW injection locking of a mode-locked semiconductor laser as a local oscillator comb for channelizing broad-band RF signals." *IEEE transactions on microwave theory and techniques* 47, no. 7 (1999): 1225-1233.
117. Li, Wei, Ning Hua Zhu, and Li Xian Wang. "Harmonic RF carrier generation and broadband data upconversion using stimulated Brillouin scattering." *Optics Communications* 284, no. 13 (2011): 3437-3439.
118. Bull, Jeffrey D., Nicolas AF Jaeger, Hiroshi Kato, Mark Fairburn, Adam Reid, and Pejman Ghanipour. "40-GHz electro-optic polarization modulator for fiber optic communications systems." In *Photonics North 2004: Optical Components and Devices*, vol. 5577, pp. 133-143. International Society for Optics and Photonics, 2004.
119. Hasan, Gazi Mahamud, Mehedi Hasan, Karin Hinzer, and Trevor Hall. "Filterless frequency octupling circuit using dual stage cascaded polarization modulators." *Journal of Modern Optics* 66, no. 4 (2019): 455-461.
120. Kawabata, Yuto, Masaru Zaitsu, Takuo Tanemura, and Yoshiaki Nakano. "Proposal and experimental demonstration of monolithic InP/InGaAsP polarization modulator." In *2014 The European Conference on Optical Communication (ECOC)*, pp. 1-3. IEEE, 2014.
121. Marpaung, David, Chris Roeloffzen, René Heideman, Arne Leinse, Salvador Sales, and José Capmany. "Integrated microwave photonics." *Laser & Photonics Reviews* 7, no. 4 (2013): 506-538.
122. Kazovsky, Leonid G., Wei-Tao Shaw, David Gutierrez, Ning Cheng, and Shing-Wa Wong. "Next-generation optical access networks." *Journal of lightwave technology* 25, no. 11 (2007): 3428-3442.
123. Gaudino, Roberto, Daniel Cárdenas, Martial Bellec, Benoît Charbonnier, Noëlla Evanno, Philippe Guignard, Sylvain Meyer, Anna Pizzinat, Ingo Mollers, and Dieter Jager. "Perspective in next-generation home networks: Toward optical solutions?." *IEEE Communications Magazine* 48, no. 2 (2010): 39-47.
124. Cox, Charles H., Edward I. Ackerman, Gary E. Betts, and Joelle L. Prince. "Limits on the performance of RF-over-fiber links and their impact on device design." *IEEE Transactions on Microwave Theory and Techniques* 54, no. 2 (2006): 906-920.
125. Decena, Bernalyn, Marc Rosales, and Paul Jason Co. "Characterization of Low Cost Wideband Direct Modulation Radio over Fiber Link." In *2019 International Symposium on Multimedia and Communication Technology (ISMAC)*, pp. 1-5. IEEE, 2019.
126. Kim, Cheolhwan, Inwoong Kim, Guifang Li, Michael R. Lange, Timothy E. Dimmick, Patrick Langlois, and Benoit Reid. "Optical microwave/millimeter-wave links using direct modulation of two-section gain-coupled DFB lasers." *IEEE photonics technology letters* 17, no. 8 (2005): 1734-1736.

127. Li, Yifei, Maja Bystrom, David Yoo, Samuel M. Goldwasser, and Peter R. Herczfeld. "Coherent optical vector modulation for fiber radio using electrooptic microchip lasers." *IEEE transactions on microwave theory and techniques* 53, no. 10 (2005): 3121-3129.
128. Doi, Yoshiyuki, Seiji Fukushima, Tetsuichiro Ohno, and Kaoru Yoshino. "Frequency stabilization of millimeter-wave subcarrier using laser heterodyne source and optical delay line." *IEEE Photonics Technology Letters* 13, no. 9 (2001): 1002-1004.
129. Kuri, Toshiaki, and K-I. Kitayama. "Long-term stabilized millimeter-wave generation using a high-power mode-locked laser diode module." *IEEE transactions on microwave theory and techniques* 47, no. 5 (1999): 570-574.
130. Inoue, Kyo, Norio Takato, Hiromu Toba, and Masao Kawachi. "A four-channel optical waveguide multi/demultiplexer for 5-GHz spaced optical FDM transmission." *Journal of lightwave technology* 6, no. 2 (1988): 339-345.
131. Toda, Hiroyuki, Tsukasa Yamashita, Toshiaki Kuri, and Ken-ichi Kitayama. "Demultiplexing using an arrayed-waveguide grating for frequency-interleaved DWDM millimeter-wave radio-on-fiber systems." *Journal of lightwave technology* 21, no. 8 (2003): 1735-1741.
132. Yamazaki, Hiroshi, Takashi Saida, Takashi Goh, Atsushi Mori, and Shinji Mino. "Dual-carrier IQ modulator with a complementary frequency shifter." *Optics express* 19, no. 26 (2011): B69-B74.
133. Yamazaki, Hiroshi, Takashi Saida, Takashi Goh, Shinji Mino, Munehiko Nagatani, Hideyuki Nosaka, and Koichi Murata. "Dual-carrier dual-polarization IQ modulator using a complementary frequency shifter." *IEEE Journal of Selected Topics in Quantum Electronics* 19, no. 6 (2013): 175-182.
134. Hasan, Mehedi, and Trevor J. Hall. "Photonic circuit for high order USB and LSB separation for remote heterodyning: analysis and simulation." *Optics express* 23, no. 19 (2015): 25259-25271.
135. Hasan, Mehedi, Jianqi Hu, Hamdam Nikkhah, and Trevor Hall. "A photonic circuit for complementary frequency shifting, in-phase quadrature/single sideband modulation and frequency multiplication: analysis and integration feasibility." *Journal of Modern Optics* 64, no. 14 (2017): 1386-1397.
136. Maldonado-Basilio, Ramón, Mehedi Hasan, Hamdam Nikkhah, Sawsan Abdul-Majid, Rabiaa Guemri, Frédéric Lucarz, Jean-Louis de Bougrenet de la Tocnaye, and Trevor James Hall. "Electro-optic up-conversion mixer amenable to photonic integration." *Journal of Modern Optics* 62, no. 17 (2015): 1405-1411.
137. Maldonado-Basilio, Ramón, Neda Nabavi, Kaveleen Aulakh, Mehedi Hasan, and Trevor J. Hall. "Photonic integrated circuit for millimeter-wave signal generation by frequency multiplication." In *2015 IEEE Photonics Conference (IPC)*, pp. 130-131. IEEE, 2015.
138. Wooten, Ed L., Karl M. Kissa, Alfredo Yi-Yan, Edmond J. Murphy, Donald A. Lafaw, Peter F. Hallemeier, David Maack et al. "A review of lithium niobate modulators for

fiber-optic communications systems." *IEEE Journal of selected topics in Quantum Electronics* 6, no. 1 (2000): 69-82.

139. Mercante, Andrew J., Peng Yao, Shouyuan Shi, Garrett Schneider, Janusz Murakowski, and Dennis W. Prather. "110 GHz CMOS compatible thin film LiNbO3 modulator on silicon." *Optics express* 24, no. 14 (2016): 15590-15595.
140. Yu, Yichuan, Robert Lewén, Stefan Irmscher, Urban Westergren, Lars Thylén, Urban Eriksson, and W. S. Lee. "80 Gb/s ETDM transmitter with a traveling-wave electroabsorption modulator." In *OFC/NFOEC Technical Digest. Optical Fiber Communication Conference, 2005.*, vol. 3, pp. 3-pp. IEEE, 2005.
141. Ogiso, Y., J. Ozaki, N. Kashio, N. Kikuchi, H. Tanobe, Y. Ohiso, and M. Kohtoku. "100 Gb/s and 2 V Vπ InP Mach-Zehnder modulator with an nipn heterostructure." *Electronics Letters* 52, no. 22 (2016): 1866-1867.
142. Alloatti, L., D. Korn, R. Palmer, D. Hillerkuss, J. Li, A. Barklund, R. Dinu et al. "42.7 Gbit/s electro-optic modulator in silicon technology." *Optics express* 19, no. 12 (2011): 11841-11851.
143. Wolf, Stefan, Heiner Zwickel, Wladislaw Hartmann, Matthias Lauermann, Yasar Kutuvantavida, Clemens Kieninger, Lars Altenhain et al. "Silicon-organic hybrid (SOH) Mach-Zehnder modulators for 100 Gbit/s on-off keying." *Scientific reports* 8, no. 1 (2018): 1-13.
144. Srinivasan, Srinivasan Ashwyn, Marianna Pantouvaki, Shashank Gupta, Hong Tao Chen, Peter Verheyen, Guy Lepage, Gunther Roelkens et al. "56 Gb/s germanium waveguide electro-absorption modulator." *Journal of Lightwave Technology* 34, no. 2 (2015): 419-424.
145. Roth, J.E., Fidaner, O., Schaevitz, R.K., Kuo, Y.H., Kamins, T.I., Harris, J.S. and Miller, D.A., 2007. Optical modulator on silicon employing germanium quantum wells. *Optics Express*, *15*(9), pp.5851-5859.
146. Ya-Ming, Li, Hu Wei-Xuan, Cheng Bu-Wen, Liu Zhi, and Wang Qi-Ming. "Remarkable Franz-Keldysh Effect in Ge-on-Si pin Diodes." *Chinese Physics Letters* 29, no. 3 (2012): 034205.
147. Feng, Dazeng, Wei Qian, Hong Liang, Cheng-Chih Kung, Zhou Zhou, Zhi Li, Jacob S. Levy et al. "High-speed GeSi electroabsorption modulator on the SOI waveguide platform." *IEEE Journal of Selected Topics in Quantum Electronics* 19, no. 6 (2013): 64-73.
148. Srinivasan, S. A., Peter Verheyen, Roger Loo, Ingrid De Wolf, Marianna Pantouvaki, Guy Lepage, Sadhishkumar Balakrishnan, Wendy Vanherle, Philippe Absil, and Joris Van Campenhout. "50Gb/s C-band GeSi waveguide electro-absorption modulator." In *Optical Fiber Communication Conference*, pp. Tu3D-7. Optical Society of America, 2016.
149. Verbist, Jochem, Michiel Verplaetse, S. A. Srivinasan, Peter De Heyn, Timothy De Keulenaer, Ramses Pierco, Renato Vaernewyck et al. "First real-time 100-Gb/s NRZ-

OOK transmission over 2 km with a silicon photonic electro-absorption modulator." In *Optical Fiber Communication Conference*, pp. Th5C-4. Optical Society of America, 2017.

150. Liu, Jifeng, Dong Pan, Samerkhae Jongthammanurak, Kazumi Wada, Lionel C. Kimerling, and Jurgen Michel. "Design of monolithically integrated GeSi electro-absorption modulators and photodetectors on an SOI platform." *Optics Express* 15, no. 2 (2007): 623-628.
151. Tang, Yongbo, Jonathan D. Peters, and John E. Bowers. "Over 67 GHz bandwidth hybrid silicon electroabsorption modulator with asymmetric segmented electrode for 1.3 μm transmission." *Optics Express* 20, no. 10 (2012): 11529-11535.
152. Liu, Ming, Xiaobo Yin, Erick Ulin-Avila, Baisong Geng, Thomas Zentgraf, Long Ju, Feng Wang, and Xiang Zhang. "A graphene-based broadband optical modulator." *Nature* 474, no. 7349 (2011): 64-67.
153. Xu, Chao, Yichang Jin, Longzhi Yang, Jianyi Yang, and Xiaoqing Jiang. "Characteristics of electro-refractive modulating based on Graphene-Oxide-Silicon waveguide." *Optics express* 20, no. 20 (2012): 22398-22405.
154. Soref RI, Bennett BR. Electrooptical effects in silicon. IEEE journal of quantum electronics. 1987 Jan;23(1):123-9.
155. Cocorullo, G., and I. Rendina. "Thermo-optical modulation at 1.5 mu m in silicon etalon." *Electronics Letters* 28, no. 1 (1992): 83-85.
156. Cocorullo, G., M. Iodice, I. Rendina, and P. M. Sarro. "Silicon thermooptical micromodulator with 700-kHz-3-dB bandwidth." *IEEE photonics technology letters* 7, no. 4 (1995): 363-365.
157. Treyz, G. V., P. G. May, and Jean-Marc Halbout. "Silicon Mach–Zehnder waveguide interferometers based on the plasma dispersion effect." *Applied physics letters* 59, no. 7 (1991): 771-773.
158. Tang, C. K., G. T. Reed, A. J. Walton, and A. G. Rickman. "Low-loss, single-model optical phase modulator in SIMOX material." *Journal of lightwave technology* 12, no. 8 (1994): 1394-1400.
159. Tang, C. K., and G. T. Reed. "Highly efficient optical phase modulator in SOI waveguides." *Electronics letters* 31, no. 6 (1995): 451-452.
160. Xu, Qianfan, Bradley Schmidt, Sameer Pradhan, and Michal Lipson. "Micrometre-scale silicon electro-optic modulator." *nature* 435, no. 7040 (2005): 325-327.
161. Green, William MJ, Michael J. Rooks, Lidija Sekaric, and Yurii A. Vlasov. "Ultra-compact, low RF power, 10 Gb/s silicon Mach-Zehnder modulator." *Optics express* 15, no. 25 (2007): 17106-17113.
162. Xu, Haihua, Zhiyong Li, Yu Zhu, Yuntao Li, Yude Yu, and Jinzhong Yu. "Silicon optical modulator with integrated grating couplers based on 0.18-μm complementary metal oxide semiconductor technology." *Optical Engineering* 50, no. 4 (2011): 044001.

163. Gan, Fuwan, and Franz X. Kartner. "High-speed silicon electrooptic modulator design." *IEEE Photonics Technology Letters* 17, no. 5 (2005): 1007-1009.
164. Liu, Ansheng, Richard Jones, Ling Liao, Dean Samara-Rubio, Doron Rubin, Oded Cohen, Remus Nicolaescu, and Mario Paniccia. "A high-speed silicon optical modulator based on a metal–oxide–semiconductor capacitor." *Nature* 427, no. 6975 (2004): 615-618.
165. Samara-Rubio, Dean, Ling Liao, Ansheng Liu, Richard Jones, Mario Paniccia, Oded Cohen, and Doron Rubin. "A gigahertz silicon-on-insulator Mach-Zehnder modulator." In *Optical Fiber Communication Conference*, p. PD15. Optical Society of America, 2004.
166. Samara-Rubio, Dean, Ulrich D. Keil, Ling Liao, Thorkild Franck, Ansheng Liu, Dexter W. Hodge, Doron Rubin, and Rami Cohen. "Customized drive electronics to extend silicon optical modulators to 4 Gb/s." *Journal of lightwave technology* 23, no. 12 (2005): 4305.
167. Liao, Ling, Dean Samara-Rubio, Michael Morse, Ansheng Liu, Dexter Hodge, Doron Rubin, Ulrich D. Keil, and Thorkild Franck. "High speed silicon Mach-Zehnder modulator." *Optics express* 13, no. 8 (2005): 3129-3135.
168. Gardes, F. Y., G. T. Reed, N. G. Emerson, and C. E. Png. "A sub-micron depletion-type photonic modulator in silicon on insulator." *Optics Express* 13, no. 22 (2005): 8845-8854.
169. Marris-Morini, Delphine, Xavier Le Roux, Laurent Vivien, Eric Cassan, Daniel Pascal, Mathieu Halbwax, Sylvain Maine, Suzanne Laval, Jean Marc Fédéli, and Jean François Damlencourt. "Optical modulation by carrier depletion in a silicon PIN diode." *Optics express* 14, no. 22 (2006): 10838-10843.
170. Liu, Ansheng, Ling Liao, Doron Rubin, Hat Nguyen, Berkehan Ciftcioglu, Yoel Chetrit, Nahum Izhaky, and Mario Paniccia. "High-speed optical modulation based on carrier depletion in a silicon waveguide." *Optics Express* 15, no. 2 (2007): 660-668.
171. Liao, Liu, A. Liu, D. Rubin, J. A. B. J. Basak, Y. A. C. Y. Chetrit, H. A. N. H. Nguyen, R. A. C. R. Cohen, N. A. I. N. Izhaky, and M. A. P. M. Paniccia. "40 Gbit/s silicon optical modulator for high-speed applications." *Electronics letters* 43, no. 22 (2007): 1196-1197.
172. Marris-Morini, Delphine, Laurent Vivien, Jean Marc Fédéli, Eric Cassan, Philippe Lyan, and Suzanne Laval. "Low loss and high speed silicon optical modulator based on a lateral carrier depletion structure." *Optics express* 16, no. 1 (2008): 334-339.
173. Liow, Tsung-Yang, Kah-Wee Ang, Qing Fang, Jun-Feng Song, Yong-Zhong Xiong, Ming-Bin Yu, Guo-Qiang Lo, and Dim-Lee Kwong. "Silicon modulators and germanium photodetectors on SOI: monolithic integration, compatibility, and performance optimization." *IEEE Journal of Selected Topics in Quantum Electronics* 16, no. 1 (2009): 307-315.

174. Gardes, F. Y., D. J. Thomson, N. G. Emerson, and G. T. Reed. "40 Gb/s silicon photonics modulator for TE and TM polarisations." *Optics express* 19, no. 12 (2011): 11804-11814.
175. Thomson, D. J., F. Y. Gardes, Y. Hu, G. Mashanovich, M. Fournier, P. Grosse, J. M. Fedeli, and G. T. Reed. "High contrast 40Gbit/s optical modulation in silicon." *Optics express* 19, no. 12 (2011): 11507-11516.
176. Thomson, David J., Frederic Y. Gardes, Jean-Marc Fedeli, Sanja Zlatanovic, Youfang Hu, Bill Ping Piu Kuo, Evgeny Myslivets et al. "50-Gb/s silicon optical modulator." *IEEE Photonics Technology Letters* 24, no. 4 (2011): 234-236.
177. Rasigade, Gilles, Melissa Ziebell, Delphine Marris-Morini, Jean-Marc Fédéli, Frédéric Milesi, Philippe Grosse, David Bouville, Eric Cassan, and Laurent Vivien. "High extinction ratio 10 Gbit/s silicon optical modulator." *Optics express* 19, no. 7 (2011): 5827-5832.
178. Ziebell, Melissa, Delphine Marris-Morini, Gilles Rasigade, Jean-Marc Fédéli, Paul Crozat, Eric Cassan, David Bouville, and Laurent Vivien. "40 Gbit/s low-loss silicon optical modulator based on a pipin diode." *Optics express* 20, no. 10 (2012): 10591-10596.
179. Malacarne, Antonio, Fabrizio Gambini, Stefano Faralli, Jonathan Klamkin, and Luca Poti. "High-speed silicon electro-optic microring modulator for optical interconnects." *IEEE Photonics Technology Letters* 26, no. 10 (2014): 1042-1044.
180. Xu, Hao, Xianyao Li, Xi Xiao, Peiji Zhou, Zhiyong Li, Jinzhong Yu, and Yude Yu. "High-speed silicon modulator with band equalization." *Optics letters* 39, no. 16 (2014): 4839-4842.
181. Xiao, Xi, Miaofeng Li, Zhiyong Li, Lei Wang, Qi Yang, and Shaohua Yu. "Substrate removed silicon Mach-Zehnder modulator for high baud rate optical intensity modulations." In *Optical Fiber Communication Conference*, pp. Th4H-5. Optical Society of America, 2016.
182. Xiao, Xi, Miaofeng Li, Lei Wang, Daigao Chen, Qi Yang, and Shaohua Yu. "High speed silicon photonic modulators." In *2017 Optical Fiber Communications Conference and Exhibition (OFC)*, pp. 1-3. IEEE, 2017.
183. Zhou, Gangqiang, Linjie Zhou, Yuyao Guo, Shuhuang Chen, Liangjun Lu, Lei Liu, and Jianping Chen. "32-Gb/s OOK and 64-Gb/s PAM-4 Modulation Using a Single-Drive Silicon Mach–Zehnder Modulator with 2 V Drive Voltage." *IEEE Photonics Journal* 11, no. 6 (2019): 1-10.
184. Reed, Graham T., G. Mashanovich, F. Yand Gardes, and D. J. Thomson. "Silicon optical modulators." *Nature photonics* 4, no. 8 (2010): 518.
185. Reed, Graham T., Goran Z. Mashanovich, Frederic Y. Gardes, Milos Nedeljkovic, Youfang Hu, David J. Thomson, Ke Li, Peter R. Wilson, Sheng-Wen Chen, and Shawn S. Hsu. "Recent breakthroughs in carrier depletion based silicon optical modulators." *Nanophotonics* 3, no. 4-5 (2014): 229-245.

186. Xu, Hao, Xi Xiao, Xianyao Li, Yingtao Hu, Zhiyong Li, Tao Chu, Yude Yu, and Jinzhong Yu. "High speed silicon Mach-Zehnder modulator based on interleaved PN junctions." *Optics express* 20, no. 14 (2012): 15093-15099.
187. Brosi, Jan-Michael, Christian Koos, Lucio Claudio Andreani, Michael Waldow, Juerg Leuthold, and Wolfgang Freude. "High-speed low-voltage electro-optic modulator with a polymer-infiltrated silicon photonic crystal waveguide." *Optics Express* 16, no. 6 (2008): 4177-4191.
188. Lee, Mark, Howard E. Katz, Christoph Erben, Douglas M. Gill, Padma Gopalan, Joerg D. Heber, and David J. McGee. "Broadband modulation of light by using an electro-optic polymer." *Science* 298, no. 5597 (2002): 1401-1403.
189. Gardes, F. Y., A. Brimont, P. Sanchis, G. Rasigade, D. Marris-Morini, L. O'Faolain, F. Dong et al. "High-speed modulation of a compact silicon ring resonator based on a reverse-biased pn diode." *Optics express* 17, no. 24 (2009): 21986-21991.
190. Wülbern, Jan Hendrik, Stefan Prorok, Jan Hampe, Alexander Petrov, Manfred Eich, Jingdong Luo, Alex K-Y. Jen, Martin Jenett, and Arne Jacob. "40 GHz electro-optic modulation in hybrid silicon–organic slotted photonic crystal waveguides." *Optics letters* 35, no. 16 (2010): 2753-2755.
191. Lauermann, Matthias, R. Palmer, S. Koeber, P. C. Schindler, D. Korn, T. Wahlbrink, J. Bolten et al. "Low-power silicon-organic hybrid (SOH) modulators for advanced modulation formats." *Optics express* 22, no. 24 (2014): 29927-29936.
192. Densmore, Adam, Siegfried Janz, Rubin Ma, Jens H. Schmid, Dan-Xia Xu, André Delâge, Jean Lapointe, Martin Vachon, and Pavel Cheben. "Compact and low power thermo-optic switch using folded silicon waveguides." *Optics Express* 17, no. 13 (2009): 10457-10465.
193. Abdul-Majid, Sawsan, Ramón Maldonado-Basilio, Chengmin Lei, Hazem Awad, Imad Hasan, N. Ye Winnie, and Trevor J. Hall. "Performance analysis of a photonic integrated interferometer circuit based on silicon-on-insulator." *Optical and Quantum Electronics* 47, no. 7 (2015): 1965-1971.
194. Kodigala, A., M. Gehl, C. T. DeRose, D. Hood, A. T. Pomerene, C. Dallo, D. Trotter et al. "Silicon Photonic Single-Sideband Generation with Dual-Parallel Mach-Zehnder Modulators." In *2019 Conference on Lasers and Electro-Optics (CLEO)*, pp. 1-2. IEEE, 2019.
195. Yamazaki H, Saida T, Goh T, Mino S, Nagatani M, Nosaka H, Murata K. Dual-carrier dual-polarization IQ modulator using a complementary frequency shifter. IEEE Journal of Selected Topics in Quantum Electronics. 2013 May 30; 19(6):175-82.
196. Miller, David AB. "Perfect optics with imperfect components." *Optica* 2, no. 8 (2015): 747-750.
197. Ortega-Moñux, Alejandro, Carlos Alonso-Ramos, Alejandro Maese-Novo, Robert Halir, Luis Zavargo-Peche, Diego Pérez-Galacho, Iñigo Molina-Fernández et al. "An ultra-

compact multimode interference coupler with a subwavelength grating slot." *Laser & Photonics Reviews* 7, no. 2 (2013): L12-L15.

198. Halir, Robert, Przemek J. Bock, Pavel Cheben, Alejandro Ortega-Moñux, Carlos Alonso-Ramos, Jens H. Schmid, Jean Lapointe et al. "Waveguide sub-wavelength structures: a review of principles and applications." *Laser & Photonics Reviews* 9, no. 1 (2015): 25-49.
199. Cheben, Pavel, Jens H. Schmid, Shurui Wang, Dan-Xia Xu, Martin Vachon, Siegfried Janz, Jean Lapointe, Yves Painchaud, and Marie-Josée Picard. "Broadband polarization independent nanophotonic coupler for silicon waveguides with ultra-high efficiency." *Optics express* 23, no. 17 (2015): 22553-22563.
200. Picard, M-J., Y. Painchaud, C. Latrasse, C. Larouche, F. Pelletier, and M. Poulin. "Novel spot-size converter for optical fiber to sub-μm silicon waveguide coupling with low loss, low wavelength dependence and high tolerance to alignment." In *2015 European Conference on Optical Communication (ECOC)*, pp. 1-3. IEEE, 2015.
201. Kahn, Joseph M., and Keang-Po Ho. "Spectral efficiency limits and modulation/detection techniques for DWDM systems." *IEEE Journal of selected topics in quantum electronics* 10, no. 2 (2004): 259-272.
202. Lu, Guo-Wei, Takahide Sakamoto, and Tetsuya Kawanishi. "Flexible high-order QAM transmitter using tandem IQ modulators for generating 16/32/36/64-QAM with balanced complexity in electronics and optics." *Optics express* 21, no. 5 (2013): 6213-6223.
203. Hasan, Gazi Mahamud, Mehedi Hasan, Karin Hinzer, and Trevor Hall. "Vector Modulation Scheme using Three Phase Modulator." In *2019 International Conference on Numerical Simulation of Optoelectronic Devices (NUSOD)*, pp. 127-128. IEEE, 2019.
204. Babakhani, Aydin, Xiang Guan, Abbas Komijani, Arun Natarajan, and Ali Hajimiri. "A 77-GHz phased-array transceiver with on-chip antennas in silicon: Receiver and antennas." *IEEE Journal of Solid-State Circuits* 41, no. 12 (2006): 2795-2806.
205. Koh, Kwang-Jin, and Gabriel M. Rebeiz. "0.13-μm CMOS phase shifters for X-, Ku-, and K-band phased arrays." *IEEE Journal of Solid-State Circuits* 42, no. 11 (2007): 2535-2546.
206. Nikkhah, Hamdam. "Enhancing the Performance of Si Photonics: Structure-Property Relations and Engineered Dispersion Relations." PhD diss., Université d'Ottawa/University of Ottawa, 2018.
207. Wang, Cheng, Mian Zhang, Brian Stern, Michal Lipson, and Marko Lončar. "Nanophotonic lithium niobate electro-optic modulators." *Optics express* 26, no. 2 (2018): 1547-1555.
208. Zhalehpour, Sasan, Jiachuan Lin, Mengqi Guo, Hassan Sepehrian, Zhuhong Zhang, Leslie A. Rusch, and Wei Shi. "All-silicon IQ modulator for 100 GBaud 32QAM transmissions." In *2019 Optical Fiber Communications Conference and Exhibition (OFC)*, pp. 1-3. IEEE, 2019.